



저작자표시-비영리-변경금지 2.0 대한민국

이용자는 아래의 조건을 따르는 경우에 한하여 자유롭게

- 이 저작물을 복제, 배포, 전송, 전시, 공연 및 방송할 수 있습니다.

다음과 같은 조건을 따라야 합니다:



저작자표시. 귀하는 원저작자를 표시하여야 합니다.



비영리. 귀하는 이 저작물을 영리 목적으로 이용할 수 없습니다.



변경금지. 귀하는 이 저작물을 개작, 변형 또는 가공할 수 없습니다.

- 귀하는, 이 저작물의 재이용이나 배포의 경우, 이 저작물에 적용된 이용허락조건을 명확하게 나타내어야 합니다.
- 저작권자로부터 별도의 허가를 받으면 이러한 조건들은 적용되지 않습니다.

저작권법에 따른 이용자의 권리는 위의 내용에 의하여 영향을 받지 않습니다.

이것은 [이용허락규약\(Legal Code\)](#)을 이해하기 쉽게 요약한 것입니다.

[Disclaimer](#)

공학박사 학위논문

**Nanostructured Metal Oxide Electrodes for  
Electrochemical Reduction of Carbon Dioxide**

나노구조 금속 산화물 전극의 전기화학적  
이산화탄소 환원 반응에의 활용

2020 년 8 월

서울대학교 대학원  
공과대학 화학생물공학부  
화학생물공학전공  
정주원

**Nanostructured Metal Oxide Electrodes for  
Electrochemical Reduction of Carbon  
Dioxide**

나노구조 금속 산화물 전극의 전기화학적  
이산화탄소 환원 반응에의 활용

지도 교수 성 영 은

이 논문을 공학박사 학위논문으로 제출함

2020년 8월

서울대학교 대학원

화학생물공학부

정 주 원

정주원의 박사 학위논문을 인준함

2020년 8월

위 원 장

최 장 옥



부위원장

성 영 은



위 원

이 규 태



위 원

박 현 시



위 원

안 상 현



## **Abstract**

# **Nanostructured Metal Oxide Electrodes for Electrochemical Reduction of Carbon Dioxide**

Juwon Jeong

School of Chemical and Biological Engineering

The Graduate School

Seoul National University

With the acceleration of global warming and related environmental issues, the development of environmental-friendly processes utilizing renewable energy is of great urgency. In these situations, the electrochemical reduction of carbon dioxide has a great potential, since it enables both the reduction of total atmospheric carbon dioxide amount by consuming it, and production of economically viable chemicals and feedstock. It is also desirable when the process is combined with intermittent renewable energy sources such as wind and solar energy, by a means of storage vectors of generated energies.

Nonetheless, the practical application of this reaction is almost impossible, because the reaction has many drawbacks in economic viewpoints. The carbon dioxide molecule exhibits a linear structure in which the carbon is bonded to each oxygen atom *via* two strong C=O double bonds. Because of the inert and stable characters of carbon dioxide, the energy required for its activation is quite high, resulting in high overpotential for the whole

reduction processes. Also, non-controlled production is another big problem, regarding the additional cost for separation processes. Therefore, the disentanglement of indicated issues should be done prior to the viable utilization of carbon dioxide electroreduction.

In this regard, numerous types of catalytic materials had been evaluated as possible candidates. Noble metal (i.e. Au, Ag)-based catalysts, p-block metals (i.e. Bi, Sn), and transition metal-based single atom catalysts (M-N<sub>4</sub>; M = Fe, Co, Mn, ...) are main example catalyst groups showed good activities for the reaction. Besides of metallic atom catalysts, the metal oxide catalysts were also studied in quite different objectives. Firstly, the natural reduction of metal oxide into metallic state results in high-indexed facets exhibiting good catalytic activities, thus so-called 'oxide-derived' catalysts showed improved performance. Secondly, along with the computational calculation suggesting oxophilicity as an important factor for easy adsorption of carbon dioxide molecule, the metal oxide catalysts such as SnO<sub>2</sub> successfully produced formate, with their high oxophilicity. In this dissertation, following those strategies, two different oxide-based materials were reported as an efficient system for the carbon dioxide electroreduction.

In first chapter, the brief introduction of carbon dioxide electroreduction was suggested, for the better understanding of following contents. The recent issues on carbon dioxide electroreduction will also be discussed.

In Chapter 2, the results on SnO<sub>2</sub>-based catalyst will be introduced, aimed for the efficient and selective production of formate. The anodization and thermal annealing prepared self-supported SnO<sub>2</sub> nanostructures on Sn foil. The nanostructures showed ~2,000 times enlarged surface area compared to bare Sn foil with highly crystalline SnO<sub>2</sub> phase. Attributed to its large surface and favorable adsorption of carbon dioxide molecules, the prepared electrode exhibited remarkably high partial current of formate, which is

among the state-of-the-art value for formate production catalysts. Analyses on post-electrolysis electrodes unveiled the suppression of reduction and remained Sn oxide phase could be a key for the improved performance of prepared electrode.

In Chapter 3, the ZnO nanorod on the gas-diffusion layer is proposed as an electrode for the efficient reduction of carbon dioxide into carbon monoxide. The ZnO phase reduces into metallic Zn immediately, preparing oxide-derived Zn nanoarchitecture. The *in situ* reduction generates quite different nanoarchitecture compared to bulk Zn, which proves to be more active. Reduced Zn nanorod showed excellent CO<sub>2</sub>-to-CO conversion performance, about 75% on its optimal point. The Tafel analysis evaluated the improved electrokinetics on CO production, altering the energetics on CO<sub>2</sub> adsorption step. Finally, employing the gaseous CO<sub>2</sub>-fed flow type cell, the current density about 80 mA cm<sup>-2</sup> over 75% CO selectivity prolonged for 2-hour electrolysis was obtained on prepared electrode.

**Keywords:** Carbon dioxide, Electrochemistry, Metal oxide electrode, CO<sub>2</sub> reduction, SnO<sub>2</sub>, Nanostructure.

**Student number:** 2014-21521

# Contents

<b>Abstract .....</b>	<b>i</b>
<b>Contents .....</b>	<b>iv</b>
<b>List of Tables .....</b>	<b>vi</b>
<b>List of Figures .....</b>	<b>vii</b>
<b>Chapter 1. Introduction .....</b>	<b>1</b>
1.1. Fundamental of the CO <sub>2</sub> RR .....	3
1.2. Crucial Parameters for CO <sub>2</sub> RR .....	8
1.3. Recent Developments on CO <sub>2</sub> RR .....	11
1.4. System Designs for CO <sub>2</sub> RR .....	17
1.5. References .....	22
<b>Chapter 2. Self-Supported Tin Oxide Nanofilms for CO<sub>2</sub> Electroreduction to Formate .....</b>	<b>27</b>
2.1. Introduction .....	27
2.2. Experimental Section .....	30
2.3. Results and Discussion .....	34
2.4. Conclusion .....	64
2.5. References .....	65

<b>Chapter 3. Oxide-Derived Zn Nanoarchitecture for CO<sub>2</sub></b>	
<b>Electroreduction to CO .....</b>	<b>70</b>
3.1. Introduction .....	70
3.2. Experimental Section .....	73
3.3. Results and Discussion .....	76
3.4. Conclusion .....	101
3.5. References .....	105
<b>국문 초록 (Abstract in Korean) .....</b>	<b>110</b>
<b>List of Publications (SCI) .....</b>	<b>113</b>

# List of Tables

## Chapter 2

**Table 2.1.** Sn 3d peak position and O 1s peak deconvolution results ..... 44

**Table 2.2** Comparison on electrochemical CO<sub>2</sub>RR performances of TA-SnO<sub>2</sub> and previously reported formate-producing Sn-based catalysts ..... 55

## Chapter 3

**Table 3.1** The XPS peak information of Zn foil and ZnO/GDL. The deconvolution results were described as peak position and its relative intensity in parenthesis ... 85

**Table 3.2** The detailed faradaic efficiencies measured on designated potentials and samples ..... 89

# List of Figures

## Chapter 1

<b>Figure 1.1</b> The atmospheric carbon dioxide concentration since 800,000 years before present .....	2
<b>Figure 1.2</b> A scheme for the future application of electrochemical CO <sub>2</sub> conversion .....	4
<b>Figure 1.3</b> Calculated lowest free energy diagrams for the production of a) hydrogen, b) formate, c) CO, and d) methane on Cu surface .....	6
<b>Figure 1.4</b> Detailed CO <sub>2</sub> RR mechanisms .....	9
<b>Figure 1.5</b> OD-Au as an efficient CO-producing catalyst .....	13
<b>Figure 1.6</b> The representative studies on Sn-based catalysts .....	16
<b>Figure 1.7</b> The illustrations for traditional H-cell and flow cell designs .....	18
<b>Figure 1.8</b> Concentration issues lies on H-cell type .....	19

## Chapter 2

<b>Figure 2.1</b> Experimental results of native Sn oxide phase on CO <sub>2</sub> RR .....	29
<b>Figure 2.2</b> The calibration curve for the evaluation of formate concentration .....	33
<b>Figure 2.3</b> The schematic illustration of the synthetic procedures .....	35
<b>Figure 2.4</b> Low-magnification SEM images from (A) AN-SnO <sub>x</sub> , (B) TA-SnO <sub>2</sub> ...	36
<b>Figure 2.5</b> The high-magnification SEM images of (A, B) AN-SnO <sub>x</sub> , and (C, D) TA-SnO <sub>2</sub> .....	37
<b>Figure 2.6</b> Estimation of EDLC values .....	39
<b>Figure 2.7</b> XRD spectra of prepared sample .....	40
<b>Figure 2.8</b> The universal curve of inelastic mean free path of electrons .....	42
<b>Figure 2.9</b> The XPS spectra of prepared samples. (A) Sn 3d region, (B) O 1s region .....	43

<b>Figure 2.10</b> XAFS spectra of Sn foil, AN-SnO <sub>x</sub> , and TA-SnO <sub>2</sub> and corresponding EXAFS spectra obtained at Sn K-edge .....	46
<b>Figure 2.11</b> The <i>j</i> -V polarization curve for the annealed foil electrode measured on Ar- or CO <sub>2</sub> -purged 0.5 M KHCO <sub>3</sub> electrolyte .....	48
<b>Figure 2.12</b> Linear sweep voltammetry curves of Sn foil, AN-SnO <sub>x</sub> , TA-SnO <sub>2</sub> . The scan was done from 0 to -1.0 V .....	50
<b>Figure 2.13</b> The <i>i</i> -t characteristics and corresponding product distribution for each applied potential and sample type .....	51
<b>Figure 2.14</b> The product selectivity distribution of Sn foil, AN-SnO <sub>x</sub> , TA-SnO <sub>2</sub> towards (A) H <sub>2</sub> , (B) CO, (C) Formate. (D) The total CO <sub>2</sub> RR conversion efficiency (FE <sub>CO</sub> + FE <sub>formate</sub> ) for each electrochemical test .....	52
<b>Figure 2.15</b> The formate-generating partial current of each sample .....	54
<b>Figure 2.16</b> Comparison between the specific CO <sub>2</sub> RR activities of AN-SnO <sub>x</sub> and TA-SnO <sub>2</sub> toward formate production by <i>j</i> <sub>HCOO<sup>-</sup></sub> divided by EDLCs .....	57
<b>Figure 2.17</b> Magnified version of the linear sweep voltammogram of bare Sn foil .....	58
<b>Figure 2.18</b> The pourbaix diagram for Sn-O-H system on 298.15 K .....	59
<b>Figure 2.19</b> The digital photograph image displaying commercial SnO and SnO <sub>2</sub> .....	60
<b>Figure 2.20</b> During and post-CO <sub>2</sub> RR analyses on TA-SnO <sub>2</sub> electrode .....	61
<b>Figure 2.21</b> XRD spectra of pristine and post-electrolysis TA-SnO <sub>2</sub> electrodes. The asterisk (*) stands for the SnO <sub>2</sub> signals .....	63

### Chapter 3

<b>Figure 3.1</b> Li electrochemical tuning of ZnO .....	72
<b>Figure 3.2</b> The illustration of MEA-based CO <sub>2</sub> RR flow cell design .....	77
<b>Figure 3.3</b> (A-B) The top-view SEM images, and (C) cross-sectional SEM image of ZnO/GDL .....	79

<b>Figure 3.4</b> (A) Cross-sectional SEM image of ZnO/GDL electrode. (B) F, (C) Zn, (D) O signals from EDX analysis .....	80
<b>Figure 3.5</b> The XRD patterns from ZnO/GDL and Zn foil .....	81
<b>Figure 3.6</b> The XPS spectra for Zn foil and ZnO/GDL using Al K $\alpha$ radiation .....	82
<b>Figure 3.7</b> Wagner plot of Zn .....	84
<b>Figure 3.8</b> The linear-sweep voltammogram profiles of Zn foil and ZnO/GDL, on CO <sub>2</sub> -saturated 0.5 M KHCO <sub>3</sub> electrolyte .....	87
<b>Figure 3.9</b> The i-t characteristics and product distribution results from -0.6 to -1.1 V, for (A-B) Zn foil and (C-D) ZnO/GDL electrodes .....	88
<b>Figure 3.10</b> The product distributions for (A) CO, (B) hydrogen, and (C) formate on Zn foil and ZnO/GDL electrodes from -0.6 to -1.1 V. (D) The normalized FE of CO for the prepared samples .....	91
<b>Figure 3.11</b> The partial current density of CO ( $j_{CO}$ ) of prepared electrodes .....	92
<b>Figure 3.12</b> Comparison of our catalysts with current density profiles from reported Zn-based catalysts .....	93
<b>Figure 3.13</b> The XRD patterns of ZnO/GDL before and after CO <sub>2</sub> RR .....	95
<b>Figure 3.14</b> SEM images taken from (A) pristine ZnO/GDL and (B) after the 1-h electrolysis of CO <sub>2</sub> RR .....	96
<b>Figure 3.15</b> SEM images from (A) pristine Zn foil and (B) Zn foil after the 1-hour electrolysis .....	97
<b>Figure 3.16</b> The electrokinetic studies of CO <sub>2</sub> reduction to CO on oxide-derived Zn from ZnO/GDL electrode and Zn foil .....	99
<b>Figure 3.17</b> Synthetic route and the chemical structure of Sustainion <sup>®</sup> anion exchange membrane .....	102
<b>Figure 3.18</b> The electrocatalytic performance of ZnO/GDL electrode on flow-cell operation .....	103

# Chapter 1. Introduction

Since the beginning of industrial revolution (1760~1840), the technology of human beings has developed unprecedentedly. The rapid growth of machine-based infrastructures around the society has changed every aspect of living. To develop and sustain their developments, people exploited natural resources such as coal, wood, and petroleum extensively to generate energies. [1] The combustion of those resources produced required energies, but it also generated a huge amount of leftover chemical, the carbon dioxide (CO<sub>2</sub>). Because many processes which are vital for human society rely on the consumption of energy which results in the production of CO<sub>2</sub>, soaring amount of anthropogenic CO<sub>2</sub> gases cannot be compensated by natural carbon cycle (e.g. photosynthesis). Human-centered activities produce over 14 gigatons of excess CO<sub>2</sub> annually, and those CO<sub>2</sub> thus accumulated on the Earth's atmosphere. Since 2000, the global atmospheric CO<sub>2</sub> concentration has increased about ~20 ppm decade, which is 10 times higher than the average increase over the previous 800,000 years. [2-3] As a result, the global CO<sub>2</sub> concentration has reached 407.4 ppm on 2018, about 1.33 times higher than the highest concentration of CO<sub>2</sub> on previous history. [4] The widespread CO<sub>2</sub> on the atmosphere has posed severe threats for the humanity, thus it triggered the importance of environmental preservations of the Earth. In order to retard the global warming on our globe, many researches target to alleviate the amount of CO<sub>2</sub> on atmosphere. A large number of carbon capture and storage (CCS) and carbon capture and utilize (CCU) strategies have been proposed in this manner. The captured CO<sub>2</sub> could be utilized in several industrial applications. The injection of CO<sub>2</sub> into reservoirs producing oil and gas enhances hydrocarbon recovery. The catalytic conversion processes using various methods (mineralization, artificial

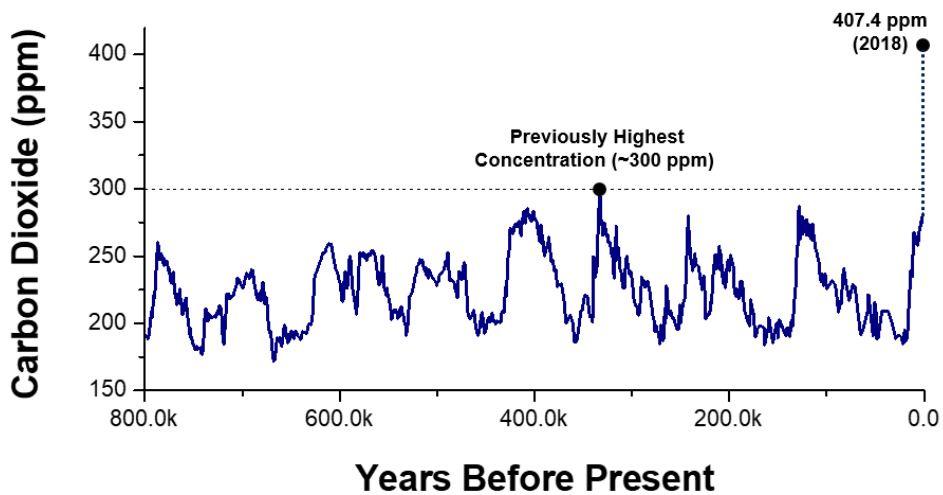


**Figure 1.1** The atmospheric carbon dioxide concentration since 800,000 years before present. On the geologic time scale, the increase (dashed vertical line around present) looks virtually instantaneous. The data were obtained by measuring the trapped airs in Antarctica glacial cores. Data acquired from Ref [4]. (*Nature*, **2008**, 453, 379-382.)

photosynthesis, (electro-)chemical, or biological conversion) also helps the conversion of CO<sub>2</sub> into valuable chemicals and feedstock. [5-6] The electrochemical conversion of carbon dioxide is one of the most promising CCU strategy, as 1) electrochemical reactor could be operated at mild conditions, 2) it require relatively simple and small plant footprints, 3) it can be designed using modular and scalable equipment, and 4) it offers opportunities to produce a wide range of products for chemical feedstock or chemical recycling within an industrial plant. [7-8] In addition, when combined with intermittent renewable energy power sources, CO<sub>2</sub>RR could also serve as the reservoir of those renewable energies, as a form of hydrocarbon feedstock. In this regard, the need of CO<sub>2</sub>RR as an industrial process is in great urgent on both economic and environmental views. Figure 1.2 depicts a blueprint of CO<sub>2</sub>RR. However, just like other potential future technologies, CO<sub>2</sub>RR has many problems that should be solved prior to its viable utilization. The detailed description will be done in next sections.

## **1.1. Fundamental of the CO<sub>2</sub>RR**

Previously, the importance of CO<sub>2</sub>RR, an electrochemical reaction that reduces CO<sub>2</sub> to compounds such as CO, ethylene, and other hydrocarbons, was introduced. We start here describing the fundamental of this reaction. On 1991, pioneering work by Hori reported the CO<sub>2</sub>RR products and efficiencies over a number of pure metallic foils. [9] This work verifies that the CO<sub>2</sub>RR can produce a variety of carbon products, largely depending on what the materials being used for catalysis. For example, when the noble metals such as gold and silver is used, the excellent CO production was observed, while Sn and other p-block metals (e.g. Bi, In) produce formate (HCOO<sup>-</sup>) on relatively high overpotentials. Cu was the only metal producing the mixture of various hydrocarbons and oxygenates such as

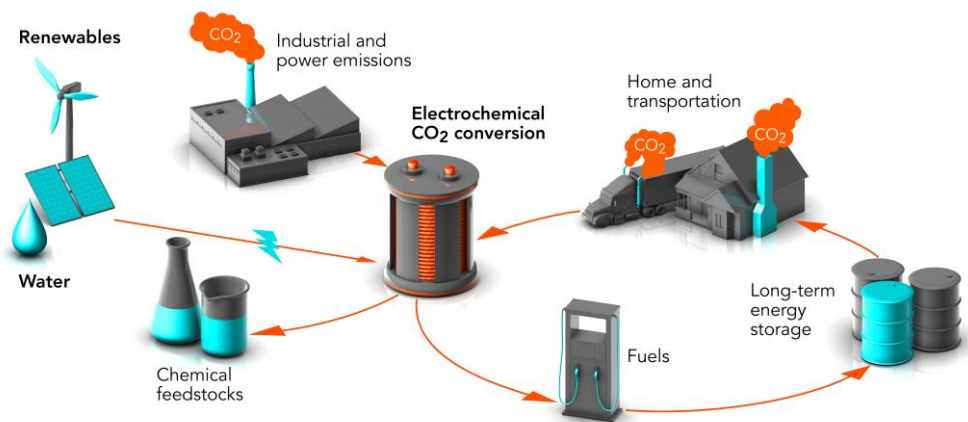


**Figure 1.2** A scheme for the future application of electrochemical CO<sub>2</sub> conversion. On the courtesy of Greg Stewart, from SLAC National Accelerator Laboratory (URL:<https://www6.slac.stanford.edu/news/2019-09-09-plastics-fuels-and-chemical-feedstocks-co2-theyre-working-it.aspx>)

methane, ethylene, and ethanol. A list for reactions and their standard reduction potentials ( $E^0$ ) were listed below. [10] The  $E^0$  values were written versus reversible hydrogen electrode (RHE), at a pH of 7. As seen below, their standard potentials are not much deviated from 0 V vs. RHE, implying the reactions do not take much energy on thermodynamic insights. However, since these reactions compose of many elemental reactions with different reaction energy barriers, the reaction actually takes much energy than expected. (Figure 1.3) That means, the operation on pure metal foil requires high overpotential. Especially, the first step of whole reaction, the adsorption and activation of the  $\text{CO}_2$  molecule is regarded as the most sluggish part. (Equation 8) [11] The  $\text{CO}_2$  molecule itself is very stable, and thus, breaking the stability of that molecule requires large energy.



And also, for the production of highly reduced molecules (that is, requiring more electrons), there exist other elemental reactions that require high energy. Because of those aspects, the real potential required to produce certain product deviates far apart from their standard potential. For example, employing Cu foil as a  $\text{CO}_2\text{RR}$  electrode, the formate mainly be produced near -0.8 V vs. RHE, whilst the

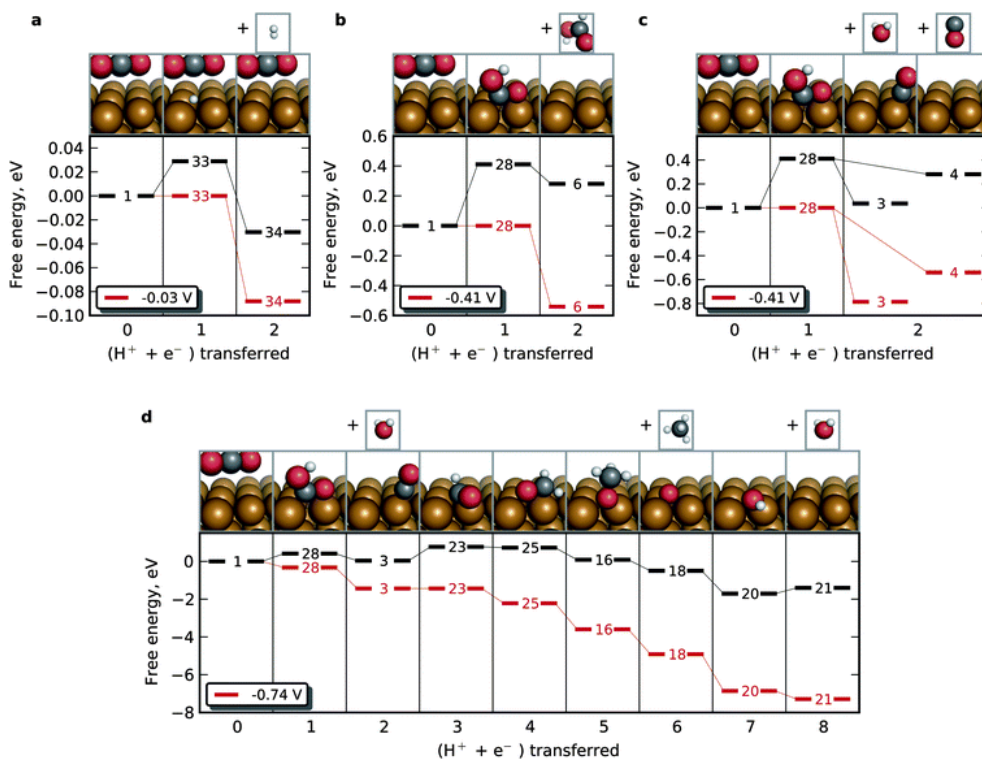


**Figure 1.3** Calculated lowest free energy diagrams for the production of a) hydrogen, b) formate, c) CO, and d) methane on Cu surface. In each diagram, the black (higher) pathway represents the free energy at 0 V vs. RHE, and the red (lower) pathway the free energy on indicated potential. Adapted from Ref [12] (*Energy Environ. Sci.* **2010**, *3*, 1311-1315.).

methane is produced at about -1.0 V vs. RHE. [12] So, the rational choice of the catalytic material with effective tuning is a key for producing the desired product efficiently.

With the aforementioned study of product distribution upon catalyst materials, the mechanism of CO<sub>2</sub> catalysis has also been studied from various research groups. As discussed above, regardless of catalyst materials, activation of bare CO<sub>2</sub> molecule occurs primary. After the activation, the following steps differentiate with their catalytic materials. (Figure 1.4) Au and Ag, known for CO-producing materials, reduces CO<sub>2</sub> into \*COOH, where C is directly adsorbed on catalyst surface. Then, the adsorbed intermediate undergo several following reaction steps, finally exist in the form of \*CO. (C is adsorbed onto the surface.) Since the desorption of \*CO is favorable on the surface and Au and Ag, the adsorbed \*CO detaches from the surface spontaneously, results in the production of CO (g). [13] On the case of formate (HCOO<sup>-</sup>), the reaction is slightly different. The activated CO<sub>2</sub> radical undergo reduction similarly, but results into \*OCHO intermediate, where two O atoms adsorbed onto the surface as a bidentate form. [14] This intermediate then reduces once more, and detaches from the surface, resulting in HCOO<sup>-</sup> (aq) form. The density functional theory (DFT)-based calculation suggested this mechanism, suggesting the oxophilicity of catalyst surface is an important descriptor. Cu has more complicated reaction steps, because it produces much diversified products, and each of the products has a bunch of elemental steps. [15] To begin with, Cu proceeds the reaction similar with CO-producing materials. However, their adsorption energy with \*CO intermediate is relatively high compared to Au and Ag, so the adsorbed molecules do not desorb from the surface. Therefore, if the intermediate gets the enough energy (enough overpotential), it undergoes additional reduction as a form of \*CHO. Additional reduction steps produce C1 products like methane or methanol. In this reaction mechanism, the reduction of \*CHO is known as rate-determining step (RDS). Or, alternatively, two

adjoined \*CO adsorbates can be coupled with each other, resulting in C2 intermediate (\*COCO). This step is known as ‘C-C coupling’ reaction, which is regarded as an RDS for producing C2 molecules such as ethylene, ethanol, or ethane. Since many elemental reactions and electrokinetics are entangled together for the production on Cu surface, thorough studies and analyses should be done for the better catalysis on Cu surface. As C2 products have much better potentials than their C1 counterparts, the development of Cu-based catalytic materials should be done, in order to utilize CO<sub>2</sub>RR in a practical scale.

## **1.2. Crucial Parameters for the CO<sub>2</sub>RR**

In order to understand CO<sub>2</sub>RR and discuss efficiently, some fundamental and useful figure of merits are used to evaluate process performance, including current density, Faradaic efficiency (FE), Tafel slope, and electrochemically active surface area (ECSA).

### **1.2.1. Current density**

Current density of certain electrocatalysts could be obtained by normalizing the obtained current by the surface area or mass of catalyst. The overall current density symbolizes the overall catalyzing ability of the tested catalyst. Therefore, this value is a crucial indicator of the whole performance of the cell.

### **1.2.2. Faradaic efficiency (FE)**

The FE indicates how much the catalysis is focused on a certain product, otherwise denoted as selectivity. This FE value has an enormous meaning for evaluation the electrocatalytic CO<sub>2</sub>RR performance, because the high selectivity is a primary feature for CO<sub>2</sub>RR catalysts. The FE of gaseous products can be

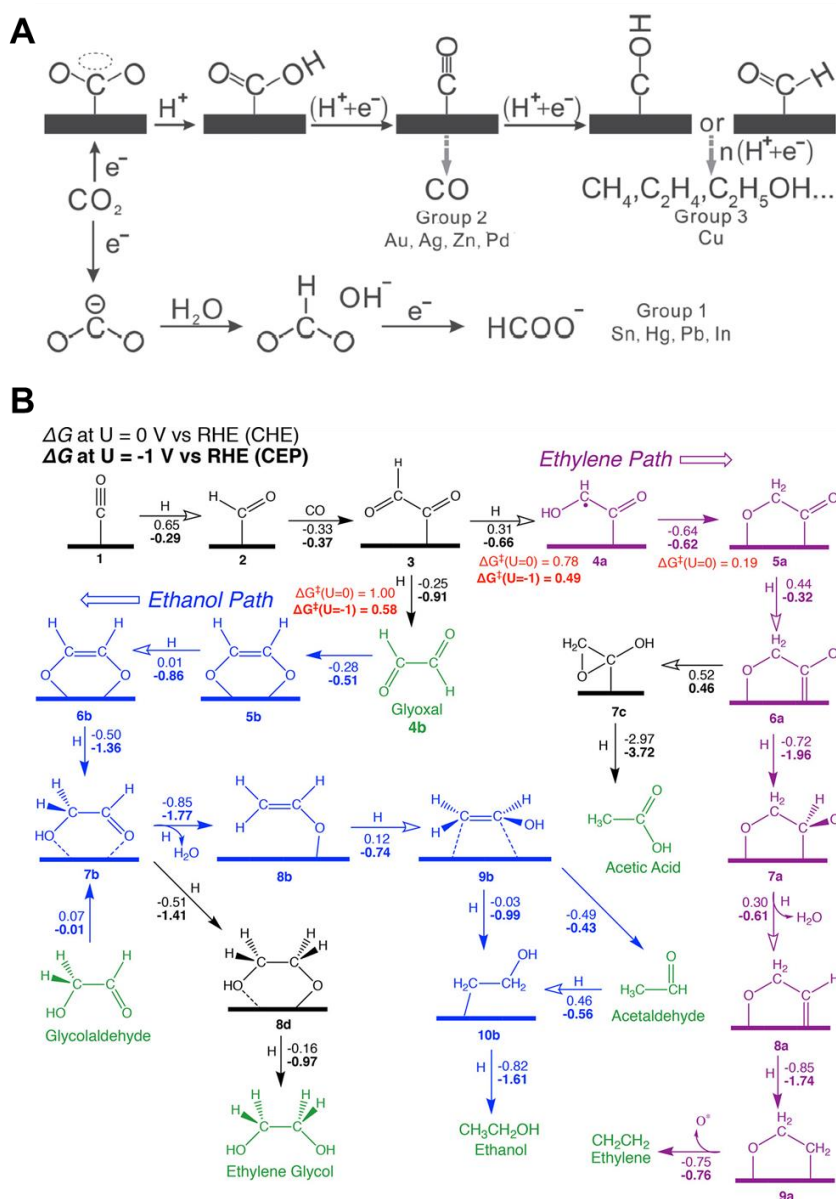


**Figure 1.4** Detailed CO<sub>2</sub>RR mechanisms. A) Reaction mechanism of electrochemical CO<sub>2</sub> reduction on metal electrodes in aqueous solution. B) Proposed mechanism for the reduction of CO to C<sub>2</sub> products on Cu (100). The calculated free energies were written with each arrows on  $U = 0$  and  $-1$  V, respectively. Adapted from Ref [13] (A, *Adv. Mater.* **2016**, 28, 3423-3452.) & [15] (B, *ACS Catal.* **2018**, 8, 1490-1499).

calculated using the Equation (9) as written below,

$$FE_j = \frac{n \times F \times \frac{p_0 Q v_j}{RT}}{i_{total}} \times 100\% \quad (9)$$

where each parameter indicates,

$C_j$  = total charge used to produce the product j [=] C

$m$  = the number of electrons used to produce a molecule j

$n_j$  = the total mole number of product j [=] mol

$V_j$  = the total volume of product j [=] m<sup>3</sup>

$v_j$  = the volume percentage of product j measured from GC signal

$Q$  = total flow rate [=] m<sup>3</sup> s<sup>-1</sup>

The FE for liquid or ionic products are usually obtained using nuclear magnetic resonance (NMR) data.

### 1.2.3. Tafel slope

The Tafel plot, a plot of overpotential versus the logarithm of the partial current density. On lower overpotential region, the electrochemical reaction is purely dictated by the electrokinetics, regardless of mass transfer-related kinetics. The Tafel slope can be measured from Tafel plot on this region, which represents the electrokinetic aspects of the reaction path and its RDS. For example, a Tafel slope of 59 mV dec<sup>-1</sup> suggests the RDS encompassing 0-electron transfer. On CO<sub>2</sub>RR, this could suggest that the reduction undergoes a fast pre-equilibrium involving 1 e<sup>-</sup> transfer to form CO<sub>2</sub> radical and a subsequent slower proton-transfer reaction as the RDS. On the other hand, the slope near 116 mV dec<sup>-1</sup> could be ascribable to an RDS of initial activation step, which is commonly invoked for metal-based catalysts. [16]

#### 1.2.4. Electrochemical surface area (ECSA)

The ECSA means a modified surface area exclusive for electrochemical reaction. It could be differentiated from absolute surface area with the density of specific active sites or other variable related with electrochemical reactions. Typically for the non-metal catalysts, the measurement of electrochemical double-layer capacitance (EDLC;  $C_{dl}$ ) substitutes its direct measurement, since that is hard to apply on non-metal surface. [17] The  $C_{dl}$  is calculated by measuring the capacitive current associated with double-layer charging at different scanning rates of cyclic voltammetry (CV) stripping, using the Equation (10).

$$I = \nu C_{dl} \quad (10)$$

where  $I$  stands for the current measured from CV, and  $\nu$  is scan rate.

### 1.3. Recent Developments on the CO<sub>2</sub>RR

There have been much progresses on CO<sub>2</sub>RR, on the mechanistic, material, and even industrial viewpoints. Herein, the description will be focused on material and their main products.

#### 1.3.1. Producing CO

The CO<sub>2</sub>-to-CO conversion has been extensively studied in early stage of research, because their products were only limited to CO and hydrogen, their overpotential for the production was fairly small (near -0.6 V vs. RHE), and also their relative CO selectivity was already high (>60%). So, in this regard, the researches of noble metals mainly focus to the achievement of almost-unity (that is, near 100%) production of CO by effectively suppressing hydrogen evolution reaction (HER). There are some representative works which combines the theory and the realization of the catalysts well, and thus, showed good performances.

On first, the Kanan group reported oxide derived (OD)-metal catalysts. On the cause of Au, the production of CO above 96% was achieved. (Figure 1.5) [18] They prepared Au<sub>2</sub>O<sub>3</sub> onto the Au foil by electrochemically, by introducing constant potential to Au foil. The prepared Au oxide reduced on the CO<sub>2</sub>RR environment, preparing large grain boundaries covering whole foil surfaces (OD-Au). As-made grain boundaries results in highly-indexed facets and other reactive surfaces for CO<sub>2</sub>RR. As a consequence, the OD-Au produced CO about 96%, with the overpotential of only 140 mV. The long-term stability tests also guaranteed that this catalyst could prolong more than 8 h of electrolysis without much degradation. As a following research, Kanan group also proved that the grain boundaries were main active sites, by correlating the activity with the density of grain boundaries with direct measuring. [19] Along with their great works, many other OD-based materials reported elsewhere, showing good efficiencies for CO<sub>2</sub>RR. [20-22]

Single-atom (M-N-C; M = Fe, Ni, Co, Mn, ...) could also be a nice catalytic material for CO<sub>2</sub>-to-CO reaction. Transition metal-based single atom catalysts were firstly introduced by Strasser group, showing their nice activity for CO production with relatively cheap material prices. [23] In this report, Fe and Ni-based single atom catalysts were showed good efficiencies, because of their HER-suppressing characters. Along with this research, studies such as undercoordinated Ni(I) single atom catalysts, porosity-controlled Fe single atom catalysts successfully reported single-atom catalysts with highly effective production of CO. [24-29]

Though they attract a little attention than noble metals because of their low intrinsic activity toward CO<sub>2</sub>RR, Zn-based materials also researched in some extent, showing good potentials. Because of the relatively cheap material price and non-toxic character for human, Zn-based materials could draw much attention, if they could produce CO as similar as noble metal counterparts. Recently, some successful cases were reported, displaying Zn-based catalysts with the CO

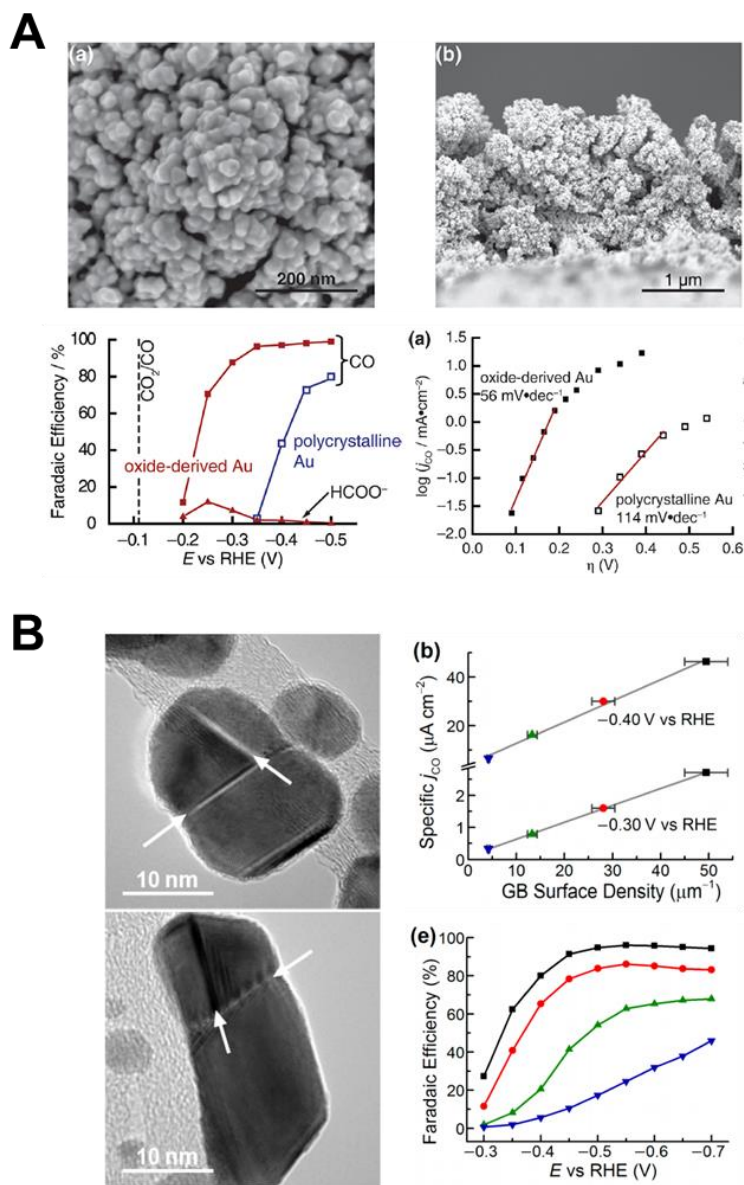


**Figure 1.5** OD-Au as an efficient CO-producing catalyst. A) OD-Au catalysts images and their CO<sub>2</sub>RR performances. B) The prepared grain boundaries by in situ reduction of Au oxide nanoparticles and their performances. Adapted by Ref. [18] (A, *J. Am. Chem. Soc.* **2012**, *134*, 19969-19972) and Ref. [19] (B, *J. Am. Chem. Soc.* **2015**, *137*, 4606-4609).

selectivity above 80%. [30-32] It is very intriguing that pure Zn-based catalysts also showed much improved efficiency with appropriate treatments. Porosity might be the main enhancement factor for it, by improving local pH near electrode by consuming more  $H^+$  ions near electrode surfaces. Alloying with other metals also proved nice strategy for Zn-based materials. [33-35]

### **1.3.2. Producing formate**

As discussed above, p-block metals such as Sn, Bi, In are renowned candidates of producing formate. However, they can selectively produce formate, their operating conditions were too much harsh (maximum about -1.2 V vs. RHE), so their raw materials could not efficiently work as  $CO_2RR$  catalysts compared to CO-producing metals. [9] Although their pure metals do not show good possibility for further applications, the studies targeting formate has continuously reported, because of the higher economic value of formate than CO.

Among the p-block materials, Sn has been drawn most attention, as it exhibited the best  $CO_2RR$  efficiency. On 2012, Kanan group reported that the tin oxide is essential for  $CO_2RR$  electrolysis on Sn, comparing activity and selectivity of acid-etched and bare Sn foils. [36] Sn naturally prepare thin  $SnO_x$  layer on its surface, and etching in acid removes that layer instantly. Strikingly, the acid-etched Sn exhibited much higher current, but the selectivity of formate decreased from 19% to only 0.3%. With combined physicochemical analyses on both samples, the tin oxide phase was surely proved as an active site for  $CO_2RR$  catalysis. From this intriguing results,  $SnO_x$  materials were largely researched from various researchers worldwide, showed decent activities, although their overpotentials were still large. [14] And, as aforementioned above, the relationship with oxophilicity was presented, and related volcano plot also successfully drawn proving the theory. (Figure 1.6)

### 1.3.3. Cu – producing hydrocarbons

Decent application of Cu has been the most precious theme on CO<sub>2</sub>RR, as it is the sole element producing hydrocarbon on its pure phase. In spite of the harsh operating parameters, researchers devoted their idea onto the efficient operation of Cu-based catalysts. With their uncountable efforts onto it, there are numerous reports successfully employing Cu as an efficient, selective production of hydrocarbons currently. [37-40] Sargent group reports the effective CO<sub>2</sub>-to-ethylene conversion using N-aryl-substituted tetrahydro-bipyridine films on a Cu catalyst, exhibiting 72% of ethylene FE at only -0.82 V vs. RHE. The prepared chemical layer improved the stabilization of an 'atop-bound' CO intermediate, thereby favoring further reduction to ethylene. Same group also reports that the electro-redeposited Cu electrodes as an efficient CO<sub>2</sub> reduction electrocatalysts with high C<sub>2</sub>:C<sub>1</sub> selectivity. The redeposited Cu showed nanoscale morphology and interestingly, the stabilization of Cu<sup>+</sup> at negative potentials. With this Cu electrode, the ethylene partial current density of 161 mA cm<sup>-2</sup> was obtained only on -1.0 V vs. RHE. Jaramillo group also reported improved activity employing Cu-based materials. They reported a tandem structure of Au/Cu electrocatalysts, by introducing Au nanoparticles on a polycrystalline Cu foil. A combination of these two materials showed more than 100 times selective production of molecules containing C-C bonds versus C<sub>1</sub> products. They revealed that separated reduction was a key feature for the tandem catalyst. The Au catalyzes CO<sub>2</sub> into CO, and resulting high concentration nearly Cu is ascribable to the high activity upon C<sub>2</sub> product generation. The fluorine-modified copper also exhibited improved C<sub>2</sub>+ generation, by adsorbing \*H and offer it to CO<sub>2</sub>RR when needed. They reported 80% C<sub>2</sub>+ selectivity. A hydrogen-assisted C-C coupling mechanism was hypothesized for the improved performance, verified using X-ray based *in situ* techniques and other analyses.

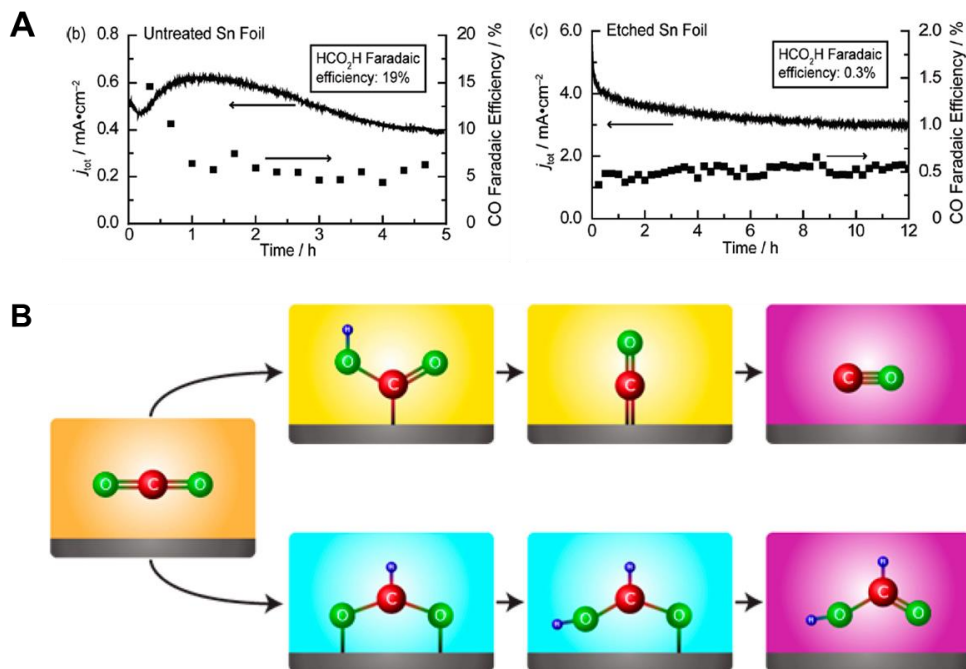


**Figure 1.6** The representative studies on Sn-based catalysts. A) The measured current density and selectivity of formate measured from untreated and etched Sn foils. B) The mechanism that includes pathways for CO and HCOO<sup>-</sup> production from CO<sub>2</sub>. CO<sub>2</sub> may bind to the electrode surface in an initial electrochemical step via the carbon or the oxygens. (which results in \*COOH and \*OCHO, respectively) Adapted and reproduced from Ref. [36] (A, *J. Am. Chem. Soc.* **2012**, *134*, 1986-1989) and Ref. [14] (B, *ACS Catal.* **2017**, *7*, 4822-4827)

However, though numerous strategies were proven effective for the hydrocarbon production on Cu electrode, the principal design mechanism still opaque on Cu electrolysis. There are numerous calculative and realized studies unveiling mechanisms on Cu electrode, but more detailed and fundamental studies are still limited. In this regard, when these uncertainties are disentangled, one could say that there are unprecedented potentials lies on this field.

#### **1.4. System Designs of the CO<sub>2</sub>RR**

The CO<sub>2</sub>RR undoubtedly needs CO<sub>2</sub> molecule as a primary reactant. All aforementioned studies consume CO<sub>2</sub> molecules by solvating them in aqueous electrolyte by CO<sub>2</sub> purging, employing a traditional H-cell as electrocatalysis reactor. H-cell comprises of anodic and cathodic reaction cell parts, and a separator which physically separate two parts to prevent crossover of chemicals between each part. (Figure 1.7) [41] The CO<sub>2</sub>RR occurs on cathodic part, so the CO<sub>2</sub> should be fed continuously and for the measurement of gaseous product. Catalyst that is directly grown or prepared on carbon substrates are usually employed. Neutral (pH ~ 7) solution with dissolved ions (KHCO<sub>3</sub>, KCl, etc.) is commonly used for electrolyte. The pH of electrolyte is of utmost importance, as it determines the selectivity, by controlling the solubility and concentration of each molecule. (Figure 1.8) When the pH goes to acidic, [H<sup>+</sup>] (the concentration of proton) increases, and the HER dominates FE. On the contrary, basic electrolyte results in the decrease of [CO<sub>2</sub>(aq)] concentration, inhibiting the CO<sub>2</sub>RR. [42-43] As a consequence, neutral electrolyte has been used for CO<sub>2</sub>RR.

Given the simplicity of the H-cell based experimental system, the measured performance can usually be directly attributed to the catalyst, albeit within the limitations of H-cell. In H-cell systems, the generated current density is limited (typically under 100 mA cm<sup>-2</sup>), because of the limited access of dissolved CO<sub>2</sub>

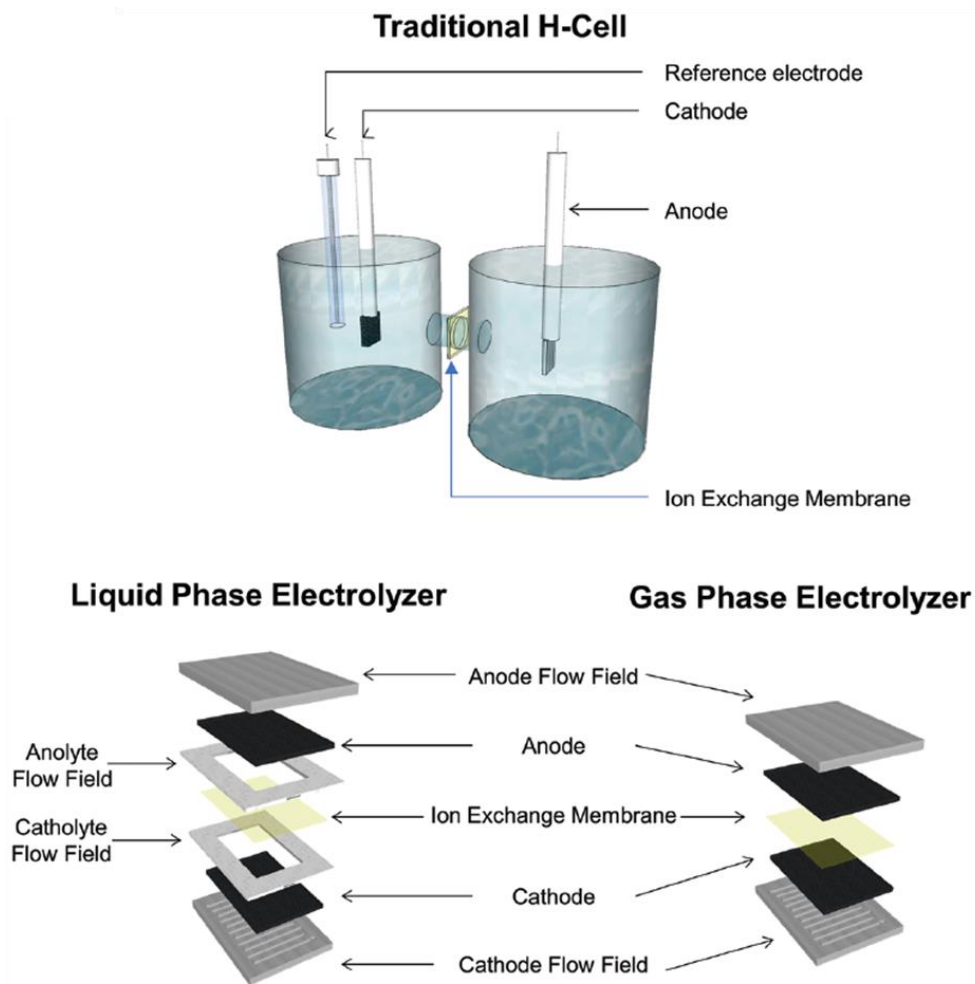


**Figure 1.7** The illustrations for traditional H-cell and flow cell designs. (Top) Scheme for H-cell. H-cell separates anodic and cathodic reactions by ion exchange membrane on their linkage. The CO<sub>2</sub>RR occurs on cathodic compartment. (Bottom) Two representative designs for flow cell architecture. Liquid phase electrolyzer have space for electrolyte, while gas phase electrolyzer only uses ion exchange membrane as solid electrolyte. Adapted from Ref. [41] (Adv. Mater. 2019, 31, 1807166).

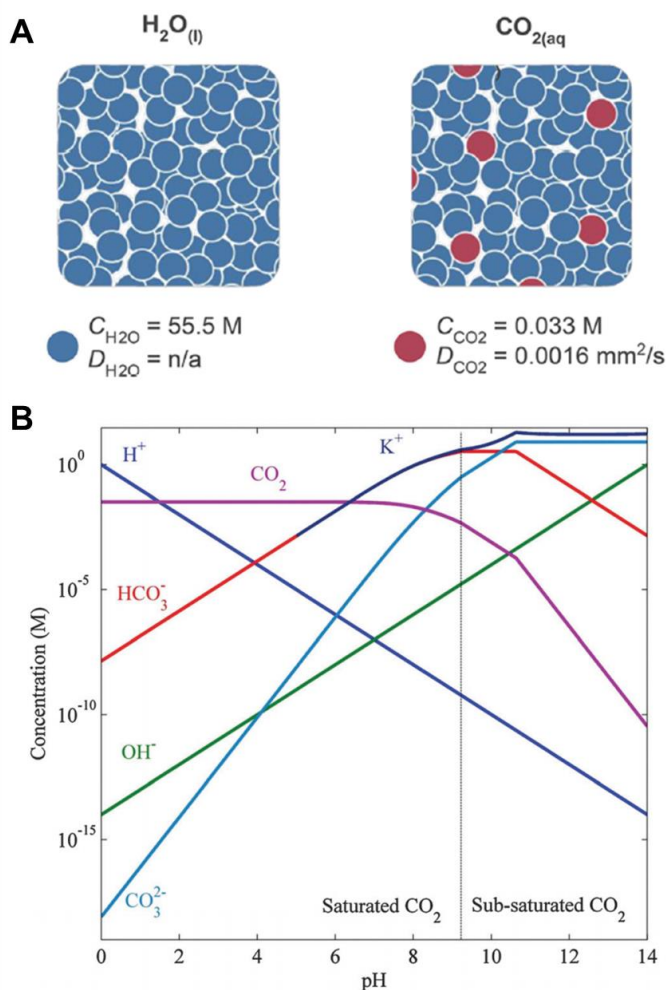


**Figure 1.8** Concentration issues lies on H-cell type. A) The schematics for the distribution of each reactant molecules for HER and  $\text{CO}_2\text{RR}$  in bulk electrolyte. B) The calculated concentration of  $\text{CO}_2$ ,  $\text{H}^+$ , hydroxyl, bicarbonate, carbonate, and potassium ions as a function of pH at 25 °C and a total pressure of 1 atm. Adapted from Ref. [42] (B, *Phys. Chem. Chem. Phys.* **2015**, *17*, 18924-18936.) and Ref. [43] (A, *Acc. Chem. Res.* **2018**, *51*, 910-918.)

within the system. (about 33 mM at room temperature) However, this current density is too small for the application of CO<sub>2</sub>RR industrially. Hence, to tackle the innate problems lies on H-cell design, alternative electrolyzer architectures are being pursued. These so-called ‘flow cell’ designs inspired from water electrolyzers have been studied intensely, to meet the industrial rationales for future applications. (Figure 1.7)

CO<sub>2</sub>RR in flow cell design is much diverged from H-cell architecture, especially in the method of CO<sub>2</sub> feeding. The flow cell design utilizes gaseous CO<sub>2</sub> instead of electrolyte-solved one, resembling the system of alkaline water electrolyzer. Gaseous CO<sub>2</sub> is delivered to cathode site, and liquid electrolyte circulates through the anode compartment of the cell. It is worthy to note that this type of cell could use basic electrolyte such as 1 M KOH, because the cell utilizes gaseous CO<sub>2</sub>, not the solvated one. The gas-phase CO<sub>2</sub> electrolyzer, for example, uses membrane-electrode assembly (MEA) which composed of anode (e.g. Ni foam) and cathode (where CO<sub>2</sub>RR catalysts exists on the gas-diffusion layer (GDL)) and hydroxide exchange membrane (e.g. Sustainion®). On operating conditions, the cathode contacts with membrane and gaseous CO<sub>2</sub> came through GDL. This three-phase boundary composed of solid catalyst, liquid electrolyte (which came from membrane), and gaseous CO<sub>2</sub> is where the catalysis happens. [44] Because of abundant CO<sub>2</sub> concentration near catalytic sites, the CO<sub>2</sub>RR boosts and a current density of hundreds miliampere could be observed. [45]

There are many prototypes of flow cell design, varied for their targeted purposes. MEA-type cell is the simplest type, only applicable for catalysts generating gaseous products only. The liquid phase electrolyzer also uses flow field, where the electrolyte could be existed on cathodic sites. Solid phase electrolyzer also exists, using solid oxide electrolytes where O<sub>2</sub><sup>-</sup> could move through.

Similar with alkaline-based fuel cell, each cell part is under development, including catalytic material, separating membrane, cell type. Sargent group reports

a brilliant result using Nafion<sup>®</sup> ionomer which could extend electrically-feasible active area. By applying this strategy, the CO<sub>2</sub>RR current density of 1.3 A cm<sup>-2</sup> was observed. [46]

It is important to note that mentioned two types of cell have their individual roles which cannot be done in another type of cell. Since the H-cell utilizes the three-electrode configuration, it enables the screening and evaluation of catalysts apart from other variables. Meanwhile, the flow cell configuration focuses much more on the assessment of catalysts practically, which is essential for the industries.

## 1.5. References

[1] *International Energy Outlook 2019*, United States Energy Information Administration, 2018, URL: [eia.gov/outlooks/ieo/](http://eia.gov/outlooks/ieo/)

[2] *Climate Change 2014 Synthesis Report Summary for Policymakers*, Intergovernmental Panel on Climate Change, 2014, URL: [https://www.ipcc.ch/pdf/assessment-report/ar5/syr/AR5\\_SYR\\_FINAL\\_SPM.pdf](https://www.ipcc.ch/pdf/assessment-report/ar5/syr/AR5_SYR_FINAL_SPM.pdf)

[3] *Global Warming of 1.5 °C*, Intergovernmental Panel on Climate Change, 2018, URL: <https://ipcc.ch/sr15/>

[4] Lüthi, D.; Le Floch, M.; Bereiter, B.; Blunier, T.; Barnola, J.-M.; Siegenthaler, U.; Raynaud, D.; Jouzel, J.; Fischer, H.; Kawamura, K.; Stocker, T. F. High-resolution carbon dioxide concentration record 650,000-800,000 years before present. *Nature*, **2008**, *453*, 379-382.

[5] Ramírez-Santos, Á. A.; Castel, C.; Favre, E. A review of gas separation technologies within emission reduction programs in the iron and steel sector: Current application and development perspectives. *Sep. Purif. Technol.* **2018**, *194*, 425-442.

[6] Delacourt, C.; Ridgway, P. L.; Kerr, J. B.; Newman, J. Design of an electrochemical cell making syngas (CO + H<sub>2</sub>) from CO<sub>2</sub> and H<sub>2</sub>O reduction at room temperature. *J. Electrochem. Soc.* **2008**, *155*, B42.

[7] Yang, H. B.; Hung, S.-F.; Liu, S.; Yuan, K.; Miao, S.; Zhang, L.; Huang, X.; Wang, H.-Y.; Cai, W.; Chen, R.; Gao, J.; Yang, X.; Chen, W.; Huang, Y.; Chen, H. M.; Li, C. M.; Zhang, T.; Liu, B. Atomically dispersed Ni(I) as the active site for electrochemical CO<sub>2</sub> reduction. *Nat. Energy* **2018**, *3*, 140-147.

[8] Rosen, B. A.; Salehi-Khojin, A.; Thorson, M. R.; Zhu, W.; Whipple, D. T.; Kenis, P. J. A.; Masel, R. I. Ionic liquid-mediated selective conversion of CO<sub>2</sub> to CO at low overpotential. *Science* **2011**, *334*, 643-644.

[9] Hori, Y. Electrochemical CO<sub>2</sub> reduction on metal electrodes. *Mod. Aspects Electrochem.* **2008**, pp. 89-189.

[10] Nwabara, U. O.; Cofell, E. R.; Verma, S.; Negro, E.; Kenis, P. J. A. Durable cathodes and electrolyzers for the efficient aqueous electrochemical reduction of CO<sub>2</sub>. *ChemSusChem* **2020**, *13*, 855-985.

[11] Rumble, J. R.; Rumble, J. *CRC Handbook of Chemistry and Physics*, 98<sup>th</sup> ed.; CRC Press LLC, **2017**.

[12] Peterson, A. A.; Abild-Pederson, F.; Studt, F.; Rossmeisl, J.; Nørskov, J. K. How copper catalyzes the electroreduction of carbon dioxide into hydrocarbon fuels. *Energy Environ, Sci.* **2010**, *3*, 1311-1315.

[13] Zhu, D. D.; Liu, J. L.; Qiao, S. Z. Recent advances in inorganic heterogeneous electrocatalysts for reduction of carbon dioxide. *Adv. Mater.* **2016**, *28*, 3423-3452.

[14] Feaster, J. T.; Shi, C.; Cave, E. R.; Hatsukade, T.; Abram, D. N.; Kuhl, K. P.; Hahn, C.; Nørskov, J. K.; Jaramillo, T. F. Understanding selectivity for the electrochemical reduction of carbon dioxide to formic acid and carbon monoxide on metal electrodes. *ACS Catal.* **2017**, *7*, 4822-4827.

[15] Garza, A. J.; Bell., A. T.; Head-Gordon, M. Mechanism of CO<sub>2</sub> reduction at copper surfaces: Pathways to C<sub>2</sub> products. *ACS Catal.* **2018**, *8*, 1490-1499.

[16] Agarwal, A. S.; Zhai, Y.; Hill, D.; Sridhar, N. The electrochemical reduction of carbon dioxide to formate/formic acid: Engineering and economic feasibility. *ChemSusChem* **2011**, *4*, 1301-1310.

[17] Lohmann-Richters, F. P.; Abel, B.; Varga, Á. *In situ* determination of the electrochemically active platinum surface area: Key to improvement of solid acid fuel cells. *J. Mater. Chem. A* **2018**, *6*, 2700-2707.

[18] Chen, Y.; Li, C. W.; Kanan, M. W. Aqueous CO<sub>2</sub> reduction at very low overpotential on oxide-derived Au nanoparticles. *J. Am. Chem. Soc.* **2012**, *134*, 19969-19972.

[19] Feng, X.; Jiang, K.; Fan, S.; Kanan, M. W. Grain-boundary-dependent CO<sub>2</sub> electroreduction activity. *J. Am. Chem. Soc.* **2015**, *137*, 4606-4609.

[20] Lum, Y.; Ager, J. W. Evidence for product-specific active sites on oxide-derived Cu catalysts for electrochemical CO<sub>2</sub> reduction. *Nat. Catal.* **2019**, *2*, 86-93.

[21] Yan, C.; Lin, L.; Gao, D.; Wang, G.; Bao, X. Selective CO<sub>2</sub> electroreduction over an oxide-derived gallium catalyst. *J. Mater. Chem. A* **2018**, *6*, 19743-19749.

[22] Pander III, J. E.; Ren, D.; Huang, Y.; Loo, N. W. X.; Hong, S. H. L.; Yeo, B. S. Understanding the heterogeneous electrocatalytic reduction of carbon dioxide on oxide-derived catalysts. *ChemElectroChem* **2018**, *5*, 219-237.

[23] Ju, W.; Bagger, A.; Hao, G.-P.; Varela, A. S.; Sinev, I.; Bon, V.; Cuenya, B. R.; Kaskel, S.; Rossmeisl, J.; Strasser, P. Understanding activity and selectivity of metal-nitrogen-doped carbon catalysts for electrochemical reduction of CO<sub>2</sub>. *Nat. Commun.* **2017**, *8*, 944.

[24] Yang, H.; Lin, Q.; Zhang, C.; Yu, X.; Cheng, Z.; Li, G.; Hu, Q.; Ren, X.; Zhang, Q.; Liu, J.; He, C. Carbon dioxide electroreduction on single-atom nickel decorated carbon membranes with industry compatible current densities. *Nat. Commun.* **2020**, *11*, 593.

[25] Pan, Y.; Lin, R.; Chen, Y.; Liu, S.; Zhu, W.; Cao, X.; Chen, W.; Wu, K.; Cheong, W.-C.; Wang, Y.; Zheng, L.; Luo, J.; Lin, Y.; Liu, Y.; Liu, C.; Li, J.; Lu, Q.; Chen, X.; Wang, D.; Peng, Q.; Chen, C.; Li, Y. Design of single-atom Co-N<sub>5</sub> catalytic site: A robust electrocatalysts for CO<sub>2</sub> reduction with nearly 100% CO selectivity and remarkable stability. *J. Am. Chem. Soc.* **2018**, *140*, 4218-4221.

[26] Yang, H. B.; Hung, S.-F.; Liu, S.; Yuan, K.; Miao, S.; Zhang, L.; Huang, X.; Wang, H.-Y.; Cai, W.; Chen, R.; Gao, J.; Yang, X.; Chen, W.; Huang, Y.; Chen, H. M.; Li, C. M.; Zhang, T.; Liu, B. Atomically dispersed Ni(I) as the active site for electrochemical CO<sub>2</sub> reduction. *Nat. Energy* **2018**, *3*, 140-147.

[27] Gu, J.; Hsu, C.-S.; Bai, L.; Chen, H. M.; Hu, X. Atomically dispersed Fe<sup>3+</sup> sites catalyze efficient CO<sub>2</sub> electroreduction to CO. *Science* **2019**, *364*, 1091-1094.

[28] Hu, C.; Bai, S.; Gao, L.; Liang, S.; Yang, J.; Cheng, S.-D.; Mi, S.-B.; Qiu, J. Porosity-induced high selectivity of CO<sub>2</sub> electroreduction to CO on Fe-doped ZIF-derived carbon catalysts. *ACS Catal.* **2019**, *9*, 11579-11588.

[29] Su, X.; Yang, X.-F.; Huang, Y.; Liu, B.; Zhang, T. Single-atom catalysis toward efficient CO<sub>2</sub> conversion to CO and formate products. *Acc. Chem. Res.* **2019**, *52*, 656-664.

[30] Luo, W.; Zhang, J.; Li, M.; Züttel, A. Boosting CO production in electrocatalytic CO<sub>2</sub> reduction on highly porous Zn catalysts. *ACS Catal.* **2019**, *9*, 3783-3791.

[31] Rosen, J.; Hutchings, G. S.; Lu, Q.; Forest, R. V.; Moore, A.; Jiao, F.

Electrodeposited Zn dendrites with enhanced CO selectivity for electrocatalytic CO<sub>2</sub> reduction. *ACS Catal.* **2015**, *5*, 4586-4591.

[32] Liu, K.; Wang, J.; Shi, M.; Yan, J.; Jiang, Q. Simultaneous achieving of high faradaic efficiency and CO partial current density for CO<sub>2</sub> reduction via robust, noble-metal-free Zn nanosheets with favorable adsorption energy. *Adv. Energy Mater.* **2019**, *6*, 1900276.

[33] Lamaison, S.; Wakerley, D.; Blanchard, J.; Montero, D.; Rouse, G.; Mercier, D.; Marcus, P.; Taverna, D.; Giaume, D.; Mougél, V.; Fontecave, M. High-current-density CO<sub>2</sub>-to-CO electroreduction on Ag-alloyed Zn dendrites at elevated pressure. *Joule* **2020**, *4*, 1-12.

[34] Low, Q. H.; Loo, N. W. X.; Calle-Vallejo, F.; Yeo, B. S. Enhanced electroreduction of carbon dioxide to methanol using zinc dendrites pulse-deposited on silver foam. *Angew. Chem. Int. Ed.* **2019**, *58*, 2256-2260.

[35] Hatsukade, T.; Kuhl, K. P.; Cave, E. R.; Abram, D. N.; Feaster, J. T.; Jongerius, A. L.; Hahn, C.; Jaramillo, T. F. Carbon dioxide electroreduction using a silver-zinc alloy. *Energy Technol.* **2017**, *5*, 955-961.

[36] Chen, Y.; Kanan, M. W. Tin oxide dependence of the CO<sub>2</sub> reduction efficiency on tin electrodes and enhanced activity for tin/tin oxide thin-film catalysts. *J. Am. Chem. Soc.* **2012**, *134*, 1986-1989.

[37] Li, F.; Thevenon, A.; Rosas-Hernández, A.; Wang, Z.; Li, Y.; Gabardo, C. M.; Ozden, A.; Dinh, C. T.; Li, J.; Wang, Y.; Edwards, J. P.; Xu, Y.; McCallum, C.; Tao, L.; Liang, Z.-Q.; Luo, M.; Wang, X.; Li, H.; O'Brien, C. P.; Tan, C.-S.; Nam, D.-H.; Quintero-Bermudez, R.; Zhuang, T.-T.; Li, Y. C.; Han, Z.; Britt, R. D.; Sinton, D.; Agapie, T.; Peters, J. C.; Sargent, E. H. Molecular tuning of CO<sub>2</sub>-to-ethylene conversion. *Nature* **2020**, *577*, 509-513.

[38] Luna, P. D.; Quintero-Bermudez, R.; Dinh, C.-T.; Ross, M. B.; Bushuyev, O. S.; Todorović, P.; Regier, T.; Kelley, S. O.; Yang, P.; Sargent, E. H. Catalyst electroreposition controls morphology and oxidation state for selective carbon dioxide reduction. *Nat. Catal.* **2018**, *1*, 103-110.

[39] Morales-Guio, C. G.; Cave, E. R.; Nitopi, S. A.; Feaster, J. T.; Wang, L.; Kuhl, K. P.; Jackson, A.; Johnson, N. C.; Abran, D. N.; Hatsukade, T.; Hahn, C.; Jaramillo, T. F. Improved CO<sub>2</sub> reduction activity towards C<sub>2+</sub> alcohols on a tandem gold on copper electrocatalyst. *Nat. Catal.* **2018**, *1*, 764-771.

[40] Ma, W.; Xie, S.; Liu, T.; Fan, Q.; Ye, J.; Sun, F.; Jiang, Z.; Zhang, Q.; Cheng, J.; Wang, Y. Electrocatalytic reduction of CO<sub>2</sub> to ethylene and ethanol through hydrogen-assisted C-C coupling over fluorine-modified copper. *Nat. Catal.* **2020**, DOI: 10.1038/s41929-020-0450-0.

[41] Kibria, M. G.; Edwards, J. P.; Gabardo, C. M.; Dinh, C.-D.; Seifitokaldani, A.; Sinton, D.; Sargent, E. H.; Electrochemical CO<sub>2</sub> reduction into chemical feedstocks: From mechanistic electrocatalysis models to system design. *Adv. Mater.* **2019**, *31*, 1807166.

[42] Singh, M. R.; Clark, E. L.; Bell, A. T. Effects of electrolyte, catalyst, and membrane composition and operating conditions on the performance of solar-driven electrochemical reduction of carbon dioxide. *Phys. Chem. Chem. Phys.* **2015**, *17*, 18924-18936.

[43] Weekes, D. M.; Salvatore, D. A.; Reyes, A.; Huang, A.; Berlinguette, C. P. Electrolytic CO<sub>2</sub> reduction in a flow cell. *Acc. Chem. Res.* **2018**, *51*, 910-918.

[44] Liu, K.; Smith, W. A.; Burdyny, T. Introductory guide to assembling and operating gas diffusion electrodes for electrochemical CO<sub>2</sub> reduction. *ACS Energy Lett.* **2019**, *4*, 639-643.

[45] Dinh, C.-T.; Burdyny, T.; Kibria, M. G.; Seifitokaldani, A.; Gabardo, C. M.; Arquer, F. P. G.; Kiani, A.; Edwards, J. P.; Luna, P. D.; Bushuyev, O. S.; Zou, C.; Quintero-Bermudez, R.; Pang, Y.; Sinton, D.; Sargent, E. D. CO<sub>2</sub> electroreduction to ethylene via hydroxide-mediated copper catalysis at an abrupt interface. *Science* **2018**, *360*, 783-787.

[46] Arquer, F. P. G.; Dinh, C.-T.; Ozden, A.; Wicks, J.; McCallum, C.; Kirmani, A. R.; Nam, D.-H.; Gabardo, C.; Seifitokaldani, A.; Wang, X.; Li, Y. C.; Li, F.; Edwards, J. P.; Richter, L. J.; Thorpe, S. J.; Sinton, D.; Sargent, E. D. CO<sub>2</sub> electrolysis to multicarbon products at activities greater than 1 A cm<sup>-2</sup>. *Science* **2020**, *367*, 661-666.

# Chapter 2. Self-Supported Tin Oxide Nanofilms for CO<sub>2</sub> Electroreduction to Formate

## 2.1. Introduction

To achieve the viable applications of CO<sub>2</sub>RR in economic view, many problems are still needed to be solved in precedence. The wide variety of products is one of the problems, which is proven to be partially controlled with rational selection of materials. Among the various products of CO<sub>2</sub>RR, formate (HCOO<sup>-</sup>) is a decent chemical which could be generated from CO<sub>2</sub>RR. The economic feasibility of formate is promising, in that the chemical is regarded as a next-generation liquid fuel, carrying high energy density based on its simple molecule structure. [1-2] Also, recently, a technoeconomic feasibility evaluation was conducted for each CO<sub>2</sub>RR product. [3] The article suggested that CO and formate have economically more viable potentials for practical applications than highly reduced products such as alcohols and hydrocarbons, considering their relatively simple reduction pathways and low overpotentials for producing them. The near-unity production of CO is already achieved on previous reports with noble metals or transition metal single atoms. [4-10] However, contrary to CO catalysts, the current status of formate production still lacks the economical target values required for the practical applications, that is, achieving high selectivity at low overpotentials. [11]

P-block metals such as Sn [12-14], In [15-17], Bi [18-21] mainly produce formate from CO<sub>2</sub>RR. Particularly, Sn-based catalysts are regarded as the best candidate for formate production, from both economical and theoretical aspects. These p-block metals typically have a protective oxide layer on its surface, and thus, the mechanism on these p-block metals are not discovered clearly, especially on verifying active phase on CO<sub>2</sub>RR. On 2012, the experiment on Sn phase was done by Kanan *et al.*, revealing the importance of oxidized Sn phase on the surface of Sn.

[22] The two samples were compared; one is bare Sn and the other is acid-etched Sn. Acid etching removed the thin oxide layer on the surface, preparing surface with metallic Sn phase. The CO<sub>2</sub>RR was conducted for each sample, exhibiting much improved current, but absolutely diminished CO<sub>2</sub>RR selectivity, which verifies the importance of oxide phase upon converting CO<sub>2</sub> into formate. (Figure 2.1) Inspired from the report, a number of studies had reported exploiting Sn oxide materials and the lying mechanism and thermodynamics of Sn-based materials for CO<sub>2</sub>RR. On theoretical studies, particularly, Jaramillo group reported, from the DFT calculation study, that the distribution of formate production current against \*OCHO intermediate exhibits apparent volcano plot, and Sn locates near the maximum point of the volcano. [23] Based on the calculation result, the \*OCHO binding energy strongly relates with the oxophilicity of the catalyst surface, which indirectly suggesting the importance of oxide layer as an active site. Following this paper, the Sn oxide and its derivatives (e.g. SnO, SnS<sub>2</sub>) were intensively studied for CO<sub>2</sub>RR catalysts showing improved formate-producing performances on CO<sub>2</sub>RR electrocatalysis. [24-34] Nonetheless, in spite of their improved performance on formate production, the total current densities of them still show insufficient values (e.g. formate partial current below 20 mA cm<sup>-2</sup>), because of the limited access to the active Sn sites and scarcity of studies on the active phase.

In this regard, herein, employing Sn foil as a starting material, self-supported SnO<sub>2</sub> nanostructures were prepared. The anodic oxidation (anodization) and subsequent annealing in air were sequentially applied to the Sn foil, for the preparation of SnO<sub>2</sub> layer with nanosized architecture. Material characterization revealed that the anodization behaves mainly as structure generator, while the annealing process mainly contributes to the crystallization of prepared nanostructures into SnO<sub>2</sub> phase. The resulting electrode showed superior CO<sub>2</sub>-to-formate converting performance over bare and as-anodized Sn foils, demonstrating increased formate partial current at low overpotential for formate production.

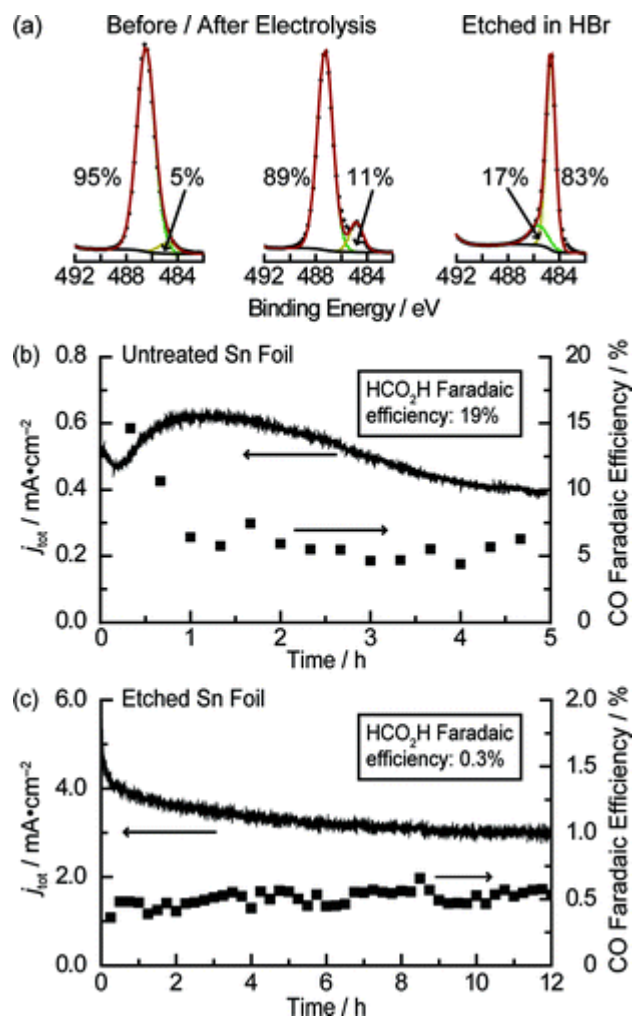


**Figure 2.1** Experimental results of native Sn oxide phase on CO<sub>2</sub>RR. (a) XPS spectra of untreated Sn foil before and after electrolysis and Sn foil after etching in HBr. (b)-(c) Total current density, CO faradaic efficiency (black squares) vs. time on -0.7 V vs. RHE in CO<sub>2</sub>-saturated 0.5 M NaHCO<sub>3</sub>. Adopted from Ref. [22] (*J. Am. Chem. Soc.* **2012**, *134*, 1986-1989)

Ascribable to the top-down synthetic protocol, numerous Sn atoms could be exposed with accessible form on the surface, and thus, a remarkably high current for formate production could be observed. Furthermore, analyses on post-electrolysis electrodes revealed that the prepared SnO<sub>2</sub> electrode resists its full reduction to metallic Sn, maintaining a ‘metastable’ Sn<sup>II</sup>-like oxide phase on its reduction condition. With our results, we concluded that the prepared metastable oxide phase works as a superior phase for formate reduction.

## **2.2. Experimental Section**

### **2.2.1. Preparation and characterization of nanostructured SnO<sub>2</sub> electrodes**

Anodization of Sn foil (Alfa Aesar, 0.25 mm-thick, 99.8%) was carried out in 0.5 M oxalic acid in a two-electrode system (with the assistance of ultrasonication), where a Pt wire was used as counter electrode. The distance between the two electrodes was 5 cm, and 10 V was applied for 10 min. As-anodized electrode was washed with distilled water and was dried in an oven, followed by thermal annealing in air at 500 °C for 3 h. The morphology of SnO<sub>2</sub> electrodes were examined by SEM using Carl Zeiss MERLIN Compact, and XRD patterns were collected by using Rigaku D-MAX2500-PC. XPS analyses were carried out using a synchrotron radiation source at 10A2 beamline of Pohang Accelerator Laboratory (PAL) or by using Thermo Sigma Probe equipped with an Al-K $\alpha$  source. XAFS measurements were performed at 10C beamline of PAL, and the data were processed by using Demeter software package. A potentiostat (Autolab PGSTAT302N) was used for the estimation of EDLCs.

### **2.2.2. Electrochemical Reduction of CO<sub>2</sub>**

For CO<sub>2</sub>RR, all electrochemical measurements were carried out in a three-electrode configuration using a homemade gas-tight H-type cell and Autolab PGSTAT302N, with a Ag/AgCl reference electrode (filled with saturated KCl

solution) and a graphite rod counter electrode. The glass cell was comprised of anodic and cathodic compartments which were separated by cation exchange membrane (Nafion® 117) to prevent any contamination by crossovers between cathode and anode. Ohmic resistance of solution was measured using electrochemical impedance spectroscopy (EIS) before the reaction and was used for  $iR$  correction for all of the measurements.  $\text{CO}_2$ -saturated 0.5 M  $\text{KHCO}_3$  was used as electrolyte;  $\text{CO}_2$  gas was delivered with specific rate (20 sccm) from at least 30 minutes before the reaction and was continuously purged throughout the measurements. In the case of steady-state  $\text{CO}_2\text{RR}$ , cathodic electrolyte was continuously stirred at 400 rpm. All potentials were converted to RHE scale by using the following equation:

$$E_{\text{RHE}} = E_{\text{Ag/AgCl}} + 0.197 \text{ V} + 0.0592 \text{ pH} \quad (1)$$

### 2.2.3. Analyses of products from $\text{CO}_2\text{RR}$

Gaseous products were analyzed by using a GC (Agilent 7890B) equipped with a flame ionization detector (FID) and a thermal conductivity detector (TCD) for detection of  $\text{CO}$  and  $\text{H}_2$ , respectively. FE of each gaseous product was calculated from the obtained volume concentration using the following equation:

$$\text{FE}_j = \frac{i_j}{i_{\text{total}}} \times 100\% = \frac{2 \times F \times \frac{p_0 Q v_j}{RT}}{i_{\text{total}}} \times 100\% \quad (j = \text{H}_2 \text{ or } \text{CO}) \quad (2)$$

(where  $v_j$  = volume concentration measured from GC,  $Q$  = flow rate of delivering  $\text{CO}_2$ ,  $F = 96485 \text{ C mol}^{-1}$ ,  $p_0 = 101325 \text{ Pa}$ ,  $R = 8.314 \text{ J mol}^{-1} \text{ K}^{-1}$ ,  $T = 298.15 \text{ K}$ , and  $i_{\text{total}}$  = overall current measured at the moment of injection). Quantification of formate was performed by measuring 600 MHz NMR peak area using Bruker AVANCE 600. The sample for  $^1\text{H}$  NMR was prepared by mixing 450  $\mu\text{L}$  aliquot of

electrolyte with 50  $\mu\text{L}$  of 1% 3-(trimethylsilyl)-1-propanesulfonic acid (DSS) in  $\text{D}_2\text{O}$  (Sigma-Aldrich). The formate peak area on  $^1\text{H}$  NMR ( $\delta = 8.445$ ) was converted to the amount of formate based on the calibration curve in Figure 2.2. Then, formate selectivity was calculated by dividing this amount by the total charge consumed during the  $\text{CO}_2\text{RR}$ . All of the experiments related to product quantification were conducted at least three times to verify the reliability of our results by presenting the statistics.

#### 2.2.4. EDLC evaluation

Electrochemical double layer capacitance (EDLC) was estimated by measuring double layer capacitance of Sn foil electrodes. [12, 24] In Ar-saturated 0.5 M  $\text{KHCO}_3$  electrolyte, the cyclic voltammetry (CV) was conducted for prepared Sn electrodes. The CV was conducted in non-faradaic region ( $0.17 \sim 0.37 \text{ V}_{\text{RHE}}$ ) controlling scan rates from 20 to 100  $\text{mV s}^{-1}$ . The cathodic and anodic current differences at  $0.3 \text{ V}_{\text{RHE}}$  were then plotted against scan rate to measure their double layer capacitances. The estimated EDLC values were calculated using the equation (3) stated as:

$$(\Delta j / 2) = \text{EDLC} * \nu \quad (3)$$

( $\Delta j$  = current density difference at  $0.3 \text{ V}_{\text{RHE}}$ ,  $\nu$  = scan rate)

Please note that the obtained value does not stand the exact value, but means as a convenient figure for comparing among samples.

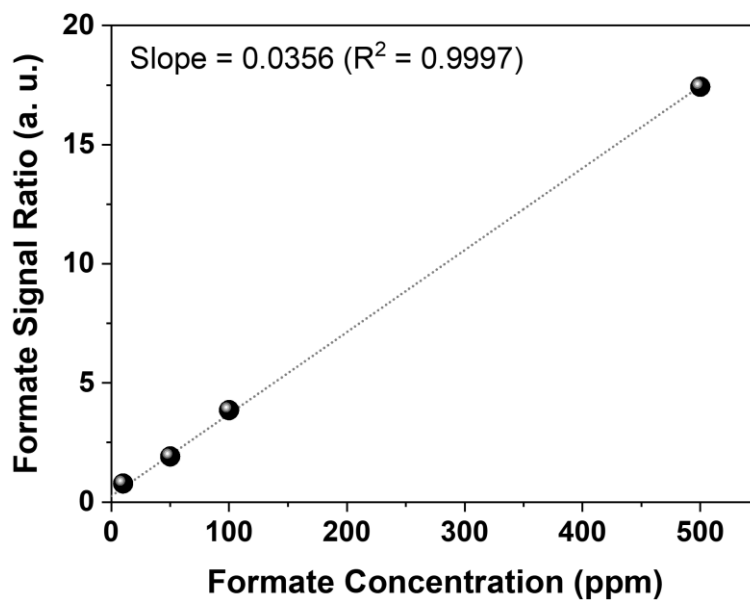


**Figure 2.2** The calibration curve for the evaluation of formate concentration. The peak area of formate ( $\delta = 8.445$ ) was first modified with respect to reference DSS peak ( $\delta = 0$ ), and the obtained value was calibrated again using the curve above.

## 2.3. Results and discussion

### 2.3.1. Synthesis and characterizations of tin oxide nanofilms.

Nanostructured Sn oxide was prepared on the Sn foil by applying two distinctive oxidative approaches to the bare Sn foil. The Sn foil was cleaned in ethanol and distilled water (DI) prior to the oxidative processes. The anodic oxidation (anodization) was applied using 0.5 M of oxalic acid aqueous solution as an etching electrolyte to the fresh foil. [35] An application of a DC potential of 10 V made self-supported Sn oxide nanostructures on the Sn foil. The resulting samples were kept under N<sub>2</sub> stream in oven for further procedures and denoted as ‘AN-SnO<sub>x</sub>’. (Anodized SnO<sub>x</sub>) The AN-SnO<sub>x</sub> was then annealed in air at 500 °C to stabilize the prepared layer with more crystallized phase. Post-annealed sample also kept in oven with N<sub>2</sub> stream, and the sample is denoted as ‘TA-SnO<sub>2</sub>’. (Thermally-annealed SnO<sub>2</sub>) Those samples were then directly used for electrochemical evaluations without further modification processes. The whole processes of the nanofilm preparations were summarized in Figure 2.3. Please note that the direct annealing of bare Sn foil without anodization results in fragile structures which could not be employed as an electrode, therefore excluded from further electrochemical examinations.

The surface morphology of the synthesized SnO<sub>2</sub> nanostructures was observed using field-emission scanning electron microscopy (FE-SEM), as depicted in Figure 2.4 for low-magnification and Figure 2.5 for high-magnification images. The AN-SnO<sub>x</sub> samples showed uniform nanochannel structures covering the whole surface of as-anodized foil. The synthesized structure was composed of almost uniformly sized pores about 50 nm, as shown in SEM images. After the annealing processes from Figure 2.4 and 2.5, it is obvious that the annealing processes changed the prepared nanofilm with more disordered version. The existed flat surface was roughened, and the disordered pore structure was observed with

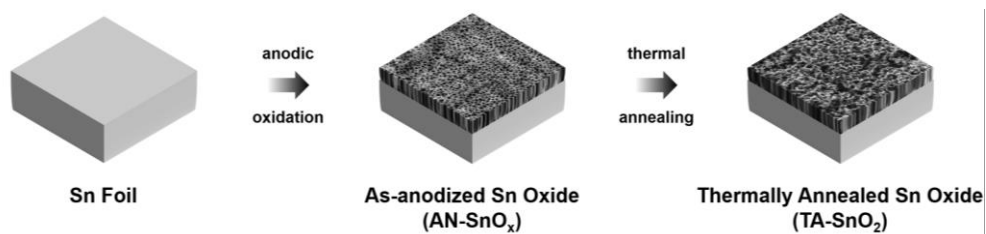


**Figure 2.3** The schematic illustration of the synthetic procedures. Electrochemical anodization of Sn foil followed by thermal annealing. The SEM images were exploited as top-side surfaces of prepared images.

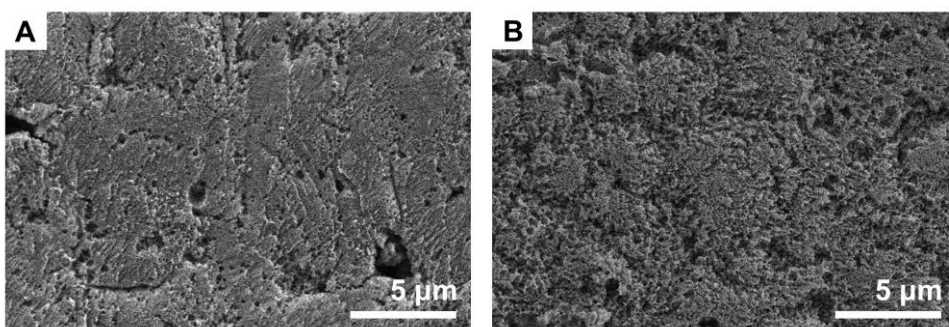


**Figure 2.4** Low-magnification SEM images from (A) AN-SnO<sub>x</sub>, (B) TA-SnO<sub>2</sub>.

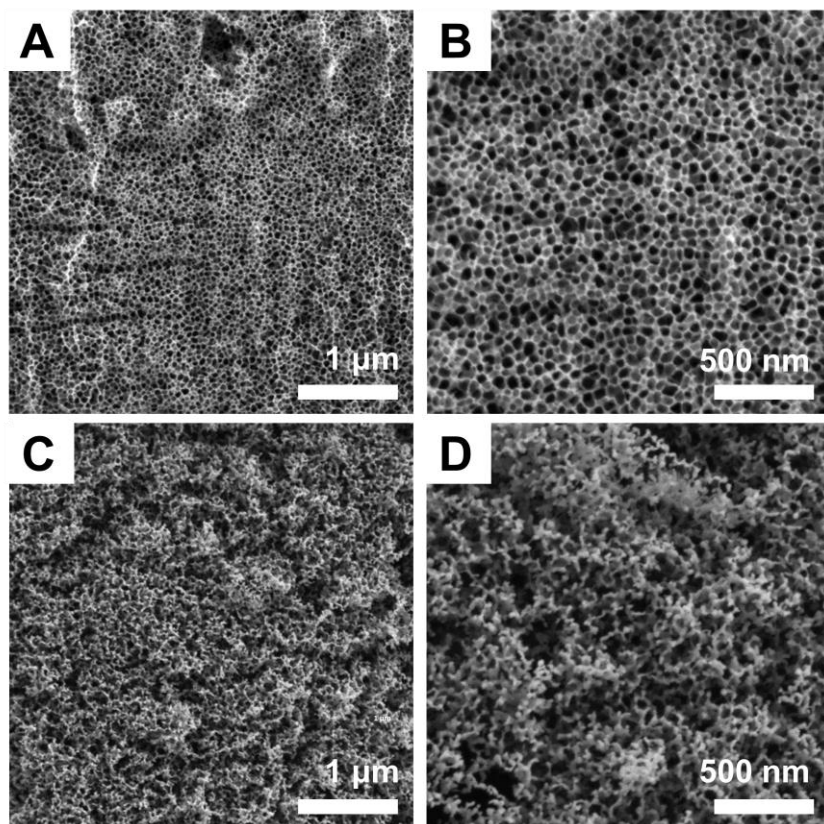


**Figure 2.5** The high-magnification SEM images of (A, B) AN-SnO<sub>x</sub>, and (C, D) TA-SnO<sub>2</sub>. The destruction of nanoporous morphology is clearly seen by comparing AN-SnO<sub>x</sub> and TA-SnO<sub>2</sub> images.

diversified pore sizes. Nevertheless, the most importantly, the decent level of overall nanostructures was retained during the annealing processes, though the structure is much deviated from ordered pore structures. In order to compare the degree of disorder of prepared nanostructure between AN-SnO<sub>x</sub> and TA-SnO<sub>2</sub>, electrochemical double layer capacitances (EDLCs) were estimated for prepared samples. To avoid the structural damage from recurring oxidation and reduction of Sn oxide structure, the potential range of scanning sets to avoid near 0 V (where the Sn<sup>0/IV</sup> redox potential exists, refer Figure 2.11), which is between 0.17 and 0.37 V. These CV and according EDLC evaluation were summarized in Figure 2.6. The EDLCs were evaluated using the above-mentioned equation (3). The  $\Delta j$  ( $j_a - j_c$ ) obtained from CV using current densities at 0.3 V were used for evaluation, stated on Figure 2.6 D-F. The obtained values were 2.01  $\mu\text{F cm}^{-2}$ , 23.21  $\text{mF cm}^{-2}$ , and 4.36  $\text{mF cm}^{-2}$  for bare Sn foil, AN-SnO<sub>x</sub> and TA-SnO<sub>2</sub>, respectively. After the anodization, the surface area accessible for electrochemical reaction increased dramatically even over three orders of magnitude. Meanwhile, the annealing process decreased the total surface area, about 1/5 to that of AN-SnO<sub>x</sub>. This unveils that thermal annealing process was detrimental to the sustaining the nanostructure. But, when comparing TA-SnO<sub>2</sub> and bare foil, the TA-SnO<sub>2</sub> still has about 2,000 times larger surface area than that on bare foil. This implies that the TA-SnO<sub>2</sub> have substantially larger active sites that can be accessible on electrochemical analyses.

For the identification of crystal structures and phase developments upon each experimental process, we first carried out X-ray diffraction (XRD) analysis. (Figure 2.7) A pure metallic feature appears on bare Sn foil, (JCPDS #65-0296) suggesting a thin and amorphous feature of the native oxide film. It is really interesting that the anodization did not alter the XRD spectrum of AN-SnO<sub>x</sub>, indicating the highly amorphous character of prepared oxide nanofilm. The metallic Sn signals might come from the metallic Sn underneath the nanostructured

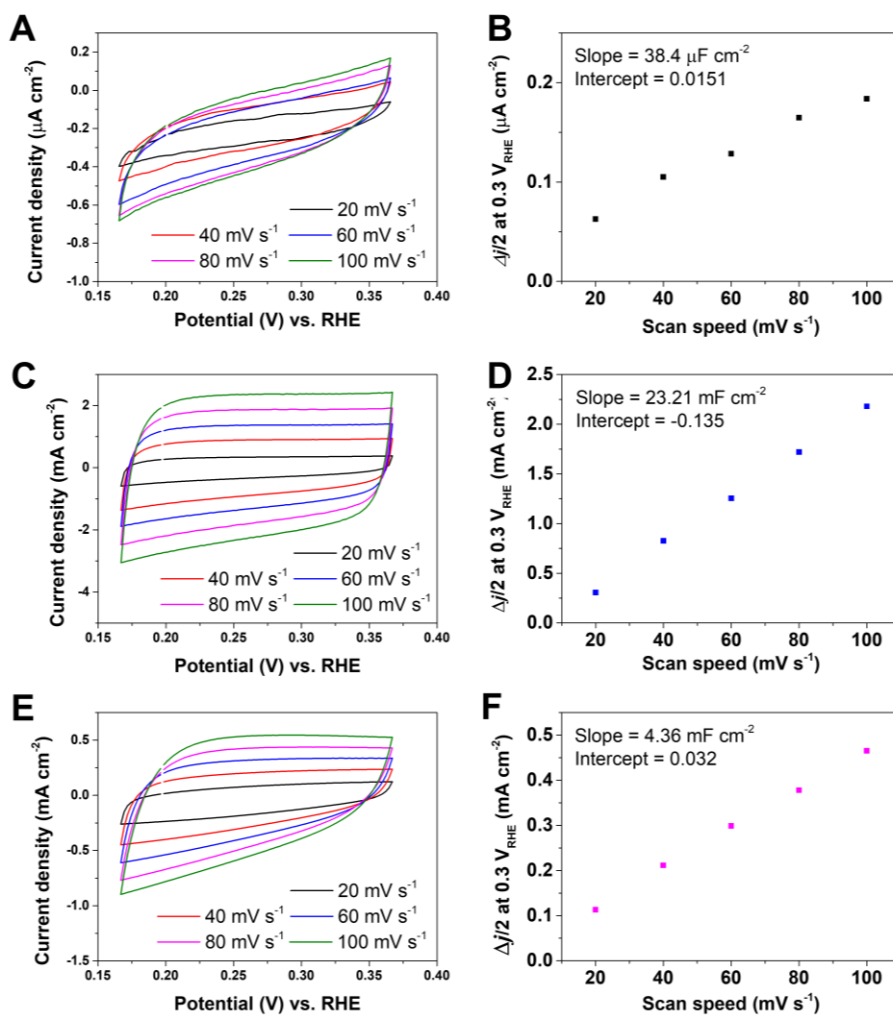


**Figure 2.6** Estimation of EDLC values. (A) CV spectrum displaying non-faradaic capacitive current for bare Sn foil. (B) Corresponding  $\Delta j$  against scan speed for the estimation of EDLC values from slope. The information of linear regression was stated top-left side of graph. (C-D) Same data for AN-SnO<sub>x</sub>, (E-F) TA-SnO<sub>2</sub>.

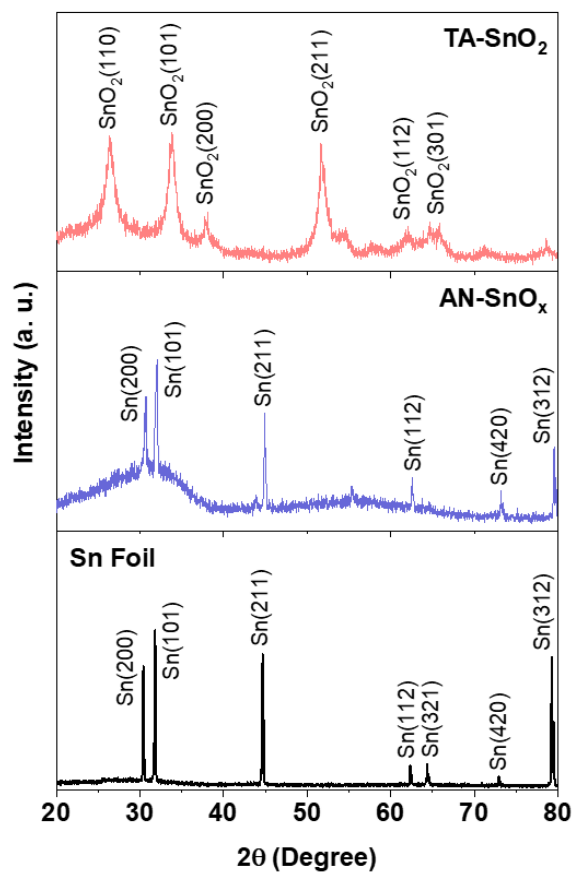


**Figure 2.7** XRD spectra of prepared sample. The XRD spectra for TA-SnO<sub>2</sub>, AN-SnO<sub>x</sub>, bare Sn foil from top to bottom. Each signal was assigned using powder diffraction pattern database. (Sn signals were referred from JCPDS #65-0296, and SnO<sub>2</sub> from JCPDS #41-1445.)

layer. The signals of Sn (220) and Sn (310) planes were newly appeared on AN-SnO<sub>x</sub> spectra, which didn't exist on bare Sn foil. Maybe the restructuring of Sn atoms was happened, caused by electrochemical anodization. Only broad signal which appears on SnO<sub>2</sub> peak position suggesting the existence of oxide on AN-SnO<sub>x</sub> sample. With annealing in air, the XRD spectrum fully changed to SnO<sub>2</sub>-related signals. (JCPDS #41-1445) Sharp signals indicate the highly-crystalline SnO<sub>2</sub> was prepared from annealing, with hardly detectable Sn-based signals. This can be attributed to the lower melting point of Sn metal (232 °C) compared to annealing temperature, which melts and reacts with oxygen in the air during the annealing. [36]

For the more detailed analysis on their chemical information, X-ray photoelectron spectroscopy (XPS) and X-ray absorption fine structure spectroscopy (XAFS) were conducted for prepared samples. The beam energy of 590 eV was chosen, to minimize the inelastic mean free path of electrons through the sample. The work of *Seah* and *Dench* describes that the inelastic mean free path of electron is determined with the escaping electron energy. [37] It reports that the inelastic mean free path can be described universally on categorized material types (e.g. metal, organic chemicals). For inorganic materials, the minimal penetration depth locates on the electron energy values between 30 to 100 eV, corresponding with 590 eV beam escaping SnO<sub>2</sub> layers (Sn 3d = 480-500 eV / O 1s = 520-540 eV), meaning that XPS results from 590 eV beam convey the information about atoms located on the utmost surface. (Figure 2.8) Figure 2.9 shows XPS Sn 3d and O 1s spectra of prepared samples, with detailed fitting results of O 1s spectra described in Table 2.1. The Sn 3d spectra on Figure 2.9A clearly shows how the surface state of Sn 3d develops upon each oxidation process. At first, the Sn 3d<sub>5/2</sub> peak position of 486.32 eV on bare Sn clearly indicates the majority phase of bare Sn foil surface is metallic Sn states (Sn<sup>0</sup> = 484-486 eV). [14] On AN-SnO<sub>x</sub>, the Sn 3d<sub>5/2</sub> peak

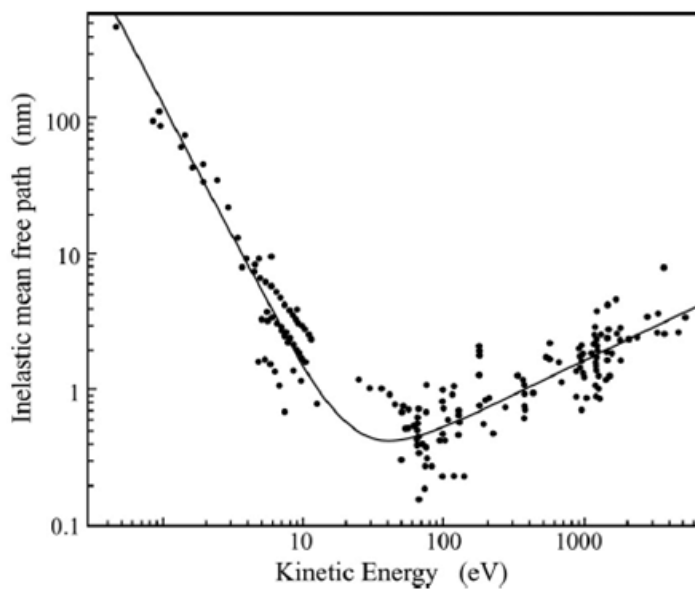


**Figure 2.8** The universal curve of inelastic mean free path of electrons. The path lengths are very high at low energies, fall to 0.1-0.8 nm for energies in the range of 30-100 eV and then rise again as the energy increases further. With theoretical derivation, the universal curve could be expressed as  $\lambda_m = 538 E^{-2} + 0.14 (\alpha E)^{1/2}$  for inorganic compounds. ( $\lambda_m$  = path length, E = electron energy,  $\alpha$  = monolayer thickness in nm.) Adapted from Ref. [37] (*Surf. Interface Anal.* **1979**, 1, 2-11.)

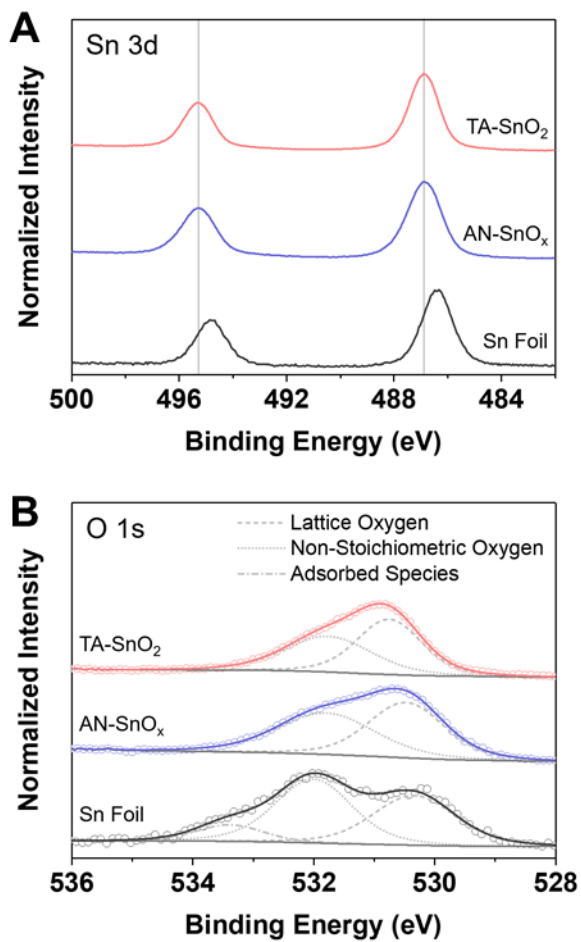


**Figure 2.9** The XPS spectra of prepared samples. (A) Sn 3d region, (B) O 1s region.

**Table 2.1.** Sn 3d peak position and O 1s peak deconvolution results.

	Bare Sn	As-anodized	Annealed
Sn 3d <sub>5/2</sub> position	487.03 eV	487.06 eV	486.82 eV
Sn-O-Sn	530.19 eV (30.9%)	530.47 eV (50.8%)	530.75 eV (53.4%)
Sn-O	531.96 eV (63.3%)	531.79 eV (49.2%)	531.76 eV (46.4%)
O-C <sub>contam.</sub>	533.57 eV (5.8%)	-	-

position was shifted from 486.32 eV to 486.90 eV, suggesting phase shift from Sn<sup>0</sup> to Sn<sup>IV</sup>. (Sn<sup>IV</sup> = 486.5-487.5 eV) [14] Annealing in air did not alter the position of Sn 3d<sub>5/2</sub> peak (486.90 eV to 486.91 eV), as the surface was fully oxidized to Sn<sup>IV</sup> on anodization process. Besides, the XPS spectra from O 1s region also show a clear trend, which develops toward the more crystallized version of Sn oxide. It is well-known that the O 1s from tin oxide could briefly be categorized into three peaks; from lattice oxygen which represents highly crystalline structure (Sn-O-Sn, near 530.5 eV), from non-stoichiometric oxides on the surface (Sn-O, near 532.0 eV), and the adsorbed surface oxygen from adventitious sources. (C-O, near 533.5 eV) [38-39] From the deconvolution results, (Table 2.1) we found that the Sn-O-Sn peak was increased after anodization (from 30.9% to 50.8%), and slightly increased by annealing (53.4%). Meanwhile, the Sn-O peak ratio continuously decreases from 63.3% to 49.2% & 46.4%, respectively. The increase of lattice oxygen amount with concomitant decrease of Sn-O implies that the more crystallized SnO<sub>2</sub> surfaces along with the procedures. As a consequence, we could conclude that the surface of Sn foil was transformed into crystallized oxide on the anodization step, and annealing further crystallizes of less crystallized oxide. This observation is in line with those from XRD and XPS Sn 3d measurements; anodization results in the oxidation, further crystallized by the thermal annealing. In order to understand the nature of chemical bonding between Sn and O in the Sn oxide films, we performed X-ray absorption fine structure spectroscopy (XAFS) analyses at Sn K-edge, and the data are displayed in Figure 2.10. Given that XAFS is not a surface-sensitive method but rather a tool for analysis of bulk characteristics of materials, signals from metallic Sn in the substrate was dominant in all of the spectra; however, we could still see the differences from extended X-ray absorption fine structure spectroscopy (EXAFS) results displayed in Figure 2.10B; especially within 1 to 2 Å wherein the responses from Sn-O species are known to appear. [12, 40] Sn-O

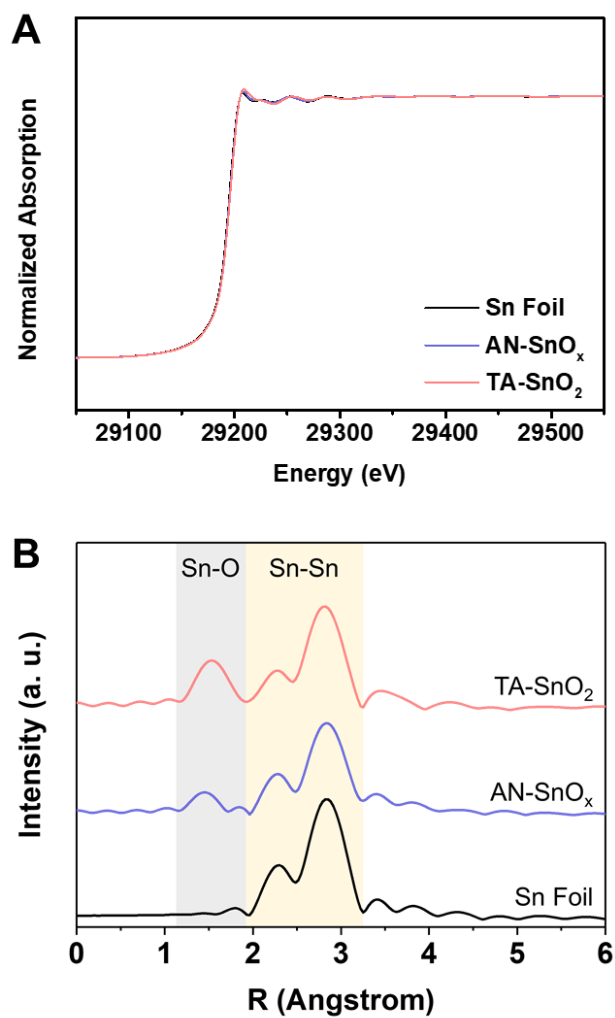


**Figure 2.10** XAFS spectra of Sn foil, AN-SnO<sub>x</sub>, and TA-SnO<sub>2</sub> and corresponding EXAFS spectra obtained at Sn K-edge.  $k^3$ -weighted Fourier transform was used for the EXAFS spectra.

signal which was negligible in the case of Sn foil became apparent in AN-SnO<sub>x</sub>, and its intensity increased further in TA-SnO<sub>2</sub>. This could be understood as another clear evidence of oxide formation by the anodic oxidation and also that of oxide lattice formation during the annealing process.

In conclusion, combining the XRD, XAS, and XPS analyses altogether, the surface and bulk phase of Sn foils had been transformed distinctively with two experimental processes. While the anodization serves as the surface-limited oxidization tool, the annealing in air helped the crystallization to SnO<sub>2</sub> phase of prepared nanostructure.

### **2.3.2. CO<sub>2</sub>RR characteristics of Sn oxide nanofilms**

The electrochemical CO<sub>2</sub>RR was evaluated in 0.5 M KHCO<sub>3</sub> electrolyte for prepared samples. The potential of each electrode was measured against Ag/AgCl potential ( $E^0 = 0.197$  V), employing graphite rod as counter electrode, and saturated Ag/AgCl (3 M KCl) reference electrode. From here, all the measured potentials are converted to RHE scale using the equation (1). Firstly, the CO<sub>2</sub>-catalyzing ability was briefly studied by comparing the CV shapes obtained from Ar- and CO<sub>2</sub>-purged electrolyte, using TA-SnO<sub>2</sub> electrode. The pH of each electrolyte after gas purging was 8.30 and 7.23, for Ar- and CO<sub>2</sub>-purged electrolyte, respectively. The measured CV results were depicted in Figure 2.11, ranging from 0 to -1.0 V. For the Ar-purged electrolyte, the measured current might come from HER, because of scarce CO<sub>2</sub> concentration near the electrodes. Meanwhile, the CO<sub>2</sub>RR and HER will occur simultaneously on CO<sub>2</sub>-purged electrolyte, with enriched CO<sub>2</sub> concentration. Along with the Sn<sup>0/IV</sup> redox signals near 0 V, the CV at Ar-purged electrolyte began to produce reduction current near -0.6 V and gradually increased with increasing overpotentials. [41] The same trend was observed on CO<sub>2</sub>-purged electrolyte, displaying same redox signal and reduction

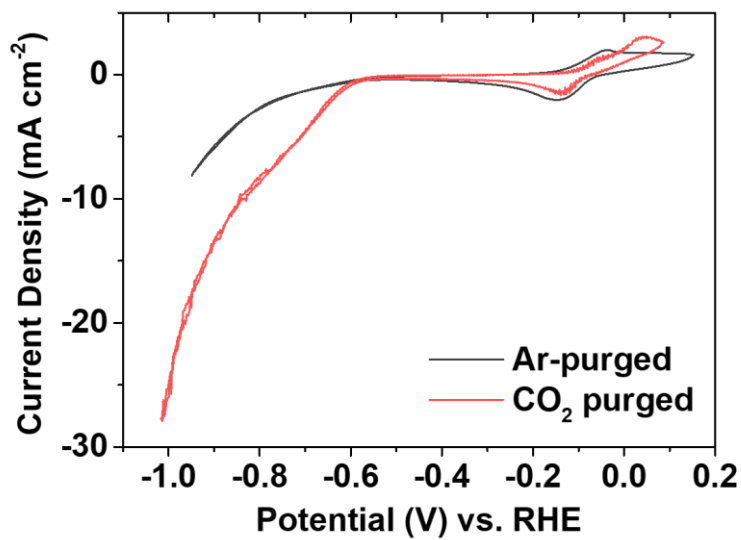


**Figure 2.11** The  $j$ -V polarization curve for the annealed foil electrode measured on Ar- or CO<sub>2</sub>-purged 0.5 M KHCO<sub>3</sub> electrolyte.

current with onset potential on same positions with Ar-purged one. Nonetheless, the observed current was much higher on CO<sub>2</sub>-purged electrolyte, (about 3 times higher in potential ranges below -0.6 V) proving the existence and its high current of CO<sub>2</sub> reduction on TA-SnO<sub>2</sub> electrode. Based on the possibility of CO<sub>2</sub>RR on prepared electrodes, we conducted CO<sub>2</sub>RR experiments employing H-cell structure. For the electrolysis, the homemade gas-tight cell with three-electrode configuration was designed, composed of anodic and cathodic compartments with Nafion<sup>®</sup> membrane as separator to prevent crossover of CO<sub>2</sub>RR products. [42, 43] All electrochemical hereafter was evaluated using the cell with iR-corrected potential using electrochemical impedance spectroscopy (EIS). The *x*-intercept value on EIS spectrum, which stands for external resistance ( $R_s$ ), was corrected using the *in situ* adjustment supported by NOVA program. Please note that the measured  $R_s$  ranges from 3.0 to 10  $\Omega$  for all electrodes tested.

Figure 2.12 depicts the linear sweep voltammogram span from 0 to -1.0 V in CO<sub>2</sub>-saturated 0.5 M KHCO<sub>3</sub> electrolyte, for bare Sn foil, AN-SnO<sub>x</sub>, TA-SnO<sub>2</sub>. Both AN-SnO<sub>x</sub> and TA-SnO<sub>2</sub> exhibited larger current densities compared to that of Sn foil, and it was the largest in the case of TA-SnO<sub>2</sub>, reaching over 100 mA cm<sup>-2</sup> on -1.0 V. For the precise evaluation of product distribution from electrocatalytic CO<sub>2</sub>RR of each sample, 1-hour long electrolysis was applied for a series of constant potential, chosen based on the results in Figure 2.11 (-0.7, -0.8, -0.9, -1.0 V). The gas chromatography (GC) and <sup>1</sup>H NMR were used for the quantification of gaseous and liquid CO<sub>2</sub>RR products, respectively. For our samples, only three products were detected: CO and H<sub>2</sub> on GC, and formate on NMR spectroscopy. Figure 2.13 illustrates the *i*-*t* characteristics of bare Sn, AN-SnO<sub>x</sub>, and TA-SnO<sub>2</sub> with their faradaic efficiencies (FEs) on each applied potential. The results were also summarized in Figure 2.14, for the easier recognition of obtained data. Please note that at least three identical experiments were done for each experimental

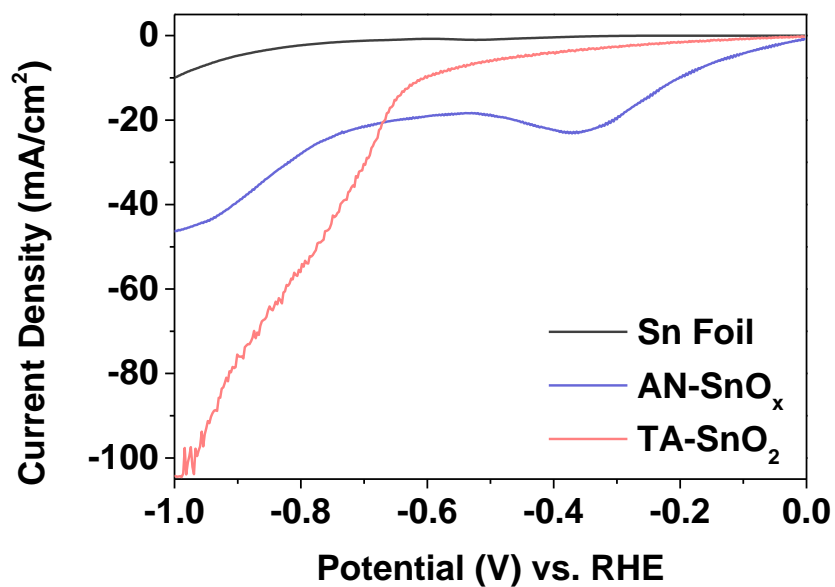


**Figure 2.12** Linear sweep voltammetry curves of Sn foil, AN-SnO<sub>x</sub>, TA-SnO<sub>2</sub>. The scan was done from 0 to -1.0 V.

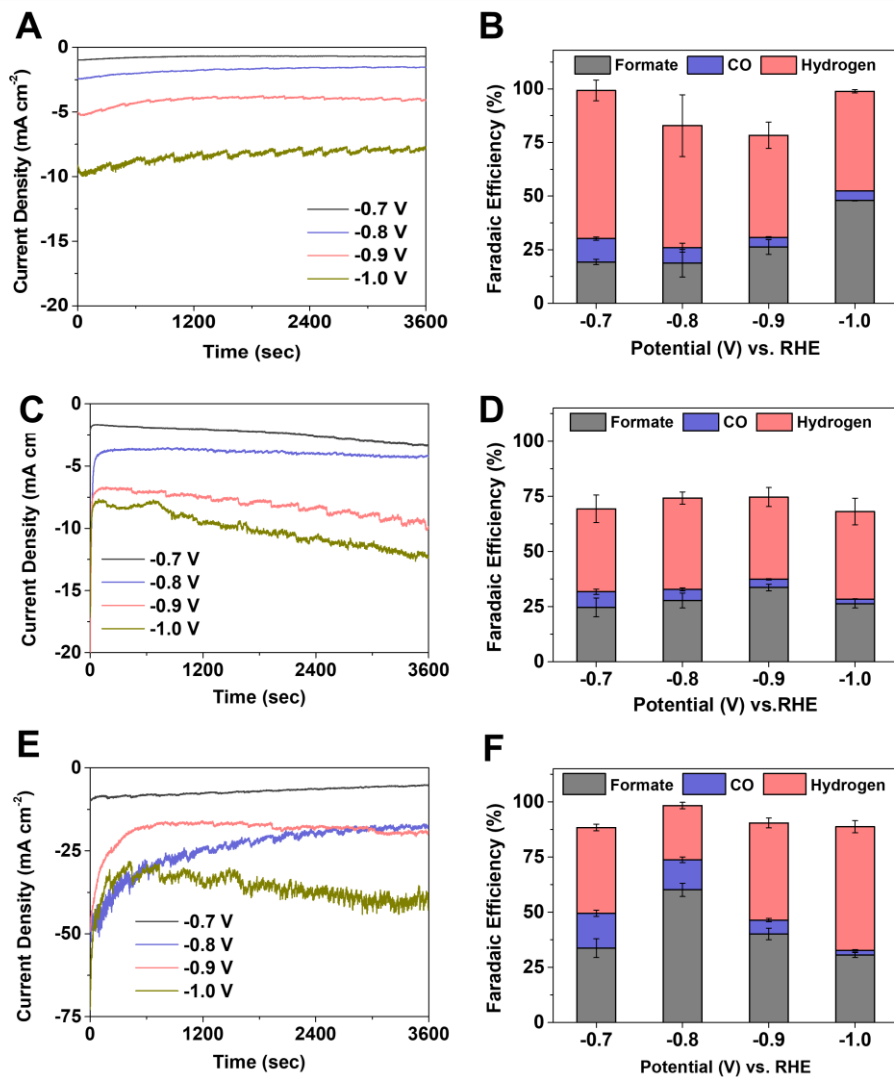


**Figure 2.13** The *i-t* characteristics and corresponding product distribution for each applied potential and sample type. (A-B) Bare Sn foil, (C-D) AN-SnO<sub>x</sub>, (E-F) TA-SnO<sub>2</sub>. For the evaluation of product distribution, three identical experiments were done for each potential, and averaged.

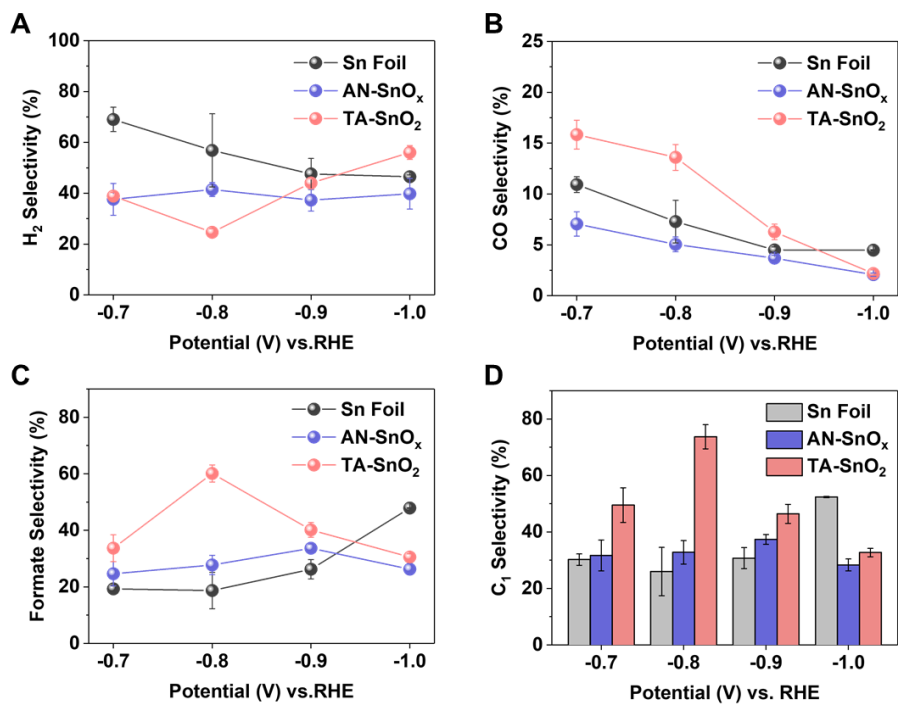


**Figure 2.14** The product selectivity distribution of Sn foil, AN-SnO<sub>x</sub>, TA-SnO<sub>2</sub> towards (A) H<sub>2</sub>, (B) CO, (C) Formate. (D) The total CO<sub>2</sub>RR conversion efficiency ( $FE_{CO} + FE_{formate}$ ) for each electrochemical test.

set. The averaged value was depicted on graph, with error bar expressing the standard deviation of those data. TA-SnO<sub>2</sub> electrode showed the highest total CO<sub>2</sub>RR conversion efficiency among all the samples from -0.7 to -0.9 V. From the data on Figure 2.14, it is clear that all samples produced formate as main CO<sub>2</sub>RR product. TA-SnO<sub>2</sub> has maximized formate production on -0.8 V, while AN-SnO<sub>x</sub> electrode had its maximum point on -0.9 V. The formate production of bare Sn electrode slowly increases from -0.7 V and maximizes up to 45% at -1.0 V. The TA-SnO<sub>2</sub> exhibited a 60.11% FE for formate on -0.8 V where other samples produced formate only lower than 30% on same potential. HER was a main competitive reaction, covering the remaining current besides formate. All electrodes display low CO production rates, only showing 16% of its maximum on annealed sample at -0.7 V. (Figure 2.14B) From these results, the formate partial current density ( $j_{\text{HCOO}^-}$ ) was calculated from formate selectivity and total current density at each potential. Figure 2.15 depicts the calculated  $j_{\text{HCOO}^-}$  for all samples. The annealed electrode showed the highest  $j_{\text{HCOO}^-}$  amongst prepared samples, based on its high total current density and formate selectivity. Interestingly, the formate selectivity and corresponding  $j_{\text{HCOO}^-}$  showed same maximum potential at -0.8 V.  $j_{\text{HCOO}^-}$  and faraday efficiency were then decreased concurrently with increased overpotentials, whereas the total current density was continued to increase at -0.9 and -1.0 V. [44] The highest observed  $j_{\text{HCOO}^-}$  was 33.66 mA cm<sup>-2</sup> on the annealed electrode, which is among the state-of-the-arts. (Table 2.2) This large  $j_{\text{HCOO}^-}$  of TA-SnO<sub>2</sub> demonstrates that our anodization-based synthetic method is a highly reliable and robust method to prepare the nanostructured oxide films with superior catalytic activity and selectivity. [35, 45-46]

For the results discussed above, it is surely noteworthy that TA-SnO<sub>2</sub> generated significantly improved  $j_{\text{HCOO}^-}$  compared to AN-SnO<sub>x</sub>, only with 20% EDLC compared to AN-SnO<sub>x</sub>. This indicates that the CO<sub>2</sub>-catalyzing ability of TA-SnO<sub>2</sub> is

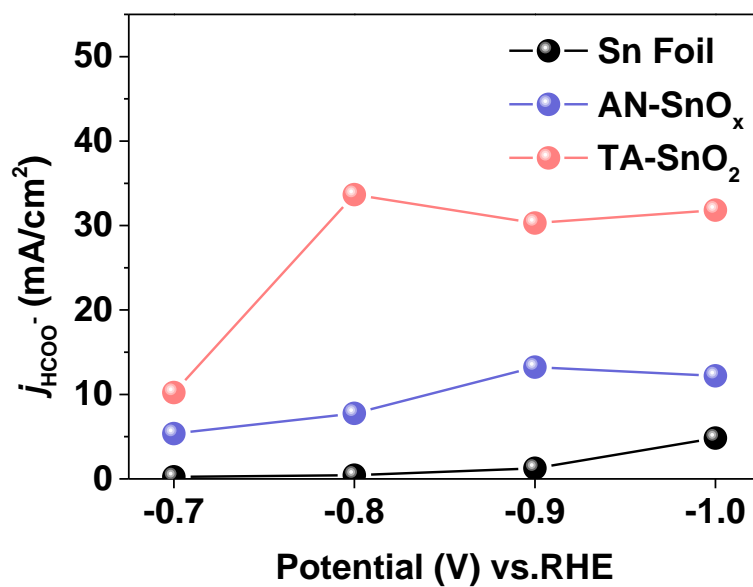


**Figure 2.15** The formate-generating partial current of each sample. Formate partial current was calculated with current density and formate selectivity on corresponding potential.

**Table 2.2** Comparison on electrochemical CO<sub>2</sub>RR performances of TA-SnO<sub>2</sub> and previously reported formate-producing Sn-based catalysts.

<b>Electrode Materials</b>	<b>Electrolyte</b>	<b>Potential (V vs. RHE)</b>	<b>FE<sub>formate</sub> (%)</b>	<b><i>j</i><sub>HCOO<sup>-</sup></sub> (mA/cm<sup>2</sup>)</b>	<b>References</b>
TA-SnO <sub>2</sub>	0.5 M KHCO <sub>3</sub>	-0.80	60.11	33.66	This work
Surface-engineered Sn foil	0.1 M KHCO <sub>3</sub>	-1.09	77.4	3.7	33
Sn dendrite/Sn foil	0.1 M KHCO <sub>3</sub>	-1.36	71.6	~23	34
Sn-Cu alloy	0.1 M KHCO <sub>3</sub>	-0.50	95	31.4	12
Ag-Sn core-shell alloy	0.5 M NaHCO <sub>3</sub>	-0.90	87.2	~25	14
Sn quantum sheet/graphene	0.1 M NaHCO <sub>3</sub>	-1.13	89	18.7	13
Sn/SnO <sub>x</sub> thin film	0.5 M NaHCO <sub>3</sub>	-0.7	~40	~1.6	22
SnS <sub>2</sub> -derived Sn/reduced graphene oxide	0.1 M KHCO <sub>3</sub>	-1.05	90	10.0	30
SnO <sub>2</sub> nanoparticles/carbon cloth	0.5 M NaHCO <sub>3</sub>	-1.07	85	45	28
Sn(S)/Au needle	0.1 M KHCO <sub>3</sub>	-0.75	95	51.2	31

much better than AN-SnO<sub>x</sub>, which might arise from the phase difference on the surface of those samples. This is clearly seen on Figure 2.16, comparing the current divided by the actual surface area of the electrode. Along with this, another clear difference between AN-SnO<sub>x</sub> and TA-SnO<sub>2</sub> lies on linear sweep voltammogram, on Figure 2.12. We could see clear reductive signal near -0.4 V of AN-SnO<sub>x</sub>, which could be attributable to the reduction of SnO<sub>2</sub>. [41] This also appears in bare Sn foil, as there exists a thin native oxide layer onto the Sn foil. (See enlarged curve in Figure 2.17) These results indicate a natural phenomenon: A reduction of Sn oxide arose by reductive environment. However, this reduction signal was not observed on TA-SnO<sub>2</sub>, which implies the strong resistance to reduction of prepared oxide on the surface. Based on Pourbaix diagram of Sn-O system at 298.15 K, Sn oxides are expected to be reduced to metallic state under the CO<sub>2</sub>RR operating condition; however, since the kinetic aspects were not considered on drawing Pourbaix diagram, it is possible that Sn oxides still remain metastable during the reaction. [47] (Figure 2.18) As mentioned above, it has been understood that the presence of oxide phase in Sn-based electrocatalysts is important for high activity and selectivity in CO<sub>2</sub>RR. [22] In that manner, we propose that the high CO<sub>2</sub>-to-formate performance of TA-SnO<sub>2</sub> could be ascribed from the remaining oxide, which could be remained from its larger tendency to remain as oxide rather than being reduced to metallic Sn.

For the proof of this hypothesis, we conducted several analyses for post-CO<sub>2</sub>RR TA-SnO<sub>2</sub> electrodes. Generally, on oxide materials, the color of the material and its phase is strongly correlated; with a clear example of the color difference between SnO and SnO<sub>2</sub>. (Figure 2.19) In this manner, if the oxide really exists with metastable state, this could be expressed as color change, or color remaining on the electrode surface during the CO<sub>2</sub>RR. Figure 2.20A shows the color of electrode during the electrolysis from pristine to -1.0 V. Interestingly, the

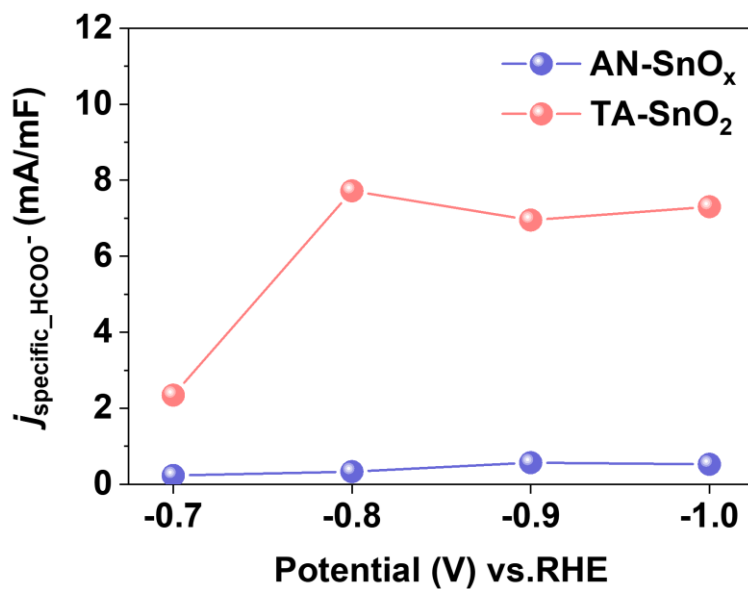


**Figure 2.16** Comparison between the specific CO<sub>2</sub>RR activities of AN-SnO<sub>x</sub> and TA-SnO<sub>2</sub> toward formate production by  $j_{\text{HCOO}^-}$  divided by EDLCs.

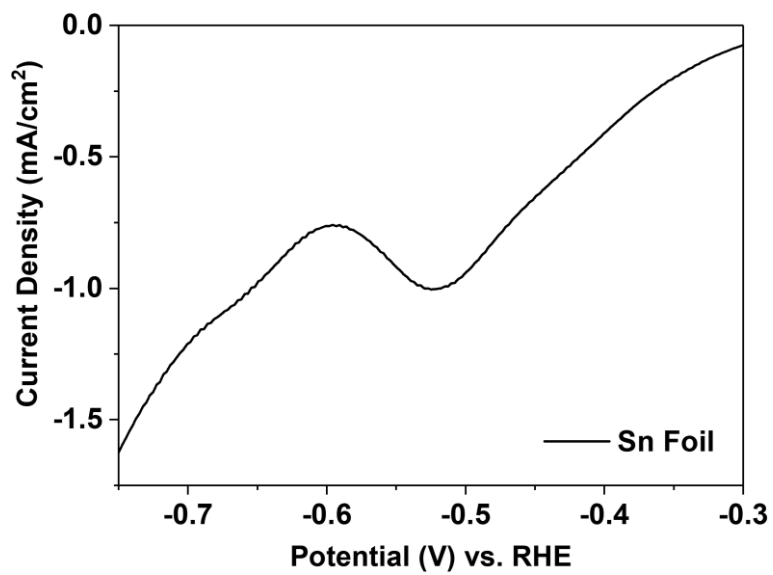


**Figure 2.17** Magnified version of the linear sweep voltammogram of bare Sn foil.

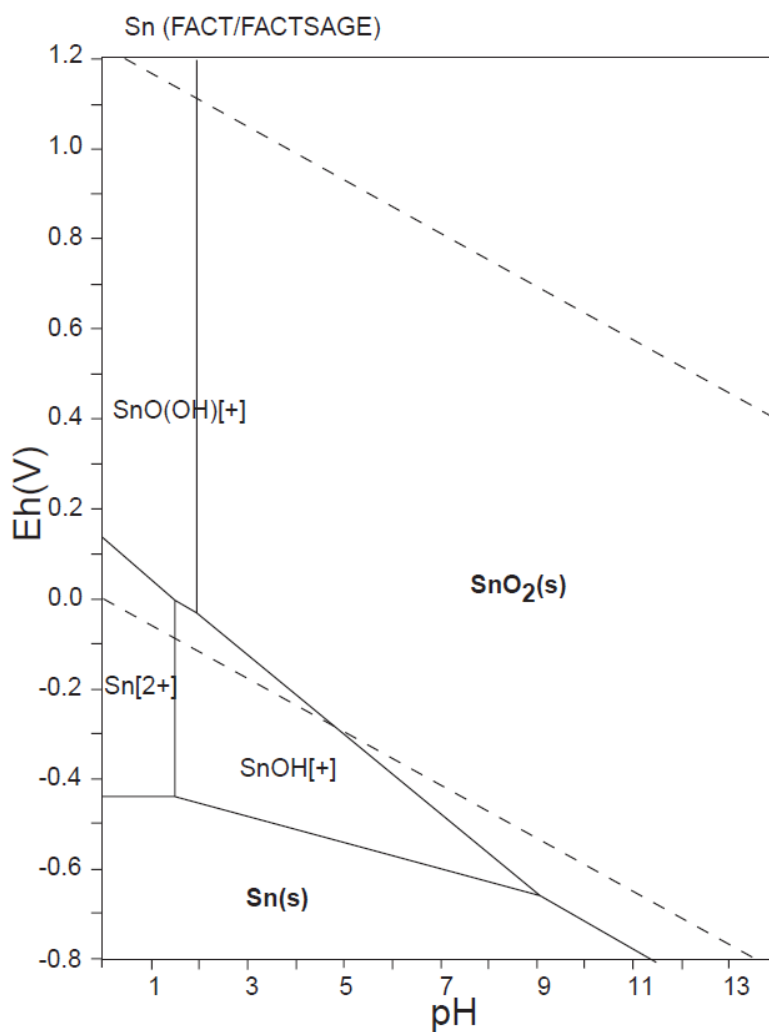


**Figure 2.18** The Pourbaix diagram for Sn-O-H system on 298.15 K. For the CO<sub>2</sub>RR condition, ( $pH = 7.23$ ,  $-0.8$  V) the Sn(s) should develop under thermodynamic viewpoint. Adapted from Ref. [47] (*Atlas of Electrochemical Equilibria in Aqueous Solutions*, 1966.)



**Figure 2.19** The digital photograph image displaying commercial SnO and SnO<sub>2</sub>.  
(from Sigma-Aldrich)

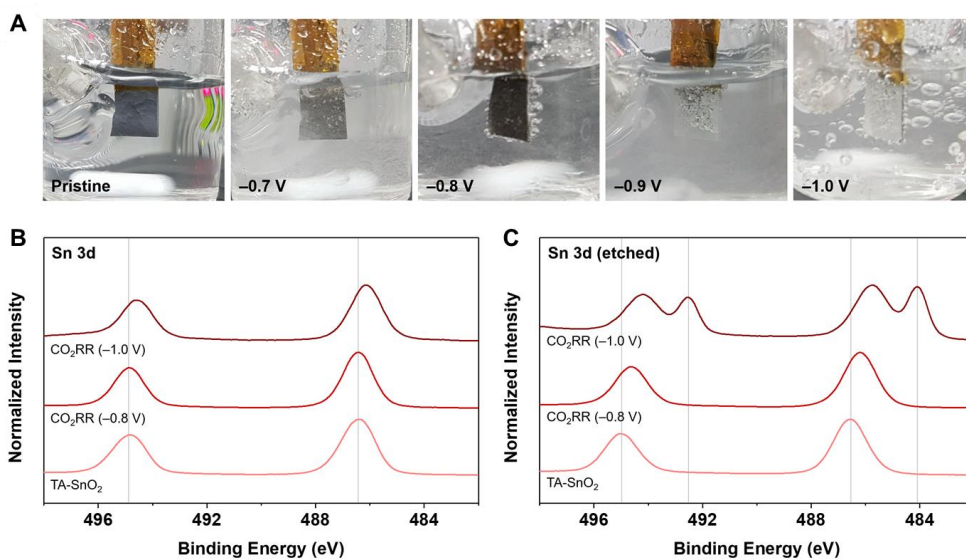


**Figure 2.20** During and post-CO<sub>2</sub>RR analyses on TA-SnO<sub>2</sub> electrode. (A) Digital photograph images of TA-SnO<sub>2</sub> before and during CO<sub>2</sub>RR under various applied potentials. The images were obtained after the stabilization of color changes for at least 5 min. (b, c) XPS Sn 3d spectra before and after CO<sub>2</sub>RR at -0.8 V and -1.0 V; XPS data in (c) were obtained after surface etching by 1 min of Ar sputtering.

black color which indicates the development of SnO phase near -0.8 V, and disappear below -0.8 V. In addition to this results, we carried out XPS and XRD analyses on TA-SnO<sub>2</sub> electrodes, to track the changes in chemical state, phase, and crystallinity of tin and oxygen elements, with respect to the introduced potentials on CO<sub>2</sub>RR. Figure 2.20B depicts the XPS spectra of TA-SnO<sub>2</sub> electrode before and after CO<sub>2</sub>RR on -0.8 and -1.0 V. On Sn 3d region, similar peak positions were found on pristine and -0.8 V-operated TA-SnO<sub>2</sub> electrodes, whereas clear shift toward low binding energy found on -1.0 V-operated sample. To attain more precise result, we obtained XPS spectra of same samples with Ar sputtering. The Ar sputtering about 1 minute slightly etches the surface of the electrode, where we suspect the formation of native oxide because of air exposure after the CO<sub>2</sub>RR. Figure 2.20C depicts the XPS spectra, where a clear difference could be observed on each sample. The gradual shift toward low binding energy is found on Sn 3d signals, with respect to the electrode applied higher overpotential. This implies that the surface suffers the reduction to some extent, even with metallic Sn peak on -1.0 V sample. The XRD was conducted on same samples, which displayed on Figure 2.21. The clear SnO<sub>2</sub>-assigned signal was observed on -0.8 V-operated TA-SnO<sub>2</sub>, which surely came from the highly resistant SnO phase during the CO<sub>2</sub>RR. The metallic Sn peaks are also observed on post-electrolysis samples, might from the metallic Sn layer underneath the anodized layer.

The results from XPS and XRD analyses show that the reduction of TA-SnO<sub>2</sub> takes place on the operating condition such as SnO<sub>2</sub>-to-Sn, but Sn oxide species with intermediate oxidation state, deviated from Sn<sup>IV</sup> state, could be presented at near-surface region of TA-SnO<sub>2</sub> when -0.8 V is applied, where -1.0 V sample shows full reduction to metallic state. From the article by Bocarsly *et al.*, the related phenomenon was deeply investigated exploiting attenuated total reflectance infrared spectroscopy. (ATR-IR) The authors said that in order for CO<sub>2</sub>-to-formate

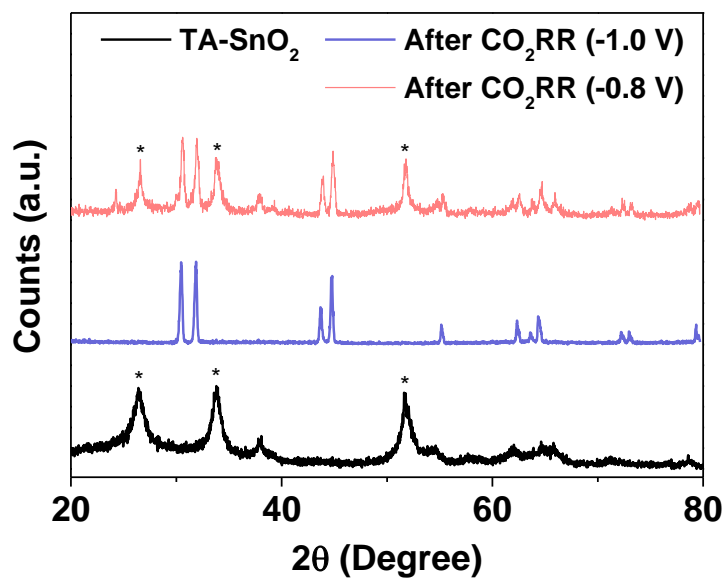


**Figure 2.21** XRD spectra of pristine and post-electrolysis TA-SnO<sub>2</sub> electrodes. The asterisk (\*) stands for the SnO<sub>2</sub> signals.

reaction to take place, formation of  $\text{Sn}^{\text{II}}$  species (in the form of  $\text{SnO}$  or  $\text{Sn}$  hydroxide) should take place first, and fixation of  $\text{CO}_2$  in the form of  $\text{Sn}(\text{H})\text{CO}_3$  followed by formate production occur continuously on  $\text{Sn}^{\text{II}}$  species. [48] Our observation – high  $\text{CO}_2\text{RR}$  activity and formate selectivity of  $\text{TA-SnO}_2$  (i.e. largest  $j_{\text{HCOO}^-}$ ) at  $-0.8\text{ V}$  – is in line with this report, as significant portion of  $\text{TA-SnO}_2$  seems to exist as  $\text{SnO}_2$  with further reduced oxide species at this potential (from both Figure 2.20 and 2.21).

## 2.4. Conclusions

In this study, self-supported  $\text{SnO}_2$  nanofilm was directly synthesized onto the  $\text{Sn}$  foil through successive oxidative synthetic approaches composed of anodization and thermal annealing in air. The anodization formed nanoarchitecture onto the surface of  $\text{Sn}$  foil, while the annealing process helped to transform prepared nanostructures into crystalline oxide phase. The  $\text{CO}_2\text{RR}$  performance was maximized when both oxidative processes were done. The finalized electrode showed maximized electrocatalytic  $\text{CO}_2\text{RR}$  activity, displaying maximum formate selectivity of 60.11% on 0.61 V overpotential. In that regard, the formate partial current density value of  $33.66\text{ mA cm}^{-2}$  was observed on annealed electrode, which is among the state-of-the-arts value. From the post- $\text{CO}_2\text{RR}$  analysis on annealed electrode, the improved performance originates from the metastable  $\text{Sn}^{\text{II}}$  phase of annealed sample. Based on the robustness and simplicity of our synthetic protocols with decent performances, we hope that this work could shed a light for efficient design and development of nanostructured oxide electrodes on  $\text{CO}_2\text{RR}$  electrolysis, for the practical application of  $\text{CO}_2\text{RR}$ .

## 2.5. References

[1] Mellmann, D.; Sponholz, P.; Junge, H.; Beller, M. Formic acid as a hydrogen storage material – development of homogeneous catalysts for selective hydrogen release. *Chem. Soc. Rev.* **2016**, *45*, 3954-3988.

[2] Müller, K.; Brooks, K.; Autrey, T. Hydrogen storage in formic acid: A comparison of process options. *Energy Fuels*, **2017**, *31*, 12603-12611.

[3] Verma, S.; Kim, B.; Jhong, H.-R.; Ma, S.; Kenis, P. J. A. A gross-margin model for defining technoeconomic benchmarks in the electroreduction of CO<sub>2</sub>. *ChemSusChem* **2016**, *9*, 1972-1979.

[4] Liu, A.; Gao, M.; Ren, X.; Meng, F.; Yang, Y.; Gao, L.; Yang, Q.; Ma, T. Current progress in electrocatalytic carbon dioxide reduction to fuels on heterogeneous catalysts. *J. Mater. Chem. A* **2020**, *8*, 3541-3562.

[5] Chen, Y.; Li, C. W.; Kanan, M. W. Aqueous CO<sub>2</sub> reduction at very low overpotential on oxide-derived Au nanoparticles. *J. Am. Chem. Soc.* **2012**, *134*, 19969-19972.

[6] Feng, X.; Jiang, K.; Fan, S.; Kanan, M. W. Grain-boundary-dependent CO<sub>2</sub> electroreduction activity. *J. Am. Chem. Soc.* **2015**, *137*, 4606-4609.

[7] Kim, C.; Jeon, H. S.; Eom, T.; Jee, M. S.; Kim, H.; Friend, C. M.; Min, B. K.; Hwang, Y. J. Achieving selective and efficient electrocatalytic activity for CO<sub>2</sub> reduction using immobilized silver nanoparticles. *J. Am. Chem. Soc.* **2015**, *137*, 13844-13850.

[8] Sun, D.; Xu, X.; Qin, Y.; Jiang, S. P.; Shao, Z. Rational design of Ag-based catalysts for the electrochemical CO<sub>2</sub> reduction to CO: A review. *ChemSusChem* **2020**, *13*, 39-58.

[9] Ju, W.; Bagger, A.; Hao, G.-P.; Varela, A. S.; Sinev, I.; Bon, V.; Cuenya, B. R.; Kaskel, S.; Rossmeisl, J.; Strasser, P. Understanding activity and selectivity of metal-nitrogen-doped carbon catalysts for electrochemical reduction of CO<sub>2</sub>. *Nat. Commun.* **2017**, *8*, 944.

[10] Yang, H. B.; Hung, S.-F.; Liu, S.; Yuan, K.; Miao, S.; Zhang, L.; Huang, X.; Wang, H.-Y.; Cai, W.; Chen, R.; Gao, J.; Yang, X.; Chen, W.; Huang, Y.; Chen, H. M.; Li, C. M.; Zhang, T.; Liu, B. Atomically dispersed Ni(I) as the active site for

electrochemical CO<sub>2</sub> reduction. *Nat. Energy* **2018**, *3*, 140-147.

[11] Hori, Y. *Modern Aspects of Electrochemistry*, Springer, New York, NY, **2008**.

[12] Zhang, X.; Ji, Y.; Tang, J.; Wang, J.; Liu, B.; Steinrück, H.-G.; Lim, K.; Li, Y.; Toney, M. F.; Chan, K.; Cui, Y. Theory-guided Sn/Cu alloying for efficient CO<sub>2</sub> electroreduction at low overpotentials. *Nat. Catal.* **2019**, *2*, 55-61.

[13] Lei, F.; Liu, W.; Sun, Y.; Xu, J.; Liu, K.; Liang, L.; Yao, T.; Pan, B.; Wei, S.; Xie, Y. Metallic tin quantum sheets confined in graphene toward high-efficiency carbon dioxide electroreduction. *Nat. Commun.* **2016**, *7*, 12697.

[14] Luc, W.; Collins, C.; Wang, S.; Xin, H.; He, K.; Kang, Y.; Jiao, F. Ag-Sn bimetallic catalyst with a core-shell structure for CO<sub>2</sub> reduction. *J. Am. Chem. Soc.* **2017**, *139*, 1885-1893.

[15] Ma, W.; Xie, S.; Zhang, X.-G.; Sun, F.; Kang, J.; Jiang, Z.; Zhang, Q.; Wu, D.-Y.; Wang, Y. Promoting electrocatalytic CO<sub>2</sub> reduction to formate via sulfur-boosting water activation on indium surfaces. *Nat. Commun.* **2019**, *10*, 892.

[16] Zhang, Z.; Ahmad, F.; Zhao, W.; Yan, W.; Zhang, W.; Huang, H.; Ma, C.; Zeng, J. Enhanced electrocatalytic reduction to CO<sub>2</sub> via chemical coupling between indium oxide and reduced graphene oxide. *Nano Lett.* **2019**, *19*, 4029-4034.

[17] Detweiler, Z. M.; White, J. L.; Bernasek, S. L.; Bocarsly, A. B. Anodized indium metal electrodes for enhanced carbon dioxide reduction in aqueous electrolyte. *Langmuir* **2014**, *30*, 7593-7600.

[18] Koh, J. H.; Won, D. H.; Eom, T.; Kim, N.-K.; Jung, K. D.; Kim, H.; Hwang, Y. J.; Min, B. K. Facile CO<sub>2</sub> electro-reduction to formate via oxygen bidentate intermediate stabilized by high-index planes of Bi dendrite catalyst. *ACS Catal.* **2017**, *7*, 5071-5077.

[19] Zhang, E.; Wang, T.; Yu, K.; Liu, J.; Chen, W.; Li, A.; Rong, H.; Liu, R.; Ji, S.; Zheng, X.; Wang, Y.; Zheng, L.; Chen, C.; Wang, D.; Zhang, J.; Li, Y. Bismuth single atoms resulting from transformation of metal-organic frameworks and their use as electrocatalysts for CO<sub>2</sub> reduction. *J. Am. Chem. Soc.* **2019**, *141*, 16569-16573.

[20] Su, P.; Xu, W.; Qui, Y.; Zhang, T.; Li, X.; Zhang, H. Ultrathin bismuth nanosheets as a highly efficient CO<sub>2</sub> reduction electrocatalysts. *ChemSusChem*

2018, 11, 848-853.

[21] Atifi, A.; Boyce, D. W.; DiMeglio, J. L.; Rosenthal, J. Directing the outcome of CO<sub>2</sub> reduction at bismuth cathodes using varied ionic liquid promoters. *ACS Catal.* **2018**, 8, 2857-2863.

[22] Chen, Y.; Kanan, M. W. Tin oxide dependence of the CO<sub>2</sub> reduction efficiency on tin electrodes and enhanced activity for tin/tin oxide thin-film catalysts. *J. Am. Chem. Soc.* **2012**, 134, 1986-1989.

[23] Feaster, J. T.; Shi, C.; Cave, E. R.; Hatsukade, T.; Abram, D. N.; Kuhl, K. P.; Hahn, C.; Nørskov, J. K.; Jaramillo, T. F. Understanding selectivity for the electrochemical reduction of carbon dioxide to formic acid and carbon monoxide on metal electrodes. *ACS Catal.* **2017**, 7, 4822-4827.

[24] Zhang, Q.; Zhang, Y.; Mao, J.; Liu, J.; Zhou, Y.; Guay, D.; Qiao, J. Electrochemical reduction of CO<sub>2</sub> by SnO<sub>x</sub> nanosheets anchored on multiwalled carbon nanotubes with tunable functional groups. *ChemSusChem* **2019**, 12, 1443-1450.

[25] Yiliguma; Wang, Z.; Yang, C.; Guan, A.; Shang, L.; Al-Enizi, A. M.; Zhang, L.; Zheng, G. Sub-5 nm SnO<sub>2</sub> chemically coupled hollow carbon spheres for efficient electrocatalytic CO<sub>2</sub> reduction. *J. Mater. Chem. A* **2018**, 6, 20121-20127.

[26] Liang, C.; Kim, B.; Yang, S.; Liu, Y.; Woellner, C. F.; Li, Z. Vajtai, R.; Yang, W.; Wu, J.; Kenis, P. J. A.; Ajayan, P. M. High efficiency electrochemical reduction of CO<sub>2</sub> beyond the two-electron transfer pathway on grain boundary rich ultra-small SnO<sub>2</sub> nanoparticles. *J. Mater. Chem. A* **2018**, 6, 10313-10319.

[27] Kumar, B.; Atla, V.; Brian, J. P.; Kumari, S.; Nguyen, T. Q.; Sunkara, M.; Spurgeon, J. M. Reduced SnO<sub>2</sub> porous nanowires with a high density of grain boundaries as catalysts for efficient electrochemical CO<sub>2</sub>-into-HCOOH conversion. *Angew. Chem. Int. Ed.* **2017**, 56, 3645-3649.

[28] Li, F.; Chen, L.; Knowles, G. P.; MacFarlane, D. R.; Zhang, J. Hierarchical mesoporous SnO<sub>2</sub> nanosheets on carbon cloth: A robust and flexible electrocatalysts for CO<sub>2</sub> reduction with high efficiency and selectivity. *Angew. Chem. Int. Ed.* **2017**, 56, 505-509.

[29] Choi, Y.-W.; Scholten, F.; Siven, I.; Cuenya, B. R. Enhanced stability and CO/formate selectivity of plasma-treated SnO<sub>x</sub>/AgO<sub>x</sub> catalysts during CO<sub>2</sub>

electroreduction. *J. Am. Chem. Soc.* **2019**, *141*, 5261-5266.

[30] Li, F.; Chen, L.; Xue, M.; Williams, T.; Zhang, Y.; MacFarlane, D. R.; Zhang, J. Towards a better Sn: Efficient electrocatalytic reduction of CO<sub>2</sub> to formate by Sn/SnS<sub>2</sub> derived from SnS<sub>2</sub> nanosheets. *Nano Energy* **2017**, *31*, 270-277.

[31] Zheng, X.; Luna, P. D.; Arquer, F. P. G.; Zhang, B.; Becknell, N.; Ross, M. B.; Li, Y.; Banis, M. N.; Li, Y.; Liu, M.; Voznyy, O.; Dinh, C. T.; Zhuang, T.; Stadler, P.; Cui, Y.; Du, X.; Yang, P.; Sargent, E. H. Sulfur-modulated tin sites enable highly selective electrochemical reduction of CO<sub>2</sub> to formate. *Joule* **2017**, *1*, 794-805.

[32] Gu, J.; Héroguel, F.; Luterbacher, J.; Hu, X. Densely packed, ultra small SnO nanoparticles for enhanced activity and selectivity in electrochemical CO<sub>2</sub> reduction. *Angew. Chem. Int. Ed.* **2018**, *57*, 2943-2947.

[33] Daiyan, R.; Lu, X.; Ng, Y. H.; Amal, R. Surface engineered tin foil for electrocatalytic reduction of carbon dioxide to formate. *Catal. Sci. Technol.* **2017**, *7*, 2542-2550.

[34] Won, D. H.; Choi, C. H.; Chung, J.; Chung, M. W.; Kim, E.-H.; Woo, S. I. Rational design of a hierarchical tin dendrite electrode for efficient electrochemical reduction of CO<sub>2</sub>. *ChemSusChem* **2015**, *8*, 3092-3098.

[35] Kim, J.-Y.; Kang, J. S.; Shin, J.; Kim, J.; Han, S.-J.; Park, J.; Min, Y.-S.; Ko, M. J.; Sung, Y.-E. Highly uniform and vertically aligned SnO<sub>2</sub> nanochannel arrays for photovoltaic applications. *Nanoscale* **2015**, *7*, 8368-8377.

[36] Yuan, Z. F.; Mukai, K.; Takagi, K.; Ohtaka, M.; Huang, W. L.; Liu, Q. S. Surface Tension and Its Temperature Coefficient of Molten Tin Determined with the Sessile Drop Method at Different Oxygen Partial Pressures. *J. Colloid Interface Sci.* **2002**, *254*, 338-345.

[37] Seah, M. P.; Dench, W. A. Quantitative Electron Spectroscopy of Surfaces: A Standard Data Base for Electron Inelastic Mean Free Paths in Solids. *Surf. Interface Anal.* **1979**, *1*, 2-11.

[38] Kwoka, M.; Ottaviano, L.; Passacantando, M.; Santucci, S.; Czempik, G.; Szuber, J. XPS study of the surface chemistry of L-CVD SnO<sub>2</sub> thin films after oxidation. *Thin Solid Films* **2005**, *490*, 36-42.

- [39] Chuang, T. J.; Brundle, C. R.; Rice, D. W. Interpretation of the X-ray photoemission spectra of cobalt oxides and cobalt oxide surfaces. *Surf. Sci.* **1976**, *59*, 413-429.
- [40] Wang, D.; Yang, J.; Liu, J.; Li, X.; Li, R.; Cai, M.; Sham, T.-K.; Sun, X. Atomic Layer Deposited Coatings to Significantly Stabilize Anodes for Li Ion Batteries: Effects of Coating Thickness and the Size of Anode Particles. *J. Mater. Chem. A* **2014**, *2*, 2306-2312.
- [41] Nakayama, S.; Sugihara, T.; Matsumoto, J.; Notoya, T.; Osakai, T. Chemical state analysis of tin oxide films by voltammetric reduction. *J. Electrochem. Soc.* **2011**, *158*, C341-C345.
- [42] Zhao, C.; Wang, J. Electrochemical reduction of CO<sub>2</sub> to formate in aqueous solution using electro-deposited Sn catalysts. *Chem. Eng. J.* **2016**, *293*, 161-170.
- [43] Kortlever, R.; Shen, J.; Schouten, K. J. P.; Calle-Vallejo, F.; Koper, M. T. M. Catalysts and reaction pathways for the electrochemical reduction of carbon dioxide. *J. Phys. Chem. Lett.* **2015**, *6*, 4073-4082.
- [44] Kuhl, K. P.; Cave, E. R.; Abram, D. N.; Jaramillo, T. F. New insights into the electrochemical reduction of carbon dioxide on metallic copper surface. *Energy Environ. Sci.* **2012**, *5*, 7050-7059.
- [45] Roy, P.; Berger, S.; Schmuki, P. TiO<sub>2</sub> Nanotubes: Synthesis and Applications. *Angew. Chem. Int. Ed.* **2011**, *50*, 2904-2939.
- [46] Nah, Y.-C.; Ghicov, A.; Kim, D.; Berger, S.; Schmuki, P. TiO<sub>2</sub>-WO<sub>3</sub> Composite Nanotubes by Alloy Anodization: Growth and Enhanced Electrochromic Properties. *J. Am. Chem. Soc.* **2008**, *130*, 16154-16155.
- [47] Pourbaix, M. *Atlas of Electrochemical Equilibria in Aqueous Solutions*, Pergamon Press, Brussels, **1966**.
- [48] Baruch, M. F.; Pander III, J. E.; White, J. L.; Bocarsly, A. B. Mechanistic insights into the reduction of CO<sub>2</sub> on tin electrodes using in situ ATR-IR spectroscopy. *ACS Catal.* **2015**, *5*, 3148-3156.

# Chapter 3. Oxide-Derived Zn Nanoarchitecture for CO<sub>2</sub> Electroreduction to CO

## 3.1. Introduction

The one of the important aspects of CO<sub>2</sub>RR is, entirely different approaches should be considered for designing the catalysts for different target compounds. This was discussed briefly on first chapter, and written at last chapter in detail, in the case of formate. For CO, basic assumption is, pure noble metals such as Au or Ag already achieve a CO production with decent selectivity over 60%. [1] Hence, the aim of the research could be differentiated to two stems: 1) maximizing the selectivity of CO or 2) seeking more economic substitutes for noble metal counterparts.

For the maximization of CO production, there have been numerous approaches to (physico-)chemically tune the energetics or kinetics catalyzing CO<sub>2</sub>. Tuning of catalysts with surface-coating chemicals is a representative approach, applied successfully on both Au and Ag. [2-3] On the other hands, considering the scarcity and high costs of noble metals, a number of alternative materials have been studied. Zn-based materials are among them, based on its innate CO<sub>2</sub>-catalyzing ability on its metallic form. [1] Attributed to its low price and non-toxicity along with aforementioned catalyzing ability, the Zn-based materials have been regarded as a promising alternative to Au or Ag. [4] Nanostructuring was a key research idea for Zn-based materials, which proved to be successful on other metals previously. Woo *et al.* has proposed a hexagonal shaped Zn catalyst for efficient CO<sub>2</sub>RR catalyst, benefited from its preferential (101) facet. [5] DFT calculation suggests the (101) facet is favorable for CO<sub>2</sub>RR, because of a lower reaction barrier and a more stabilized \*COOH intermediate on (101) facet. The prepared catalyst exhibited over 95% CO selectivity prolonged over 30 h operation. Likewise, various

nanostructured Zn materials such as electrodeposited Zn, porous Zn, and dendritic Zn were suggested, for the efficient CO<sub>2</sub>RR catalyzation. [6-10] The *in situ* reduction method (which typically known as ‘oxide-derived’ catalyst), which already researched on other metals by Kanan *et al.*, was also proved as a nice strategy for Zn-based materials. [11-12] Nanostructuring induced by *in situ* reduction creates randomly structured high index facets or grain boundaries, which are regarded as better CO<sub>2</sub>RR active sites than their low-indexed ones. ZnO nanosheet, and interconnected ultrasmall ZnO nanoparticles based on Li-electrochemical tuning are good examples. (Figure 3.1) [13-14] Along with these methods, alloying with other metals, [15-18], single-atom-based Zn-N<sub>4</sub> catalysts, [19-20] and adhesion adlayer [21] were also reported for the efficient CO<sub>2</sub>RR using Zn-based catalysts.

Herein, we propose an oxide-derived Zn nanoarchitecture directly grown on gas-diffusion electrode (GDL), for the efficient CO<sub>2</sub>-to-CO catalyzation. The *in situ* reduction on CO<sub>2</sub>RR operating condition creates completely different Zn morphology with Zn foil, which exhibits much better CO<sub>2</sub> catalyzing ability than its bulk counterpart. From potential-controlled electrolysis, the maximum CO selectivity of 75.79% was obtained on ZnO nanostructure at -1.0 V. From Tafel analysis and related electrochemical analysis, we found experimental evidences on the changed rate-determining step (RDS) on our electrode, which trigger the improved performance on our ZnO electrode. In addition, by growing ZnO nanotube structure directly onto the GDL surface, the full cell operation using flow-cell architecture was realized without any additional treatments on pristine ZnO electrode. By applying a cell voltage of 2.7 V, the prepared nanostructured electrode could successfully convert CO<sub>2</sub> into CO stably by maintaining CO selectivity over 75% for 2-hour electrolysis, exhibiting current density about 80 mA cm<sup>-2</sup>.

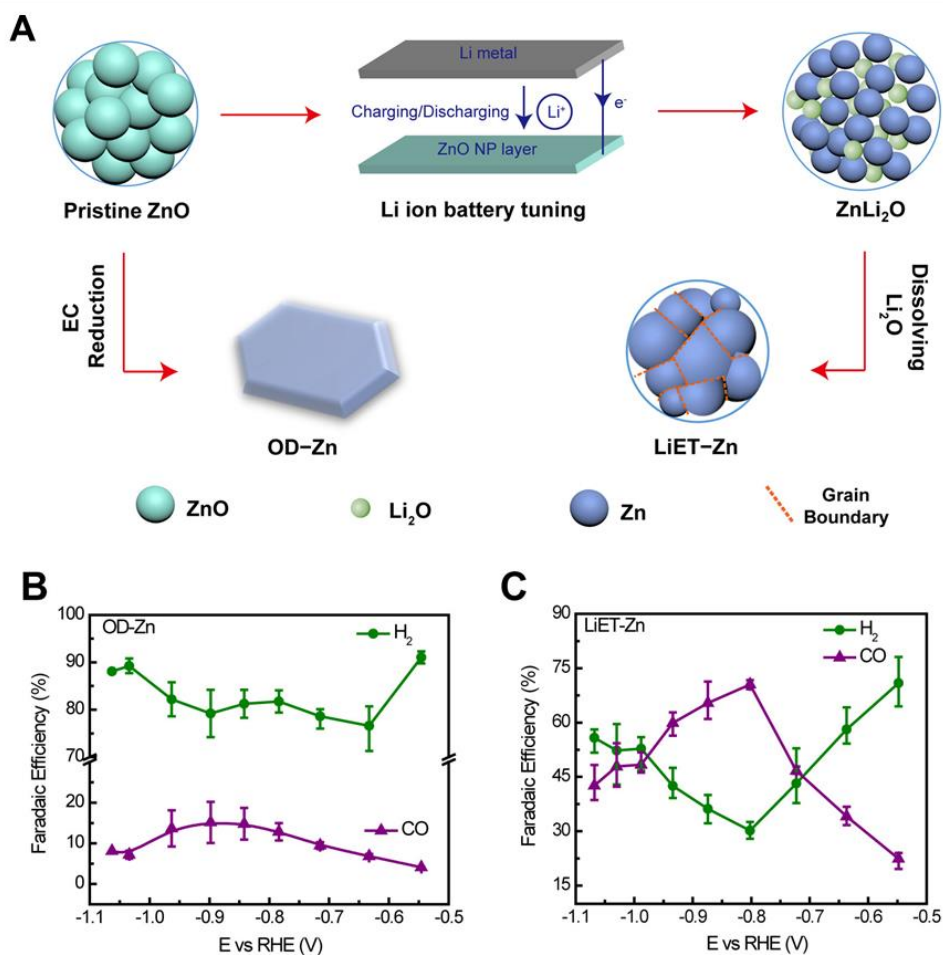


**Figure 3.1** Li electrochemical tuning of ZnO. (A) The schematic illustration for the preparation method based on Li electrochemical tuning. The product distribution of (B) OD-Zn and (C) LiET-Zn from CO<sub>2</sub>-saturated 0.1 M KHCO<sub>3</sub> electrolyte. Adapted from Ref. [14] (*ACS Nano* **2017**, *11*, 6451-6458).

## **3.2. Experimental Section**

### **3.2.1. Materials**

Zn foil (99.999%, 0.25 mm), 50-nm sized ZnO nanoparticles, zinc nitrate hexahydrate, hexamethylenetetramine (HMTA), and ammonium hydroxide solution (25%) were purchased from Sigma-Aldrich. GDL (0.32 mm thick, 30-A3) with a PTFE coating layer was purchased from JNT. All materials and reagents were used without further purifications.

### **3.2.2. Synthesis of ZnO nanorod arrays onto the GDL**

The 50-nm sized ZnO nanoparticles were dispersed in ethanol (1 wt%), and coated onto the PTFE-side of GDL (2 x 1 cm<sup>2</sup>) using the spin coating method. (3000 rpm, 60 s) After the spin coating, the ZnO-coated GDL were dried at 80 °C for 5 min, to evaporate the remaining ethanol. ZnO nanorod arrays were hydrothermally synthesized on the surface of GDL, using the pre-coated ZnO array as a seed layer. [22-24] The growth solution containing zinc nitrate hexahydrate (0.025 M), HMTA (0.0125 M), ammonium hydroxide solution and ZnO-coated GDLs were transferred into the Teflon-lined autoclave. The solution filled a volume about 80% of the total volume of autoclave chamber. The hydrothermal synthesis was conducted at 80 °C for 12 h. Because of the existing seed layer and the hydrophobic character of PTFE-coated layer, the ZnO can exclusively grow onto the ZnO-coated layer. After the hydrothermal synthesis, the ZnO nanorod arrays on GDL (ZnO/GDL) was taken out and rinsed with deionized water several times, and dried by N<sub>2</sub> gas blowing.

### **3.2.3. Characterizations of ZnO/GDL electrode**

The morphology of ZnO electrodes were examined using field-emission scanning electron microscopy (FE-SEM, Carl-Zeiss), along with energy dispersive X-ray spectroscopy (EDX) analysis verifying chemical composition of ZnO/GDL

structure. The XRD spectra were collected by Rigaku D-MAX2500-PC. The chemical state of each element was examined by X-ray photoelectron spectroscopy (XPS, AXIS SUPRA, Kratos) equipped with Al-K $\alpha$  source (1486.7 eV). The modified Auger parameter ( $\alpha$ ) of both samples were evaluated by the addition of maximum energy positions of Zn 2p<sub>3/2</sub> region and Zn LMM region. The binding energy value was used for Zn 2p region, whereas the kinetic energy value was used for Zn LMM region.

#### **3.2.4. Electrochemical reduction of ZnO/GDL electrode**

The electrochemical CO<sub>2</sub>RR performance of each electrode was evaluated using three-electrode configuration with a potentiostat. (PGSTAT302N, Autolab) The homemade H-type cell comprising anodic and cathodic compartments were used for electrochemical analyses. The working electrode (Zn foil or ZnO nanostructure) and saturated Ag/AgCl reference electrode (RE-1CP, ALS) were equipped on cathodic compartment, and graphite rod was used for counter electrode in the anodic compartment. The proton-conducting Nafion<sup>®</sup> 117 membrane was used to separate two cell parts chemically while connecting them electrically. The 0.5 M KHCO<sub>3</sub> aqueous electrolyte saturated with CO<sub>2</sub> was used for electrochemical analyses, where cathodic compartment was continuously purged with CO<sub>2</sub> during electrolysis with a speed of 20 sccm. (standard cubic centimeter per minute; cm<sup>3</sup> min<sup>-1</sup>) For the sufficient supply of CO<sub>2</sub> on the electrode surface, the cathodic compartment was continuously stirred with 400 rpm. The electrochemical CO<sub>2</sub>RR performances were evaluated by applying constant potential to the electrodes with the duration of 1 hour. The electrolysis was done from -0.6 V to -1.1 V for each electrode, with iR correction using pre-obtained EIS data.

### 3.2.5. Product quantification

The generated products were quantified by GC (7890B, Agilent) for gaseous products, and  $^1\text{H}$  NMR (AVANCE 600, Bruker) for liquid products. The FID and TCD detect CO and  $\text{H}_2$  amount by directly collecting  $\text{CO}_2$  stream generating from reactor in real-time. The aforementioned formula for FE calculation (from section 2.2.3) evaluated the selectivity for each product. The sample for  $^1\text{H}$  NMR was prepared by mixing 450  $\mu\text{L}$  aliquot of electrolyte from 1-hour electrolysis with 50  $\mu\text{L}$  of 1% 3-(trimethylsilyl)-1-propanesulfonic acid (DSS) in  $\text{D}_2\text{O}$  (Sigma-Aldrich). Normalized FE could be calculated from the equation (1) written below:

$$\text{FE}_{i,\text{norm}} = \frac{\text{FE}_i}{\sum_i \text{FE}_i} \quad (i = \text{CO}, \text{H}_2, \text{formate}) \quad (1)$$

### 3.2.6. Electrochemical mechanism investigation

The electrokinetic aspects on  $\text{CO}_2$ -to-CO catalyzed reaction was evaluated using Tafel analysis. The overpotential ( $\eta$ ) was calculated using the following equation, substituting standard reduction potential ( $E^0$ ) value of -0.11 V for the CO production: [25]

$$\eta = |E - E^0| \quad (2)$$

To obtain the Tafel slope, the plot of  $\eta$  (partial current for CO production) against logarithm of  $j_{\text{CO}}$  was drawn, and the slope was acquired from the linear region.

### 3.2.7. Full cell operation using flow-cell architecture

The MEA-based flow cell was designed to measure the  $\text{CO}_2\text{RR}$  activity of catalysts with a practical operating condition. (Figure 3.2) [26] The anion exchange membrane (Sustainion<sup>®</sup> X37-50 RT, Dioxide Materials) was sandwiched between a cathode and anode such that both catalyst layers were facing the membrane. The

size of each electrode was  $2.5 \times 2.5 \text{ cm}^2$ , while the size of membrane was  $3 \times 3 \text{ cm}^2$ . Prepared ZnO-based electrode was directly used as cathode, while the pressed Ni foam was used for anode. On both side, the current collectors with serpentine type flow fields cover backside of electrodes making electrical connection toward the potentiostat, and finally, end plates on each side tighten the whole structure to prevent any leakages. The active area of the cell was  $5.0 \text{ cm}^2$ , evaluated from total cross-sectional area of flow field. On operation, gaseous  $\text{CO}_2$  was continuously fed on cathodic side with a speed of 15 sccm, and 1 M KOH electrolyte circulates through the anodic compartment. The peristaltic pump (HV-77921-75, Masterflex) was used for the controlled circulation of 1 M KOH electrolyte with a speed of  $10 \text{ mL min}^{-1}$ . The outlet of cathodic flow field was directly connected to the GC, for the quantification of gaseous products.

### **3.3. Results and Discussion**

#### **3.3.1. Synthesis and characterizations of ZnO nanostructure**

The ZnO nanostructures were grown onto the surface of microporous layer (MPL) side of the GDL, employing ZnO seed layer mediated hydrothermal synthesis. [22-24] Dense ZnO nanoparticle array was deposited onto the GDL introducing ZnO dispersed ethanol solution, and worked for the foundation where nanorod structures starts to grow. Using zinc nitrate hexahydrate ( $\text{Zn}(\text{NO}_3)_2$ ) as a metal precursor, the nanorod morphology was constructed based on base-catalyzed hydrolysis and condensation on hydrothermal reaction conditions. The synthesized catalyst was denoted as 'ZnO/GDL'. Figure 3.3 depicts the SEM images of ZnO/GDL. Top-side view (Figure 3.3A and B) clearly illustrates the dense layer composed of ZnO nanorods. The cross-sectional SEM image on Figure 3.3C clearly displays the ZnO nanorods grown onto the MPL side of GDL. Ascribable to the seed layer composed of ZnO nanoparticles, the ZnO nanorod arrays could be successfully prepared even onto the uneven surface of MPL layer. Besides of SEM images, the energy

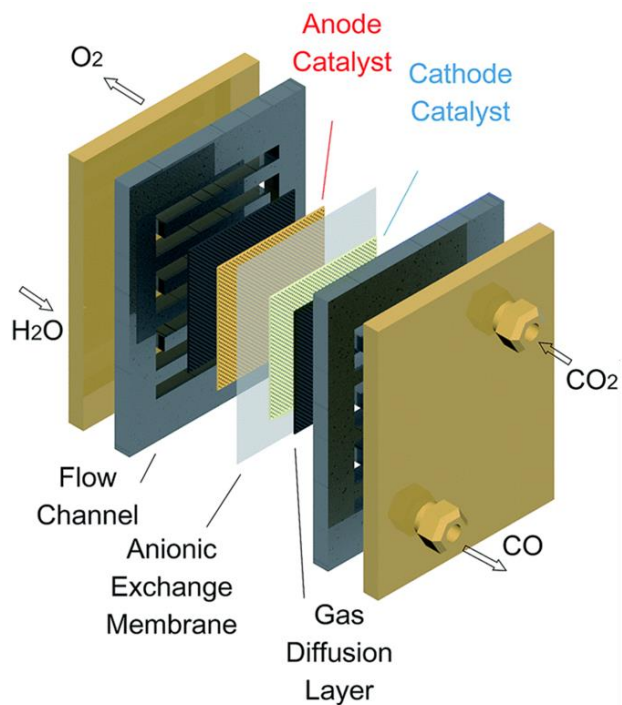


**Figure 3.2** The illustration of MEA-based CO<sub>2</sub>RR flow cell design. Reproduced from Ref. [26] (*J. Mater. Chem. A* **2019**, 7, 10651-10661.)

dispersive X-ray spectroscopy images were collected for the investigation of atomic distributions within the ZnO/GDL structure. Figure 3.4 depicts the cross-sectional images including the carbon paper. The signals from F atoms are originated from PTFE polymer on MPL layer. The Zn and O atoms are mainly localized on the nanostructured array above the MPL layer, implying the chemical composition of nanorod as ZnO.

In order to identify the crystalline structure of prepared Zn nanorods, the XRD patterns of ZnO/GDL and Zn foil were collected, which are depicted on Figure 3.5. The peak position profile of ZnO/GDL matches well with the zincite profile (JCPDS #36-1451). Interestingly, the exceptionally large (002) intensity on  $2\theta = 34.4^\circ$  was obtained, which indicates the vertically aligned character of ZnO arose from the nanorod morphology. [23] Meanwhile, only the Zn-based signals were found on XRD spectrum of Zn foil. (JCPDS #65-5973)

For the deeper understanding of chemical states of prepared ZnO nanorods, the XPS were conducted for ZnO/GDL and Zn foil. Figure 3.6 illustrates the collected spectra for Zn 2p, Zn L<sub>3</sub>M<sub>45</sub>M<sub>45</sub> Auger electron, and O 1s regions. On Figure 3.6A, the signals of two samples from Zn 2p region were displayed. The Zn 2p<sub>3/2</sub> signals locate on 1021.7 and 1021.4 eV for Zn foil and ZnO/GDL, respectively. Because of the native oxide layer grown on the surface of Zn foil along with the overlap of signals from Zn<sup>2+</sup> and Zn<sup>0</sup> signals (1022 and 1021.7 eV), the detailed deduction of Zn chemical states is almost impossible from Zn 2p signals only. [27-28] In this regard, to investigate the chemical states of Zn precisely, we acquired the XPS signals from Zn Auger LMM region. The LMM electron emission of Zn varies more with the change of chemical states of Zn, definitely more useful for the verification between the Zn and ZnO. Besides, it is more precise when we use the modified Auger parameter ( $\alpha$ ) as a descriptor. [27, 29-31]  $\alpha$  is a sum of maximum binding energy from Zn 2p region and maximum kinetic energy from Zn LMM

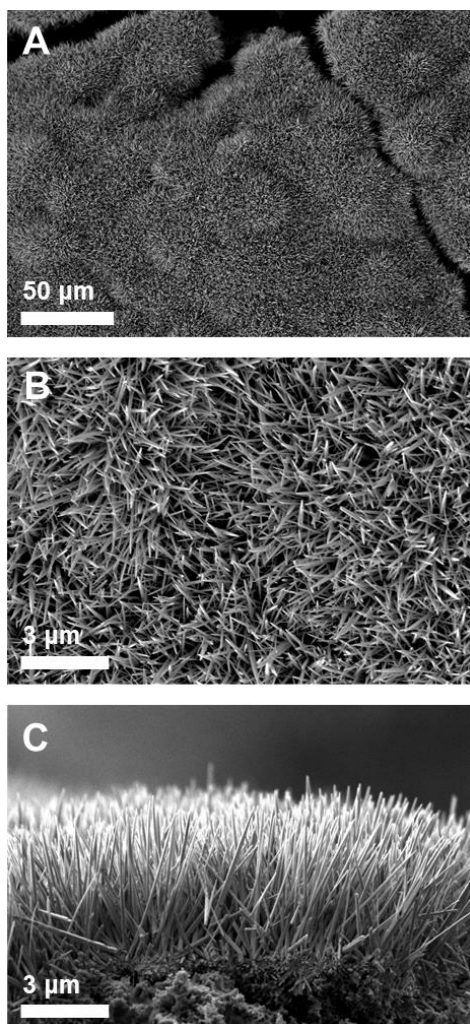


**Figure 3.3** (A-B) The top-view SEM images, and (C) cross-sectional SEM image of ZnO/GDL.

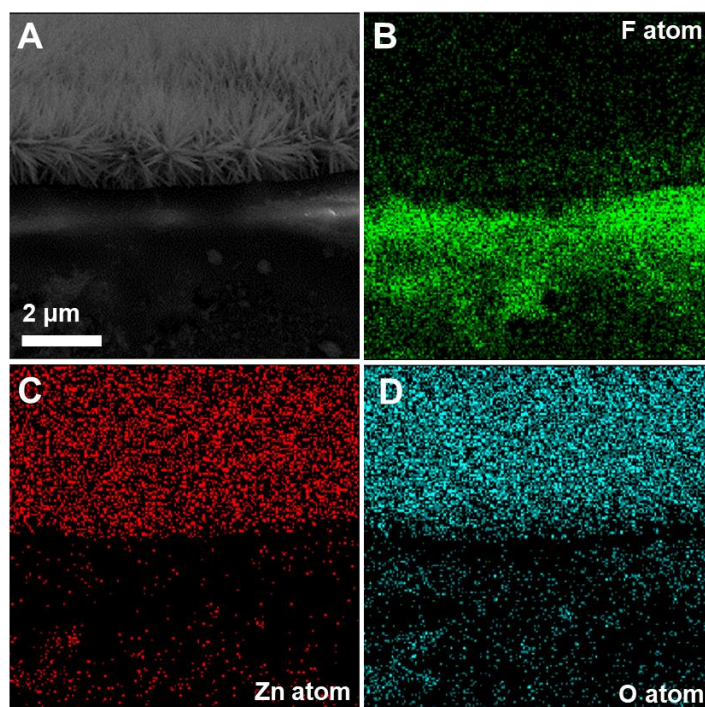


**Figure 3.4** (A) Cross-sectional SEM image of ZnO/GDL electrode. (B) F, (C) Zn, (D) O signals from EDX analysis. The F signals came from PTFE polymer located on MPL.

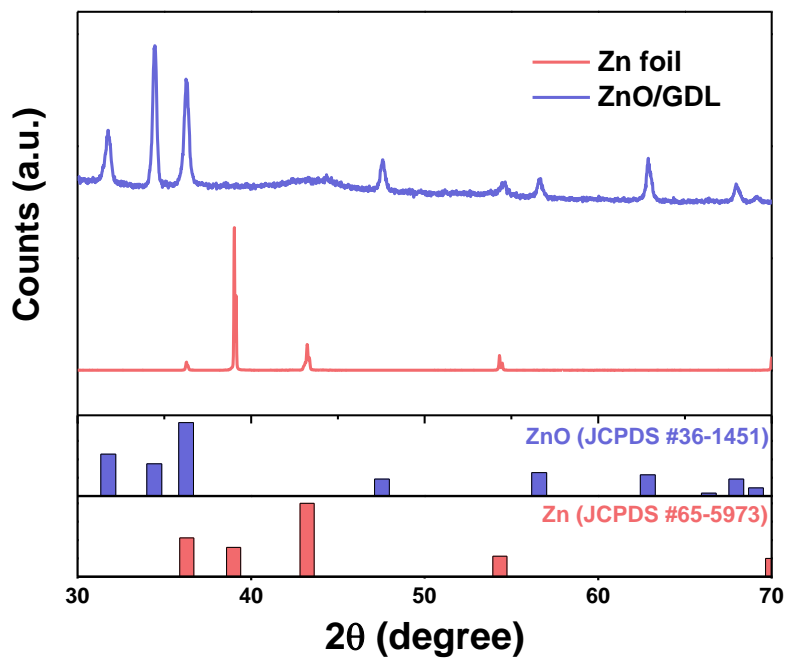


**Figure 3.5** The XRD patterns from ZnO/GDL and Zn foil. For the clarification of chemical states, the reference signals were also shown on the bottom of XRD patterns. The height of each bar indicates relative intensity of the signal on JCPDS database.

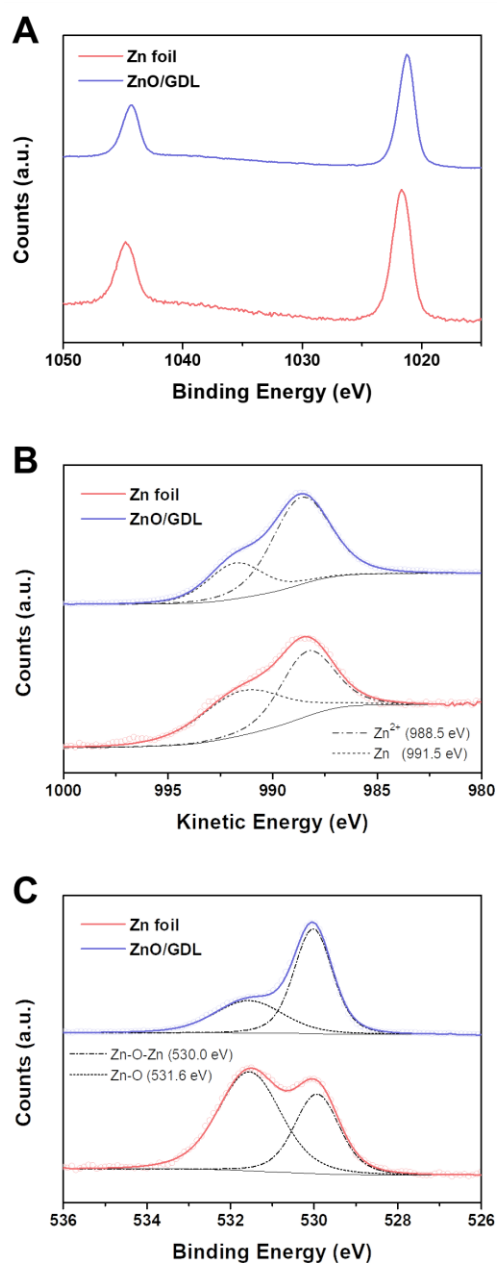


**Figure 3.6** The XPS spectra for Zn foil and ZnO/GDL using Al K $\alpha$  radiation. (A) Zn 2p spectra, (B) LMM Auger spectra and (C) O 1s spectra. The deconvolution results were depicted as dotted curves with its centers written in each graph.

region, a powerful tool for the verification of chemical state on several metals. The  $\alpha$  of ZnO/GDL and Zn foil are 2010.0 and 2010.2, respectively. Referring the Wagner plot of Zn (Figure 3.7), it could be concluded that the chemical states of both samples are in ZnO phase. Moreover, the deconvolution of Zn LMM Auger and O 1s signals were conducted. The signals from Zn LMM region could fall into two groups: lattice Zn (~988.5 eV) and interstitial Zn (~991.5 eV). [32] The signals were deconvoluted referring this data, which displayed on Figure 3.6B. The deconvolution results imply that both samples exhibit a decent size of signal assigned to lattice Zn, in accordance with the result discussed on modified Auger parameter. When we compare the detailed deconvolution results on this spectra (Table 3.1), higher Zn<sup>2+</sup> ratio for ZnO/GDL was obtained, indicating that the ZnO is much more abundant on ZnO/GDL. We suspect that the interstitial Zn might come from the Zn atoms on the surface, where the undercoordinated Zn atoms exist. On the case of Zn foil, the native oxide layer generates the Zn<sup>2+</sup> signal on Zn LMM, and its lower ratio than ZnO/GDL suggests the thin nature of this oxide layer. We found same trend on the O 1s patterns on Figure 3.6C. We found two signals on O 1s spectra, the lattice oxygen on 530 eV, and the uncoordinated oxygen on 531.6 eV. [32] The deconvolution results were summarized in Table 3.1. The results also suggest the highly crystalline character of ZnO/GDL, whereas the uncoordinated oxygen is affluent on Zn foil. In conclusion, the ZnO nanorod structure was successfully constructed on MPL-side of GDL, using seed-mediated hydrothermal growth.

### **3.3.2. Electrocatalytic reduction of CO<sub>2</sub>.**

The electrocatalytic reduction of ZnO/GDL and Zn foil was performed on homemade H-cell. The linear sweep voltammetry (LSV) results were depicted in Figure 3.8. With a broad signal near -0.65 V indicating ZnO-to-Zn reduction, the current density increases with the increase of overpotential on ZnO/GDL electrode,

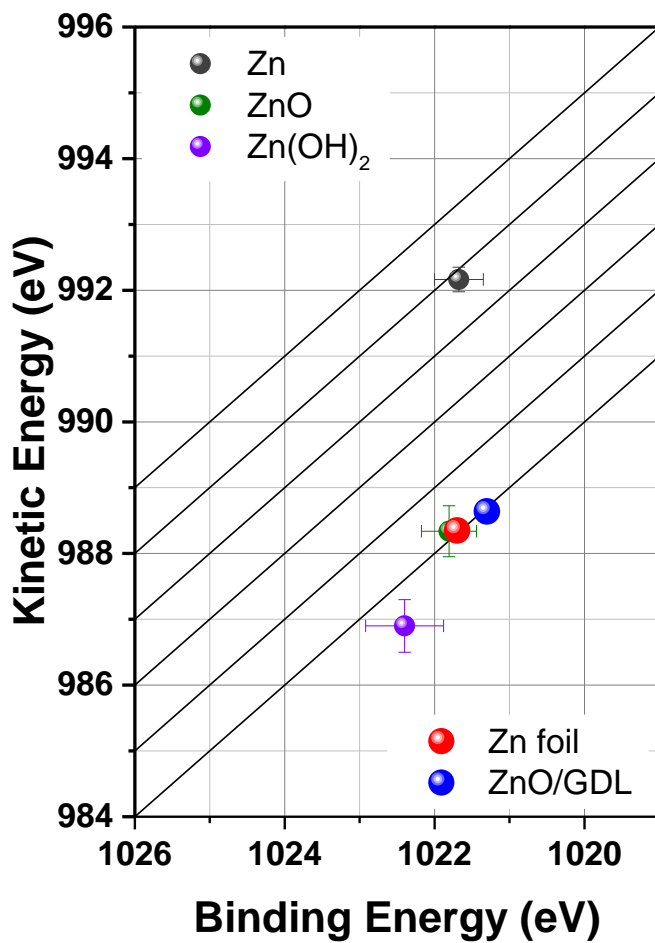


**Figure 3.7** Wagner plot of Zn. The data from NIST database were used to process the reference data. The diagonal guide lines were drawn which stand for same  $\alpha$  values. The data of Zn foil and ZnO/GDL clearly in the region of ZnO. Reproduced from Ref. [33] (NIST X-ray Photoelectron Spectroscopy Database; version 4.1, doi: 10.18434/T4T88K).

**Table 3.1** The XPS peak information of Zn foil and ZnO/GDL. The deconvolution results were described as peak position and its relative intensity in parenthesis.

		Zn foil	ZnO/GDL
Zn 2p <sub>3/2</sub> position		1021.7 eV	1021.4 eV
Zn	Lattice Zn	988.35 eV (47.88%)	988.64 eV (71.89%)
	Interstitial Zn	991.44 eV (52.12%)	991.79 eV (28.11%)
O	Zn-O-Zn	529.93 eV (36.56%)	530.02 eV (64.53%)
	Zn-O	531.55 eV (63.44%)	531.57 eV (35.47%)

finally reached to  $30 \text{ mA cm}^{-2}$  at  $-1.1 \text{ V}$ . The current density of ZnO/GDL surpasses that of Zn foil, might be ascribable to its large surface area from nanorod structure. Along with LSV polarization curves, the constant potential electrolysis for Zn foil and ZnO/GDL electrodes were conducted on  $\text{CO}_2$ -saturated  $0.5 \text{ M KHCO}_3$  electrolyte, from  $-0.6 \text{ V}$  to  $-1.1 \text{ V}$ . (Figure 3.9) Regardless of operating potentials, similar shapes of electrolysis curves were obtained: combination of a large peak on its early stage and flat profile after the disappearance of the peak. We suspect the ZnO-to-Zn reduction on early stage might be the reason of the emergence of the peak. [13] After the disappearance of the peak, the stable current density profiles were found on all the tested conditions, which proves the electrochemical stability of *in situ* prepared Zn nanoarchitecture on  $\text{CO}_2\text{RR}$  operating condition. To check the catalytic efficiency of each product, the faradaic efficiencies (FEs) were evaluated. (Figure 3.9B, D) The detailed FE values were also summarized on Table 3.2. Only  $\text{CO}$ ,  $\text{H}_2$ , formate were detected from both electrodes. On Zn foil, a gradual increase in  $\text{CO}$  selectivity with the increase of overpotential was observed till  $-1.0 \text{ V}$ , reaching maximum value of  $49.02\%$ . The decent amount of formate was also observed, while the dramatic increase of formate production about  $53.86\%$  was detected at  $-1.1 \text{ V}$ . For ZnO/GDL electrode, (Figure 3.9D) much increased  $\text{CO}$  selectivity compared to Zn foil was observed, by effectively suppressing the generation of other products. It is worthy to note that the total FEs of each electrolysis was limited to  $80\text{-}90\%$  on all experiments. Especially, even below  $50\%$  of total FEs was detected on both electrodes at  $-0.6 \text{ V}$ . We suspect a decent amount of remaining ZnO could be the reason. The slow reduction of remaining ZnO constantly occurs along the electrolysis, occupying a small portion of FE in an undetectable form. These FEs were also summarized in Figure 3.10, to easily compare FEs between Zn foil and ZnO/GDL electrodes. Superior  $\text{CO}$  selectivity of ZnO/GDL was obtained on all measured potentials. The  $\text{CO}$  selectivity from

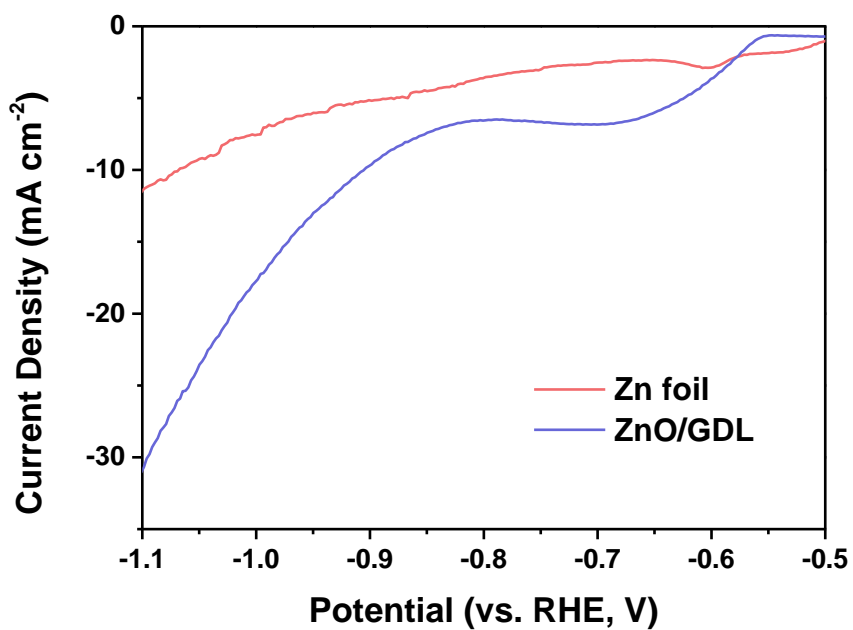


**Figure 3.8** The linear-sweep voltammogram profiles of Zn foil and ZnO/GDL, on CO<sub>2</sub>-saturated 0.5 M KHCO<sub>3</sub> electrolyte.

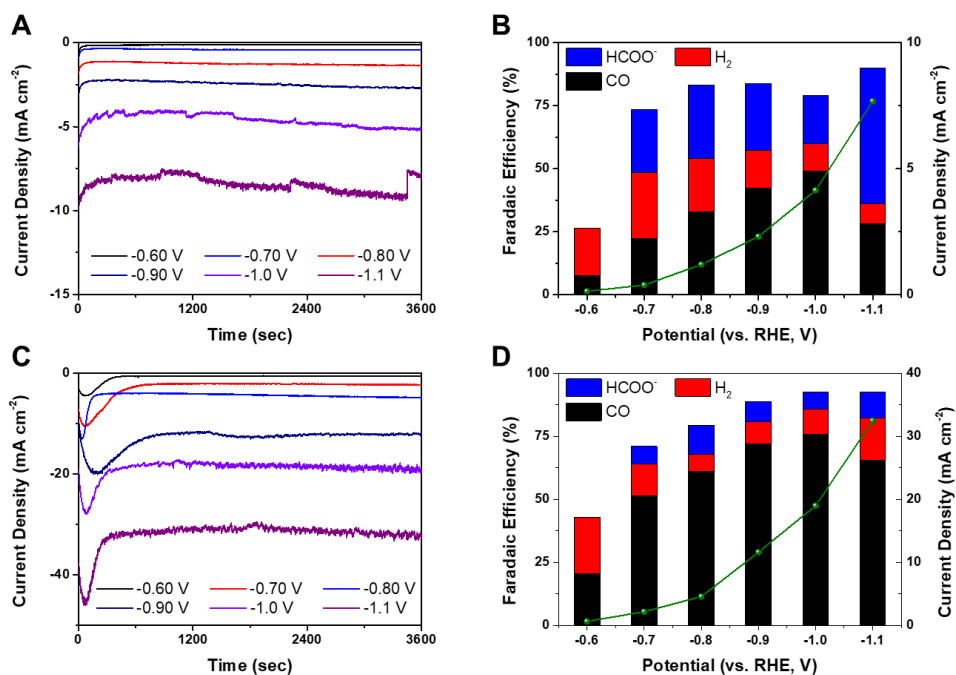


**Figure 3.9** The i-t characteristics and product distribution results from -0.6 to -1.1 V, for (A-B) Zn foil and (C-D) ZnO/GDL electrodes.

**Table 3.2** The detailed faradaic efficiencies measured on designated potentials and samples. The formate was not observed on the electrolysis at -0.6 V.

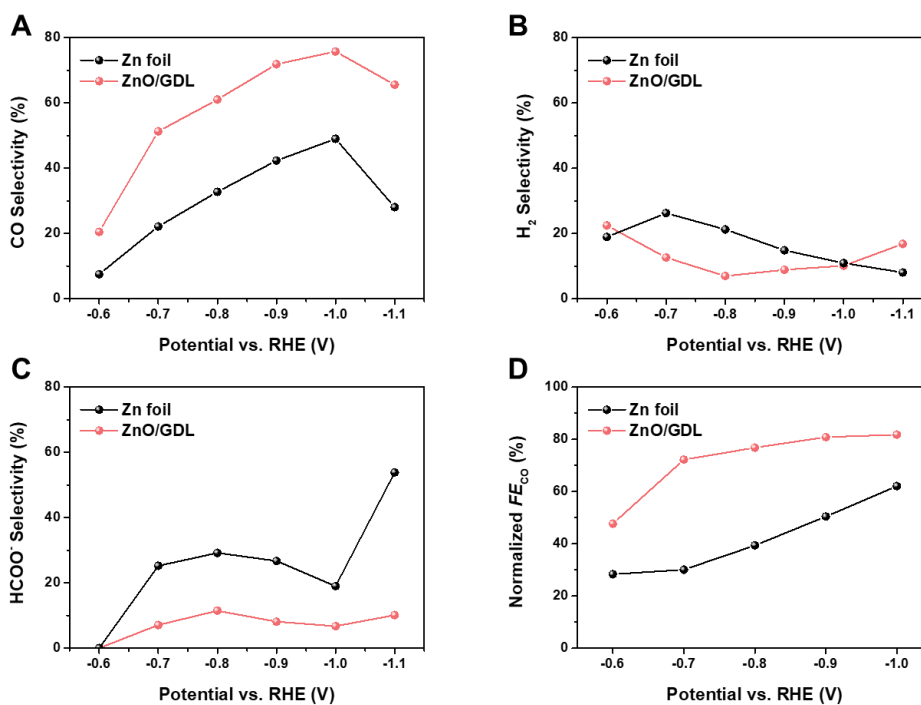
	<b>Zn foil</b>			<b>ZnO/GDL</b>		
	CO	H <sub>2</sub>	Formate	CO	H <sub>2</sub>	Formate
<b>-0.6 V</b>	7.5	18.95	-	20.5	22.47	-
<b>-0.7 V</b>	22.14	26.25	25.24	51.32	12.62	7.09
<b>-0.8 V</b>	32.76	21.25	29.21	61.05	6.94	11.46
<b>-0.9 V</b>	42.34	14.84	26.74	71.9	8.87	8.13
<b>-1.0 V</b>	49.02	10.92	19.0	75.79	10.11	6.73
<b>-1.1 V</b>	28.06	8.02	53.86	65.6	16.80	10.13

ZnO/GDL reaches its maximum point of 75.8% on -1.0 V. Formate and H<sub>2</sub> also generated as byproducts, occupying small portions on each electrolysis. Compared to ZnO, Zn foil generated more H<sub>2</sub>. Additionally, for the evaluation of the portion of CO production solely from CO<sub>2</sub>RR, we calculated the CO selectivity confined only for detected products. (Refer equation (1)) The result was depicted on Figure 3.10D. The normalized CO FEs depicts a much flattened profile compared to original CO FEs, even surpassing 80% on -0.9 V and -1.0 V. From the results, we could conclude that the prepared Zn nanoarchitecture has an improved CO<sub>2</sub>-to-CO catalyzation ability than bulk Zn foil.

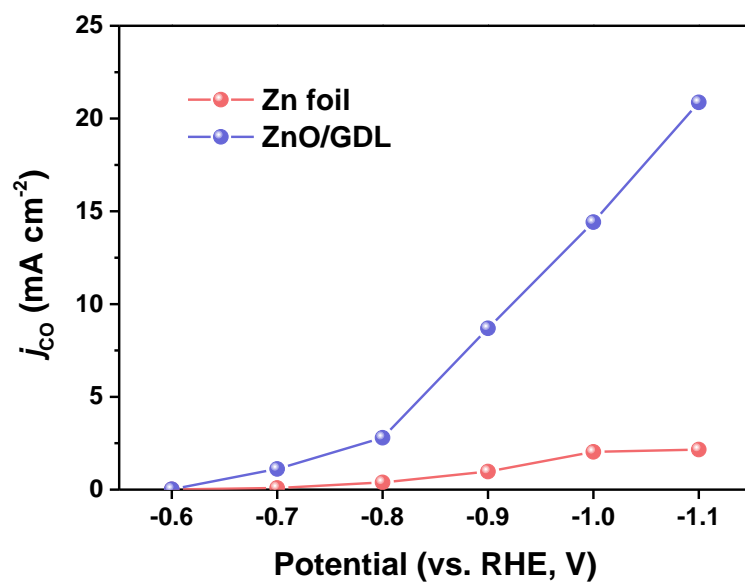
In order to quantitatively understand the CO-production rate, the partial current of CO was calculated. ( $j_{CO}$ , Figure 3.11) The ZnO/GDL exhibited a high partial current density of 20.87 mA cm<sup>-2</sup> on -1.10 V, about 10 times higher than Zn foil on same potential. This value corresponds to a production rate of 389 μmol cm<sup>-2</sup> h<sup>-1</sup>, comparable to the reported Zn-based catalysts. (Figure 3.12) As a consequence, these CO<sub>2</sub>RR performances of our ZnO/GDL electrode clearly demonstrates that our electrode preparation method is a highly efficient and robust method for the preparation of Zn-based CO<sub>2</sub>RR electrodes with high activities and selectivities.

### 3.3.3. Elucidating the origin of superior performance of ZnO/GDL

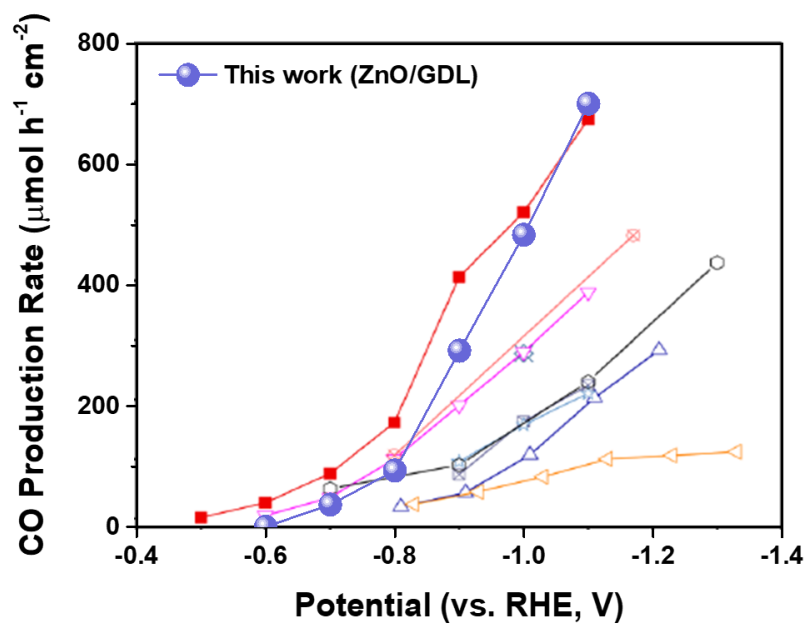
From previous chapter, we found the improved CO<sub>2</sub>RR performance on ZnO/GDL structure, ascribable to the synthesized ZnO nanorod architecture. In order to understand the structural and chemical changes upon CO<sub>2</sub>RR, we carried out several analyses on post-CO<sub>2</sub>RR ZnO/GDL electrode. Figure 3.13 illustrates the XRD spectra obtained from pristine and post-CO<sub>2</sub>RR ZnO/GDL electrodes. From the XRD pattern on Figure 3.13, the chemical composition was undoubtedly changed toward metallic Zn. Intriguingly, the XRD pattern of post-CO<sub>2</sub>RR ZnO/GDL was different with the pattern of Zn foil. (see Figure 3.5) The enlarged signal of (101) and (200) facet implies that the crystallographic morphology of the



**Figure 3.10** The product distributions for (A) CO, (B) hydrogen, and (C) formate on Zn foil and ZnO/GDL electrodes from -0.6 to -1.1 V. (D) The normalized FE of CO for the prepared samples. Refer equation (1) for the calculation method.



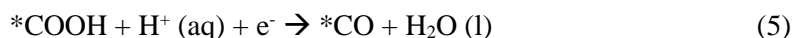
**Figure 3.11** The partial current density of CO ( $j_{CO}$ ) of prepared electrodes.



**Figure 3.12** Comparison of our catalysts with current density profiles from reported Zn-based catalysts. Blue dotted line graph shows our results. Reproduced from Ref. [7] (*ACS Catal.* **2019**, *9*, 3783-3791).

prepared Zn architecture was much differentiated structure from its foil counterpart. A small ZnO peak near 32° was also observed, indicating the native oxide layer prepared onto the Zn nanoarchitecture through the interaction with oxygen in the air. Moreover, the SEM images were taken for post-CO<sub>2</sub>RR ZnO/GDL electrode. (Figure 3.14) The foam-like nano-architecture was prepared by CO<sub>2</sub>RR, which could be described such as tangled structures composed of string-like Zn nanowires. Comparing the two images on Figure 3.14, it is apparent that the destruction of whole structure, caused by the *in situ* reduction of ZnO. It is also worthy to note that the development of oxide-derived Zn nanoarchitecture spans for the whole Zn structure in a congruent manner, proving the consistency of this preparation method. Meanwhile, the Zn foil retained its flat morphology after the CO<sub>2</sub>RR on the same condition. (Figure 3.15) So, we found that almost complete ZnO-to-Zn reduction happens on CO<sub>2</sub>RR operating condition, and it is the main reason of the construction of highly entangled Zn nanoarchitecture. And also, as the Zn foil did not generate any nanostructure with the reduction of native oxide layer, the synthesized ZnO nanorod layer actually contributed for the construction of nanoarchitecture.

In order to elucidate the origin of the improved CO production on ZnO/GDL electrode, the electrokinetic studies including Tafel slope were conducted. From the DFT-including computer calculations for CO<sub>2</sub>RR mechanistic, the elemental steps to produce CO from CO<sub>2</sub> could be described like below: [34-35]



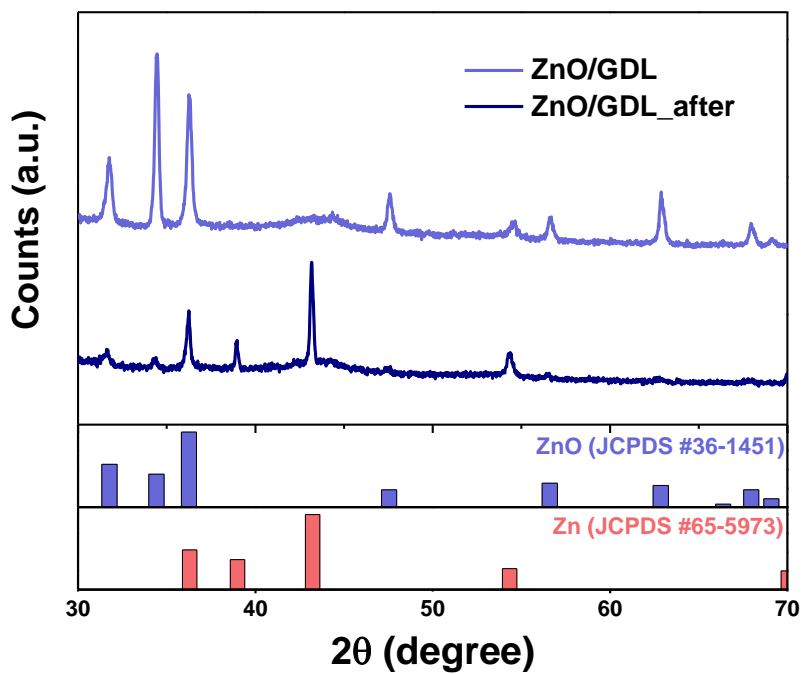


**Figure 3.13** The XRD patterns of ZnO/GDL before and after CO<sub>2</sub>RR. The XRD pattern of post-CO<sub>2</sub>RR ZnO/GDL sample is composed of Zn-based signals, which is much different with Zn foil pattern on **Figure 3.5**.

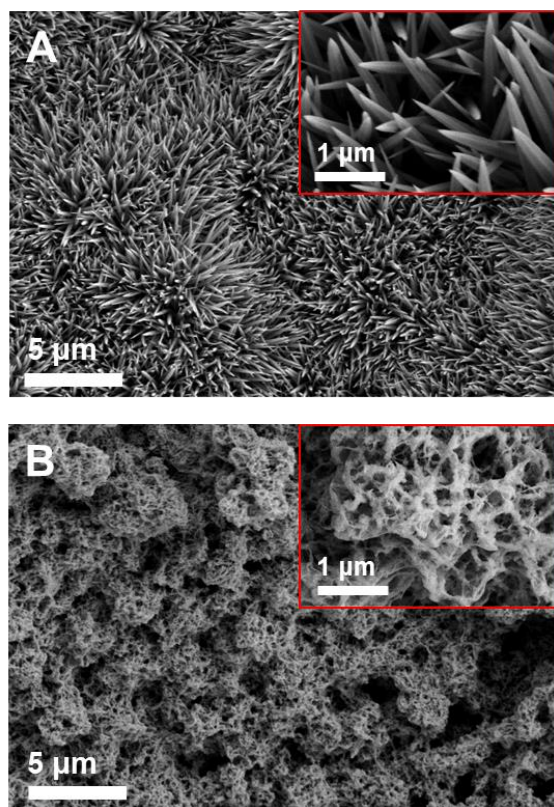


**Figure 3.14** SEM images taken from (A) pristine ZnO/GDL and (B) after the 1-h electrolysis of CO<sub>2</sub>RR. SEM images with high-magnification also suggested on top-right sides of each SEM figure.

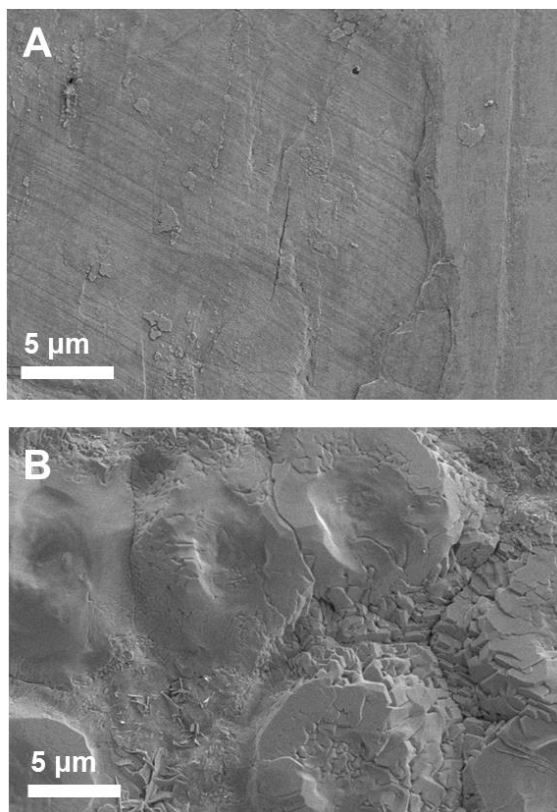


**Figure 3.15** SEM images from (A) pristine Zn foil and (B) Zn foil after the 1-hour electrolysis.

where asterisk (\*) stands for the adsorption site on Zn surfaces. The first step of a set of elemental reactions (eq 3)–including 1 electron transfer for CO<sub>2</sub> activation–is commonly considered as the RDS of this set of reactions, since it involves the breakage of the enormously stable C=O double bonds in CO<sub>2</sub> molecule. [35] To investigate the electrokinetic data of our catalysts, a plot of overpotential was drawn against logarithms of  $j_{CO}$  (Tafel plot,  $\eta$  vs.  $\log j_{CO}$ ) The Tafel plot was illustrated on Figure 3.16A, utilizing the  $j_{CO}$  data obtained from Figure 3.11. Please note that the Zn foil data were intentionally shifted 0.3 V upward, for the clear understandings of the data. From the low current density region where electrokinetic dominates, the Tafel slope was obtained as described in the Tafel plot. The Tafel slope of the two catalysts were quite different, slopes of 60.1 and 107.8 mV dec<sup>-1</sup> was calculated on ZnO/GDL and Zn foil electrodes, respectively. Theoretically, when the electrochemical reaction is purely controlled by electrokinetic aspects, the Tafel slope describes the electron transfer number on its RDS. [36] A Tafel slope of 59 or 118 mV dec<sup>-1</sup> indicates that the RDS contains with a 0 or 1-electron transfer, which could be describe alternatively as proton transfer (PT) or electron transfer (ET) step, respectively. Substitution of these values onto evaluated Tafel slope of our electrodes, interestingly, ZnO/GDL and Zn foil undergo different RDS for the production of CO: a PT RDS (eq 4) on ZnO/GDL and ET RDS (eq 3) on Zn foil. This result is quite remarkable, as the shift of RDS means that the catalyst could overcome high energy barrier on ET step (eq 3), by stabilizing the \*CO<sub>2</sub><sup>-</sup> intermediate efficiently. [12] However, it should be pointed out that the RDS of a certain Zn-based catalysts are severely influenced by non-electrokinetic aspects, such as surface oxidation state, crystal structure, or porosity of the catalyst layer. [34-35, 37] In this regard, the reaction order of each sample with respect to HCO<sub>3</sub><sup>-</sup> was evaluated. The constant potential electrolysis on -0.7 V was evaluated on Zn foil and ZnO/GDL electrodes by controlling [HCO<sub>3</sub><sup>-</sup>] from 0.1 to 0.5 M. (Figure 3.16B) The potential of -0.7 V was taken to minimize the

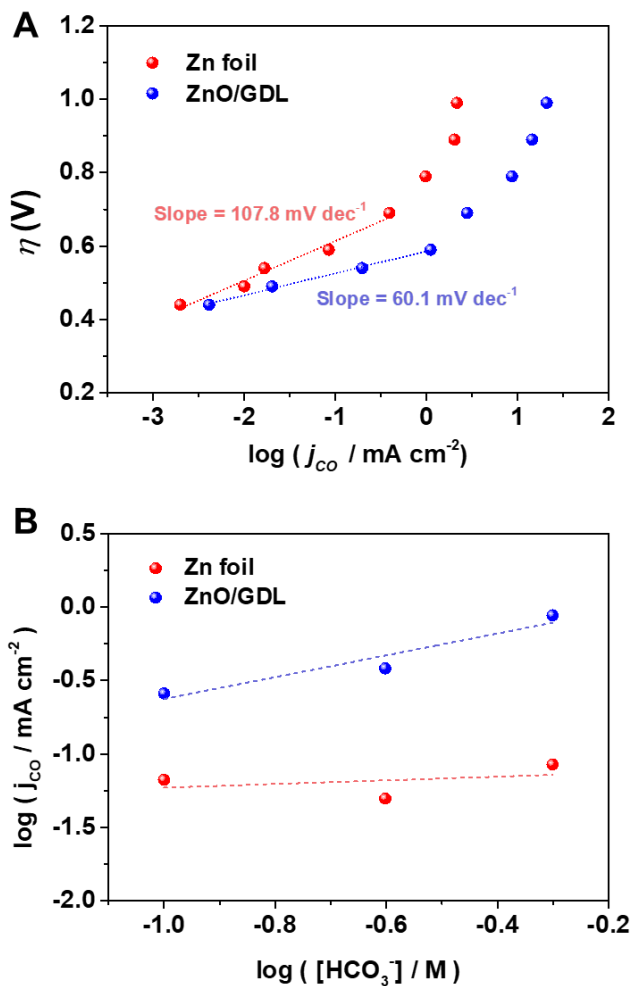


**Figure 3.16** The electrokinetic studies of CO<sub>2</sub> reduction to CO on oxide-derived Zn from ZnO/GDL electrode and Zn foil. (A) Tafel plot and the evaluated Tafel slope on the linear region. The overpotential ( $\eta$ ) value of Zn foil is pointed 0.3 V upward, to separate results from two electrodes. (B) Verification of [HCO<sub>3</sub><sup>-</sup>] dependency of each electrode. The slope of 0.74 and 0.12 was obtained for each linear fitting.

non-electrokinetic influences. To maintain the ionic strength, KCl was added to compensate  $\text{KHCO}_3$  amount. Interestingly, the ZnO/GDL and Zn foil exhibited different dependence on  $[\text{HCO}_3^-]$ , slope about 0.74 and 0.12 was observed on each electrode. It is commonly accepted that the  $\text{HCO}_3^-$  could serve as a proton donor on PT step (eq 4). [12, 38] So, the 0.74<sup>th</sup> order of dependency does not perfectly match with this idea, but much difference values obtained between two electrodes obviously verifies that two Zn-based electrodes work in different mechanisms. Hence, combining the electrokinetic analysis results altogether, we found the improved  $\text{CO}_2\text{RR}$  kinetics on ZnO/GDL electrode compared to Zn foil, and the change of RDS is a major reason for it. As many oxide-derived catalysts insists, the *in situ* generated reactive surfaces or interfaces from nanostructured oxides might be the key feature on our Zn nanoarchitecture.

#### **3.3.4. Application toward flow-cell architecture of ZnO/GDL electrode**

The electrocatalytic experiments operated on H-cell were done for prepared samples until this part. This method fits well for the evaluation of the catalytic performance, as its three-electrode configuration fits perfectly for the assessment of the catalytic activity. However, when we move our focus on its practical application, the operation on H-cell configuration is not sufficient, because of its definitely low production rate. In this manner, the evaluation of the catalyst on flow cell architecture directly manipulating gaseous type  $\text{CO}_2$  should also be done, for the future of the  $\text{CO}_2\text{RR}$  on our society.

We constructed MEA-based flow cell architecture (refer Figure 3.2), comprised of anodic and cathodic flow fields and separating anion exchange membrane. The 1 M KOH was used for the anodic electrolyte, which proves to exhibit much better performance than neutral counterpart. [39] Also, for the efficient transport of  $\text{OH}^-$  ion between two compartments, the Sustainion<sup>®</sup> membrane, composed of alkaline-stable polystyrene backbone with a hydronium ion conducting imidazolium

moieties. [40-41] (Figure 3.17) For the operation of flow-cell, the cathode must satisfy many prerequisites. It requires the CO<sub>2</sub>-flow through its structure accompanied by the suppression of liquid flow beneath the catalyst layer. Fortunately, our ZnO/GDL fulfills these requirements, since it uses the GDL as a substrate with a hydrophobic PTFE-coated MPL layer beneath the ZnO array. Therefore, the samples employed on H-cell test could directly be tested on our MEA-based flow cell. We conducted CO<sub>2</sub>RR electrolysis from aforementioned materials, as depicted in Figure 3.18. The cyclic voltammetry (CV) was recorded to 3.0 V of cell voltage, exhibiting ~200 mA cm<sup>-2</sup> on 3.0 V, an economically viable performance. Moreover, a constant-potential electrolysis was done on 2.7 V, to check the durability of the Zn electrode on 1 M KOH, an extremely basic environment. The 2-hour long electrolysis result was depicted on Figure 3.18B. Faradaic efficiencies of CO were maintained above 75% on 2-hour-long electrolysis. Although a noticeable degradation on current density was found on the electrolysis, it is worthy to note that the degradation was not severe on its last 60 minutes (81.8 to 73.0 mA cm<sup>-2</sup>, 89% retention). These results demonstrate the potential of our ZnO/GDL electrode, for the practical application of Zn-based materials on the large-scale electrosynthesis of CO.

### 3.4. Conclusion

In this study, the ZnO nanorods array was synthesized using hydrothermal synthesis. The deliberate reduction of ZnO to Zn on operating condition constructed Zn nanoarchitecture completely different from Zn foil structure. This nanostructured Zn electrode exhibited much improved electrocatalytic performance on CO<sub>2</sub>-to-CO conversion, compared to its foil counterpart. The post-electrolysis analysis combined with electrokinetic studies verified that the improved kinetics on CO<sub>2</sub>RR of ZnO/GDL electrode, which might be deduced from the generated nanostructure. Also, attributed to its well-fitted properties for flow-cell application,

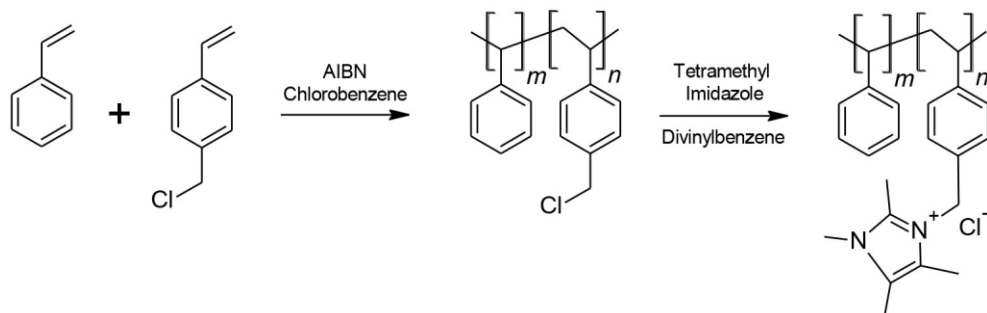


**Figure 3.17** Synthetic route and the chemical structure of Sustainion<sup>®</sup> anion exchange membrane. Adapted from Ref. [40] (*Front. Chem.* **2018**, *6*, 263.)

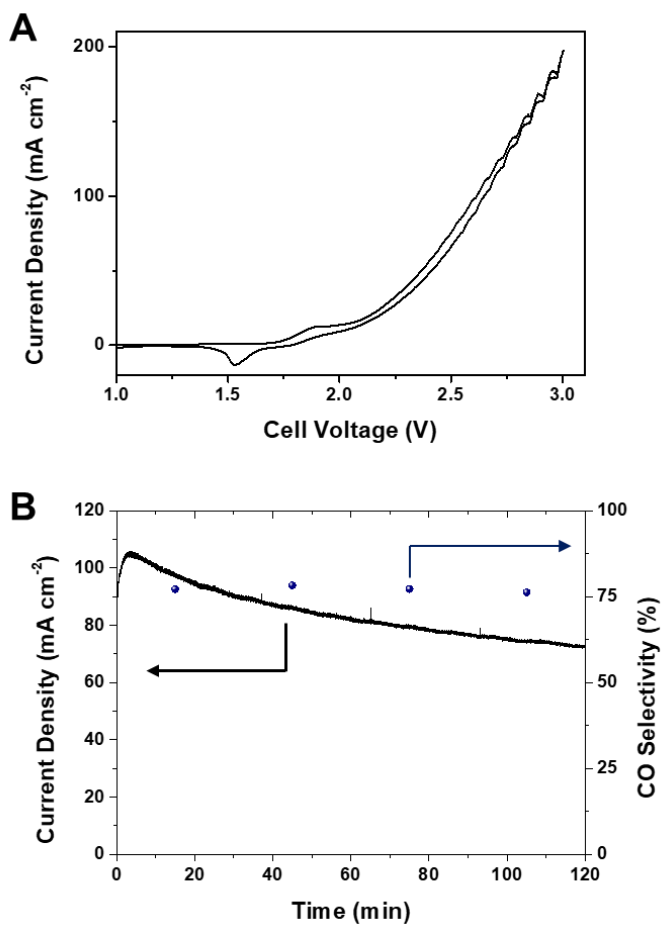


**Figure 3.18** The electrocatalytic performance of ZnO/GDL electrode on flow-cell operation. (A) Cyclic voltammogram curve recorded on stabilized current density profiles. (B) 2-hour long electrolysis data. The CO selectivities were evaluated on every 30 minutes.

the flow-cell operation on MEA-based architecture was evaluated for ZnO/GDL electrode, which exhibited over 200 mA cm<sup>-2</sup> on 3.0 V. The 2-hour long electrolysis also proves that the decent stability of ZnO/GDL electrode on its operating conditions. Given the catalytic performance of the ZnO/GDL and its great possibility on flow-cell operation, we hope that our synthetic strategy guides a route for the practical application of large-scale electrosynthesis of CO.

### 3.5. References

- [1] Hori, Y. *Modern Aspects of Electrochemistry*, Springer, New York, NY, **2008**.
- [2] Cao, Z.; Kim, D.; Hong, D.; Yu, Y.; Xu, J.; Lin, S.; Wen, X.; Nichols, E. M.; Jeong, K.; Reimer, J. A.; Yang, P.; Chang, C. J. A molecular surface functionalization approach to tuning nanoparticle electrocatalysts for carbon dioxide reduction. *J. Am. Chem. Soc.* **2016**, *138*, 8120-8125.
- [3] Kim, C.; Jeon, H. S.; Eom, T.; Jee, M. S.; Kim, H.; Friend, C. M.; Min, B. K.; Hwang, Y. J. Achieving selective and efficient electrocatalytic activity for CO<sub>2</sub> reduction using immobilized silver nanoparticles. *J. Am. Chem. Soc.* **2015**, *137*, 13844-13850.
- [4] Zheng, T.; Jiang, K.; Wang, H. Recent advances in electrochemical CO<sub>2</sub>-to-CO conversion on heterogeneous catalysts. *Adv. Mater.* **2018**, *30*, 1802066.
- [5] Won, D. H.; Shin, H.; Koh, J.; Chung, J.; Lee, H. S.; Kim, H.; Woo, S. I. Highly efficient, selective, and stable CO<sub>2</sub> electroreduction on a hexagonal Zn catalyst. *Angew. Chem. Int. Ed.* **2016**, *55*, 9297-9300.
- [6] Rosen, J.; Hutchings, G. S.; Lu, Q.; Forest, R. V.; Moore, A.; Jiao, F. Electrodeposited Zn dendrites with enhanced CO selectivity for electrocatalytic CO<sub>2</sub> reduction. *ACS Catal.* **2015**, *5*, 4586-4591.
- [7] Luo, W.; Zhang, J.; Li, M.; Züttel, A. Boosting CO production in electrocatalytic CO<sub>2</sub> reduction on highly porous Zn catalyst. *ACS Catal.* **2019**, *9*, 3783-3791.
- [8] Low, Q. H.; Loo, N. W. X.; Calle-Vallejo, F.; Yeo, B. S. Enhanced electroreduction of carbon dioxide to methanol using zinc dendrites pulse-deposited on silver foam. *Angew. Chem. Int. Ed.* **2019**, *58*, 2256-2260.
- [9] Lu, Y.; Han, B.; Tian, C.; Wu, J.; Geng, D.; Wang, D. Efficient electrocatalytic reduction of CO<sub>2</sub> to CO on an electrodeposited Zn porous network. *Electrochem. Commun.* **2018**, *97*, 87-90.
- [10] Quan, F.; Zhong, D.; Song, H.; Jia, F.; Zhang, L.; A highly efficient zinc catalyst for selective electroreduction of carbon dioxide in aqueous NaCl solution. *J. Mater. Chem. A* **2015**, *3*, 16409-16413.
- [11] Li, C. W.; Kanan, M. W. CO<sub>2</sub> reduction at low overpotential on Cu electrodes

resulting from the reduction of thick Cu<sub>2</sub>O films. *J. Am. Chem. Soc.* **2012**, *134*, 7231-7234.

[12] Li, C. W.; Ciston, J.; Kanan, M. W. Electroreduction of carbon monoxide to liquid fuel on oxide-derived nanocrystalline copper. *Nature* **2014**, *508*, 504-507.

[13] Liu, K.; Wang, J.; Shi, M.; Yan, J.; Jiang, Q. Simultaneous achieving of high faradaic efficiency and CO partial current density for CO<sub>2</sub> reduction via robust, noble-metal-free Zn nanosheets with favorable adsorption energy. *Adv. Energy Mater.* **2019**, *9*, 1900276.

[14] Jiang, K.; Wang, H.; Cai, W.-B.; Wang, H. Li electrochemical tuning of metal oxide for highly selective CO<sub>2</sub> reduction. *ACS Nano* **2017**, *11*, 6451-6458.

[15] Hatsukade, T.; Kuhl, K. P.; Cave, E. R.; Abram, D. N.; Feaster, J. T.; Jongsomjit, A. L.; Hahn, C.; Jaramillo, T. F. Carbon dioxide electroreduction using a silver-zinc alloy. *Energy Technol.* **2017**, *5*, 955-961.

[16] Lamaison, S.; Wakerley, D.; Blanchard, J.; Montero, D.; Rouse, G.; Mercier, D.; Marcus, P.; Taverna, D.; Giaume, D.; Mougél, V.; Fontecave, M. High-current-density CO<sub>2</sub>-to-CO electroreduction on Ag-alloyed Zn dendrites at elevated pressure. *Joule* **2020**, *4*, 1-12.

[17] Zhang, T.; Qiu, Y.; Yao, P.; Li, X.; Zhang, H. Bi-modified Zn catalyst for efficient CO<sub>2</sub> electrochemical reduction to formate. *ACS Sustainable Chem. Eng.* **2019**, *7*, 15190-15196.

[18] Ajmal, S.; Yang, Y.; Li, K.; Tahir, M. A.; Liu, Y.; Wang, T.; Bacha, A.-U.-R.; Feng, Y.; Deng, Y.; Zhang, L. Zinc-modified copper catalyst for efficient (photo)electrochemical CO<sub>2</sub> reduction with high selectivity of HCOOH production. *J. Phys. Chem. C* **2019**, *123*, 11555-11563.

[19] Ma, Z.; Wu, D.; Han, X.; Wang, H.; Zhang, L.; Gao, Z.; Xu, F.; Jiang, K. Ultrasonic assisted synthesis of Zn-Ni bi-metal MOFs for interconnected Ni-N-C materials with enhanced electrochemical reduction of CO<sub>2</sub>. *J. CO<sub>2</sub> Util.* **2019**, *32*, 251-258.

[20] Yang, F.; Song, P.; Liu, X.; Mei, B.; Xing, W.; Jiang, Z.; Gu, L.; Xu, W. Highly efficient CO<sub>2</sub> electroreduction on ZnN<sub>4</sub>-based single-atom catalyst. *Angew. Chem. Int. Ed.* **2018**, *57*, 12303-12307.

[21] Zhao, M.; Tang, H.; Yang, Q.; Gu, Y.; Zhu, H.; Yan, S.; Zou, Z. Inhibiting hydrogen evolution using a chloride adlayer for efficient electrochemical CO<sub>2</sub> reduction on Zn electrodes. *ACS Appl. Mater. Interfaces* **2020**, *12*, 4565-4571.

[22] Tian, J.-H.; Hu, J.; Li, S.-S.; Zhang, F.; Liu, J.; Shi, J.; Li, X.; Tian, Z.-Q.; Chen, Y. Improved seedless hydrothermal synthesis of dense and ultralong ZnO nanowires. *Nanotechnol.* **2011**, *22*, 245601.

[23] Hu, J.; Sun, Y.; Zhang, W.; Gao, F.; Li, P.; Jiang, D.; Chen, Y. Fabrication of hierarchical structures with ZnO nanowires on micropillars by UV soft imprinting and hydrothermal growth for a controlled morphology and wettability. *App. Surf. Sci.* **2014**, *317*, 545-551.

[24] Hong, S.-H.; Kim, M.-H.; Yun, H.-W.; Paik, T.; Lee, H. Solution-processed fabrication of superhydrophobic hierarchical zinc oxide nanostructures via nanotransfer printing and hydrothermal growth. *Surf. Coat. Technol.* **2017**, *331*, 189-195.

[25] Nwabara, U. O.; Cofell, E. R.; Verma, S.; Negro, E.; Kenis, P. J. A. Durable cathodes and electrolyzers for the efficient aqueous electrochemical reduction of CO<sub>2</sub>. *ChemSusChem* **2020**, *13*, 855-985.

[26] Jeong, H.-Y.; Balamurugan, M.; Choutipalli, V. S. K.; Jeong, E.-S.; Subramanian, V.; Sim, U.; Nam, K. T. Achieving highly efficient CO<sub>2</sub> to CO electroreduction exceeding 300 mA cm<sup>-2</sup> with single-atom nickel electrocatalysts. *J. Mater. Chem. A* **2019**, *7*, 10651-10661.

[27] Moulder, J. F.; Stickle, W. F.; Sobol, P. E.; Bomben, K. D. *Handbook of X-ray photoelectron spectroscopy*, Perkin-Elmer Corp., Physical Electronic Division, 2<sup>nd</sup> Ed, **1992**.

[28] Barreca, D.; Gasparotto, A.; Maccato, C.; Maragno, C.; Tondello, E. ZnO nanoplatelets obtained by chemical vapor deposition, studied by XPS. *Surf. Sci. Spectra* **2007**, *14*, 19-22.

[29] Biesinger, M. C.; Lau, L. W. M.; Gerson, A. R.; Smart, R. St. C. Resolving surface chemical states in XPS analysis of first row transition metals, oxides and hydroxides: Sc, Ti, V, Cu and Zn. *Appl. Surf. Sci.* **2010**, *257*, 887-898.

[30] Chandriahgari, C. R.; Bellis, G. D.; Ballirano, P.; Baljepalli, S. K.; Kaciulis, S.; Caneve, L.; Sarto, F.; Sarto, M. S. Synthesis and characterization of ZnO nanorods with a narrow size distribution. *RSC Adv.* **2015**, *5*, 49861-49870.

- [31] Wagner, C. D. Auger lines in X-ray photoelectron spectroscopy. *Anal. Chem.* **1972**, *44*, 967-973.
- [32] Li, W.; Fang, L.; Qin, G.; Ruan, H.; Zhang, H.; Kong, C.; Ye, L.; Zhang, P.; Wu, F. Tunable zinc interstitial related defects in ZnMgO and ZnCdO films. *J. Appl. Phys.* **2015**, *117*, 145301.
- [33] Naumkin, A. V.; Kraut-Vass, A.; Gaarenstroom, S. W.; Powell, C. J. *NIST X-ray photoelectron spectroscopy database*, **2012**.
- [34] Rosen, J.; Hutchings, G. S.; Lu, Q.; Rivera, S.; Zhou, Y.; Vlachos, D. G.; Jiao, F. Mechanistic insights into the electrochemical reduction of CO<sub>2</sub> to CO on nanostructured Ag surfaces. *ACS Catal.* **2015**, *5*, 4293-4299.
- [35] Ma, M.; Trzeniewski, B. J.; Xie, J.; Smith, W. A. Selective and efficient reduction of carbon dioxide to carbon monoxide on oxide-derived nanostructured silver electrocatalysts. *Angew. Chem. Int. Ed.* **2016**, *55*, 9748-9752.
- [36] Shinagawa, T.; Garcia-Esparza, A. T.; Takanabe, K. Insight on Tafel slopes from a microkinetic analysis of aqueous electrocatalysis for energy conversion. *Sci. Rep.* **2015**, *5*, 13801.
- [37] Singh, M. R.; Goodpaster, J. D.; Weber, A. Z.; Head-Gordon, M.; Bell, A. T. Mechanistic insights into electrochemical reduction of CO<sub>2</sub> over Ag using density functional theory and transport models. *Proc. Natl. Acad. Sci. U. S. A.* **2017**, *114*, E8812-E8821.
- [38] Zhang, T.; Zhong, H.; Qui, Y.; Li, X.; Zhang, H. Zn electrode with a layer of nanoparticles for selective electroreduction of CO<sub>2</sub> to formate in aqueous solutions. *J. Mater. Chem. A* **2016**, *4*, 16670-16676.
- [39] Dinh, C.-T.; Burdyny, T.; Kibria, M. G.; Seifitokaldani, A.; Gabardo, C. M.; Arquer, F. P. G.; Kiani, A.; Edwards, J. P.; Luna, P. D.; Bushuyev, O. S.; Zou, C.; Quintero-Bermudez, R.; Pang, Y.; Sinton, D.; Sargent, E. D. CO<sub>2</sub> electroreduction to ethylene via hydroxide-mediated copper catalysis at an abrupt interface. *Science* **2018**, *360*, 783-787.
- [40] Kaczur, J. J.; Yang, H.; Liu, Z.; Sajjad, S. D.; Masel, R. I. Carbon dioxide and water electrolysis using new alkaline stable anion membranes. *Front. Chem.* **2018**, *6*, 263.

[41] Liu, Z.; Yang, H.; Kutz, R.; Masel, R. I. CO<sub>2</sub> electrolysis to CO and O<sub>2</sub> at high selectivity, stability and efficiency using sustainion membranes. *J. Electrochem. Soc.* **2018**, *165*, J3371-J3377.

## 국문초록

지구온난화와 그로 인해 야기되는 환경의 변화가 가속화되는 현 상황에서, 신재생에너지를 활용하는 친환경적 공정의 개발이 그 무엇보다 우선시 되어야 할 것이다. 이산화탄소의 감축 및 이를 활용한 화합물의 생성이 가능하다는 장점들을 기반으로 하여 전기화학적 이산화탄소 환원 반응의 실제 활용 가능성이 높게 평가되고 있는데, 태양에너지와 같은 신재생 에너지와 결합된다면, 이산화탄소 환원 반응은 수소의 역할과 동일하게, 에너지 저장 벡터로서의 역할 역시 수행할 수 있는 가능성 역시 검토하고 있다.

하지만, 현재 기술 수준에서의 에너지의 효율을 볼 때, 전기화학적 이산화탄소의 실제 활용 가능성은 거의 없다고 볼 수 있는데, 이는 산업적 관점에서 해결되지 못한 너무나 많은 단점들이 산적하고 있기 때문이다. 대표적으로, 해당 반응의 과전압이 매우 크다는 문제가 있는데, 이는 기본적으로 이산화탄소 분자의 안정성이 매우 높아 이를 깨트리는 데만 하더라도 많은 에너지가 소비되어야 하기 때문이다. 또한, 여러 생성물들이 섞여 나온다는 문제점 역시 존재하는데, 이는 추후 분리공정을 포함하여야 하기 때문에, 이를 해결한다면 전체 비용의 절감이 가능해지리라 고려된다.

이러한 측면에서, 다양한 촉매들이 연구 및 보고되었는데, 대략적으로 귀금속 (금, 은, 구리), 중금속 (주석, 비스무트 등), 전이금속 단일원자 촉매 ( $M-N_4$ :  $M =$  망간, 니켈, 철 등) 등이 가능성 있는 촉매군으로 연구되고 있다. 이러한 금속 기반의 촉매와 더불어, 금속 산화물 기반의 촉매들 또한 그 나름의 장점을 살려 다양하게 보고되고 있다. 현 상황에서 금속 산화물 기반의 촉매는 크게 2가지의 연구 주제가

대두되는데, 첫번째는 이산화탄소 환원반응의 환원 분위기를 활용, 산화물을 반응 조건에서 먼저 급속하게 환원시켜, 만들어지는 금속 형태의 높은 반응성을 활용하는 것이다. 이러한 방식은 기존 방식에 비해 반응성이 높은 활성면을 많이 만들어낸다는 점에 기반하고 있다. 두번째는, 기본적으로 산화물이 금속에 비해 더 높은 활성을 보이는 촉매군에서의 활용으로, 중금속 기반의 개미산 생성이 대표적이다. 밀도함수 이론 기반 계산을 통해 표면의 호산소성이 높을수록 해당 촉매 표면에서의 이산화탄소 흡착 반응의 활성이 높음이 제시된 후로, 주석 산화물 ( $\text{SnO}_2$ ) 기반의 촉매들의 대두된 것이 그 예라 할 수 있다. 본 학위논문에서는 해당 두 전략을 기반으로 하여, 높은 활성을 보인 금속 산화물 기반의 나노구조 촉매를 제안하고자 한다.

먼저, 뒤이을 내용의 이해를 돕기 위해 전기화학적 이산화탄소 반응의 기본적 설명과 현재 연구 방향에 대한 간략한 소개가 진행될 계획이다.

2장에서는 양극 산화법을 이용해 제작된 주석 산화물 ( $\text{SnO}_2$ ) 나노구조 전극의 효율적 개미산 생산에 대한 연구 결과를 제시하였다. 양극 산화법과 뒤이은 열처리를 통해 성공적으로 주석 산화물 나노구조를 주석 금속 표면에 합성할 수 있었으며, 해당 구조의 높은 결정성 및 넓은 표면적 역시 확인하였다. 높은 표면적과 표면의 높은 호산소성에 기반하여, 합성된 나노구조는 개미산 생성에 있어 기존 보고된 촉매들에 비견될 만큼의 성능을 나타낸다는 것을 확인하였다. 또한, 반응 중, 후의 전극에 대한 분석을 통하여, 만들어진 전극의 반응 조건 하에서 강한 환원 억제력을 가지고, 이를 통해 남아있던 주석 산화물이 높은 활성의 원인임을 제시하였다.

3장에서는 수열합성을 통해 기체투과전극 (GDL; Gas-diffusion layer) 위에 만들어진 아연 산화물 ( $\text{ZnO}$ ) 나노막대 구조의 높은 일산화탄소 생성

효율이 제시되었다. 합성된 아연 산화물 구조는 반응이 진행되는 순간부터 금속 아연으로 환원되어 금속 아연 상태의 나노구조로 변화한다. 해당 방식으로 만들어진 전극은 기존 아연 전극 대비 최대 약 75%에 달하는 높은 CO 변환 효율 및 전류값을 나타내었다. Tafel 분석 및 추가적인 전기화학 속도론 실험의 결과를 바탕으로, 만들어진 전극의 촉매적 활성이 비약적으로 증가하였음을 확인하였으며, 이는 환원되어 만들어진 금속 아연 나노구조에서 기반함을 보였다. 추가적으로, 해당 전극을 기체상태의 이산화탄소를 반응물로 직접 활용하는 플로우 셀 전극에 활용하였고, 약  $80 \text{ mA cm}^{-2}$  정도의 전류밀도와 함께, 75% 이상의 CO 생성 효율을 2시간의 전기분해 실험동안 성공적으로 유지할 수 있음을 확인하였다.

**주요어:** 이산화탄소, 전기화학, 산화물 전극, CO<sub>2</sub> 환원, SnO<sub>2</sub>, 나노구조.

**학번:** 2014-21521

## List of publications (SCI)

### 1<sup>st</sup> or co-1<sup>st</sup> author

1. **Juwon Jeong**<sup>†</sup>, Woojeong Bak<sup>†</sup>, Jung-Woo Choi, Kyung Jae Lee, Jin Soo Kang, Jin Kim, Dong Gwan Kim, Won Cheol Yoo\*, Yung-Eun Sung\*. Application of Three-Dimensionally Ordered Mesoporous TiO<sub>2</sub> Particles as Dual-Function Scatterers in Dye-Sensitized Solar Cells. *Electrochimica Acta* **2016**, 222, 1079-1085.

### Co-author

1. Jin Soo Kang<sup>†</sup>, Min-Ah Park<sup>†</sup>, Jae-Yup Kim<sup>†</sup>, Sun Ha Park, Dong Young Chung, Seung-Ho Yu, Jin Kim, Jongwoo Park, Jung-Woo Choi, Kyung Jae Lee, **Juwon Jeong**, Min Jae Ko\*, Kwang-Soon Ahn\*, Yung-Eun Sung\*, Reactively sputtered nickel nitride as electrocatalytic counter electrode for dye-and quantum dot-sensitized solar cells. *Scientific Reports* **2015**, 5, 10450.

2. Segeun Jang<sup>†</sup>, Jin Soo Kang<sup>†</sup>, Jong-Kwon Lee, Sang Moon Kim, Yoon Jun Son, Ahyoum Lim, Hyesung Cho, Jin Kim, **Juwon Jeong**, Gunhee Lee, Yung-Eun Sung\*, Mansoo Choi\*, Enhanced Light Harvesting in Mesoscopic Solar Cells by Multilevel Multiscale Patterned Photoelectrodes with Superpositioned Optical Properties. *Advanced Functional Materials* **2016**, 26, 6584-6592.

3. Jin Soo Kang<sup>†</sup>, Joohyun Lim<sup>†</sup>, Won-Yeop Rho, Jin Kim, Doo-Sik Moon, **Juwon Jeong**, Dongwook Jung, Jung-Woo Choi, Jin-Kyu Lee\*, Yung-Eun Sung\*, Wrinkled silica/titania nanoparticles with tunable interwrinkle distances for efficient utilization of photons in dye-sensitized solar cells. *Scientific Reports* **2016**, 6, 30829.

4. Jin Soo Kang<sup>†</sup>, Jin Kim<sup>†</sup>, Myeong Jae Lee<sup>†</sup>, Yoon Jun Son, **Juwon Jeong**, Dong Young Chung, Ahyoum Lim, Heeman Choe, Hyun S. Park\*, Yung-Eun Sung\*. Electrochemical synthesis of nanoporous tungsten carbide and its application as electrocatalysts for photoelectrochemical cells. *Nanoscale* **2017**, 9, 5413-5424.

5. Jin Soo Kang<sup>†</sup>, Jin Kim<sup>†</sup>, Myeong Jae Lee<sup>†</sup>, Yoon Jun Son, Dong Young Chung, Subin Park, **Juwon Jeong**, Ji Mun Yoo, Heejong Shin, Heeman Choe, Hyun S. Park\*, Yung-Eun Sung\*, Electrochemically Synthesized Nanoporous Molybdenum Carbide as a Durable Electrocatalyst for Hydrogen Evolution Reaction. *Advanced Science* **2018**, 5, 1700601

6. Jin Soo Kang<sup>†</sup>, Jae-Yup Kim<sup>†</sup>, Jungjin Yoon<sup>†</sup>, Jin Kim, Jiwoong Yang, Dong Young Chung, Min-cheol Kim, Hansol Jeong, Yoon Jun Son, Bong Gyu Kim, **Juwon Jeong**, Taeghwan Hyeon, Mansoo Choi\*, Min Jae Ko\*, Yung-Eun Sung\*, Room-Temperature Vapor Deposition of Cobalt Nitride Nanofilms for Mesoscopic and Perovskite Solar Cells. *Advanced Energy Materials* **2018**, 8, 1703114.

7. Jin Soo Kang<sup>†</sup>, Jin Kim<sup>†</sup>, Jae-Yup Kim, Myeong Jae Lee, Jiho Kang, Yoon Jun Son, **Juwon Jeong**, Sun Ha Park, Min Jae Ko\*, Yung-Eun Sung\*, Highly efficient bifacial dye-sensitized solar cells employing polymeric counter electrodes. *ACS Applied Materials & Interfaces* **2018**, *10*, 8611-8620.
8. Bo Quan<sup>†</sup>, Aihua Jin<sup>†</sup>, Seung-Ho Yu, Seok Mun Kang, **Juwon Jeong**, Hèctor D. Abruña, Longyi Jin, Yuanzhe Piao\*, Yung-Eun Sung\*, Solvothermal-Derived S-Doped Graphene as an Anode Material for Sodium-Ion Batteries. *Advanced Science* **2018**, *5*, 1700880.
9. Yoon Jun Son<sup>†</sup>, Jin Soo Kang<sup>†</sup>, Jungjin Yoon, Jin Kim, **Juwon Jeong**, Jiho Kang, Myeong Jae Lee, Hyun S. Park\*, Yung-Eun Sung\*, Influence of TiO<sub>2</sub> Particle Size on Dye-Sensitized Solar Cells Employing an Organic Sensitizer and a Cobalt(III/II) Redox Electrolyte. *Journal of Physical Chemistry C* **2018**, *122*, 7051-7060.
10. Jin Kim<sup>†</sup>, Jin Soo Kang<sup>†</sup>, **Juwon Jeong**, Yoon Jun Son, Myeong Jae Lee, Jiho Kang, Ahyoung Lim, Hyun S. Park\*, Yung-Eun Sung\*, Electrochemically synthesized nanostructured iron carbide/carbon composite as a low-cost counter electrode for dye-sensitized solar cells. *Journal of Power Sources* **2018**, *396*, 213-219.
11. Jin Soo Kang<sup>†</sup>, Jin Kim<sup>†</sup>, Jeong Soo Kim, Kyungju Nam, Hyungyung Jo, Yoon Jun Son, Jiho Kang, **Juwon Jeong**, Heeman Choe\*, Tae-Hyuk Kwon\*, Yung-Eun Sung\*, Electrochemically synthesized mesoscopic nickel oxide films as photocathodes for dye-sensitized solar cells. *ACS Applied Energy Materials* **2018**, *1*, 4178-4185.
12. Jin Soo Kang<sup>†</sup>, Jiho Kang<sup>†</sup>, Jiyoung Chae<sup>†</sup>, Yoon Jun Son, **Juwon Jeong**, Jin Kim, Jae-Yup Kim, Soon Hyung Kang, Kwang-Soon Ahn\*, Yung-Eun Sung\*, Vapor-Deposited Tungsten Carbide Nano-Dendrites as Sulfur-Tolerant Electrocatalysts for Quantum Dot-Sensitized Solar Cells. *Journal of the Electrochemical Society* **2018**, *165*, H954-H961.
13. Jin Soo Kang<sup>†</sup>, Jiho Kang<sup>†</sup>, Dong Young Chung<sup>†</sup>, Yoon Jun Son, Seoni Kim, Sungjun Kim, Jin Kim, **Juwon Jeong**, Myeong Jae Lee, Heejong Shin, Subin Park, Sung Jong Yoo, Min Jae Ko, Jeyong Yoon, Yung-Eun Sung\*, Tailoring the porosity of MOF-derived N-doped carbon electrocatalysts for highly efficient solar energy conversion. *Journal of Materials Chemistry A* **2018**, *6*, 20170-20183.